

Vibrational properties of carbon nanotubes and graphite

vorgelegt von
Diplom-Physikerin
Janina Maultzsch
aus Berlin

von der Fakultät II – Mathematik und Naturwissenschaften
der Technischen Universität Berlin
zur Erlangung des akademischen Grades

Doktor der Naturwissenschaften
– Dr. rer. nat. –

genehmigte Dissertation

Promotionsausschuss:

Vorsitzender: Prof. Dr. Siegfried Hess
Berichter: Prof. Dr. Christian Thomsen
Berichter: Prof. Dr. Wolfgang Richter

Tag der wissenschaftlichen Aussprache: 15. Juni 2004

Berlin 2004
D83

Zusammenfassung

In dieser Arbeit werden die Phononen von Kohlenstoff-Nanotubes und Graphit untersucht. Kohlenstoff-Nanotubes sind quasi-eindimensionale Kristalle und bestehen aus einer oder mehreren Graphit-Ebenen, die zu einem Zylinder aufgerollt sind. Deshalb können in erster Näherung viele Eigenschaften der Nanotubes von Graphit hergeleitet werden, indem das Nanotube als ein schmales Rechteck aus Graphit mit periodischen Randbedingungen betrachtet wird.

Die hier verwendeten experimentellen Methoden sind Raman-Spektroskopie und für Graphit inelastische Röntgenstreuung. Das Ramanspektrum von Kohlenstoff-Nanotubes wurde bisher nicht im Detail verstanden, insbesondere kann es nicht in herkömmlicher Weise mit der Streuung von Γ -Punkt Phononen widerspruchsfrei erklärt werden. Abgesehen von der sogenannten Atmungsmode, einer niederenergetischen, radialen Schwingung des gesamten Tubes, sind die Ramanpeaks keine einfachen Lorentz-förmigen Moden, sondern komplexe, relativ breite Peaks. Andererseits gibt es nur zwei Phononen, die in diesem hochenergetischen Bereich des Spektrums aus Symmetrie-Gründen erlaubt sind. Eine weitere ungewöhnliche Eigenschaft ist die starke Abhängigkeit des Ramanspektrums von der Energie des anregenden Lasers. Dies betrifft nicht nur die Intensität des Spektrums, wie in gewöhnlicher resonanter Ramanstreuung, sondern auch die Frequenz der Ramanmoden und ihre Linienform. Ebenso sind bei gleicher Anregungsenergie die Spektren in Stokes- und Anti-Stokes-Streuung unterschiedlich.

Diese Eigenschaften des Ramanspektrums werden in dieser Arbeit mit Hilfe von Defekt-induzierter, doppelresonanter Ramanstreuung erklärt. Dabei führt die elastische Streuung an einem Defekt dazu, dass nicht nur Phononen vom Γ -Punkt zum Spektrum erster Ordnung beitragen können, sondern Phononen aus der gesamten Brillouin-Zone. Für diejenigen Phononen, die zu einer Doppelresonanz führen, ist die Streuwahrscheinlichkeit am stärksten und ergibt daher einen Peak im Spektrum. Wenn die Anregungsenergie geändert wird, ändert sich auch die Bedingung für die Doppelresonanz, entsprechend der elektronischen Bandstruktur und der Phononendispersion. Dadurch werden andere Phononen bevorzugt, und die Ramanpeaks verschieben sich. Im Prinzip ist es damit möglich, die Phononendispersion oder einen Teil davon durch Variation der Laserwellenlänge zu messen. Das Doppelresonanz-Modell erklärt auch alle weiteren Eigenschaften des Ramanspektrums ohne zusätzliche An-

nahmen: Selbst im Falle von nur einem Phononenzweig werden Mehrfach-Peaks vorhergesagt, die gleichzeitig durch mehrere, leicht unterschiedliche Doppelresonanz-Bedingungen hervorgerufen werden.

Neben der elektronischen Bandstruktur ist die Phononendispersion selbst bestimmend für die Doppelresonanz. Überraschenderweise gab es bisher selbst für Graphit keine vollständigen experimentellen Daten in der Literatur, unter anderem, weil nur etwa $100\ \mu\text{m}$ große Einkristalle von Graphit existieren. Entsprechend widersprüchlich sind die theoretischen Vorhersagen. Wir waren in der Lage, diese Widersprüche zu lösen, indem wir die optischen Phononen mit inelastischer Röntgenstreuung in der gesamten Brillouin-Zone gemessen haben.

Wir kombinieren nun die Kenntnisse über die Symmetrie-Eigenschaften (Auswahlregeln), die elektronische Bandstruktur und die Phononendispersionen, um die Ramanspektren mit dem Doppelresonanz-Modell explizit zu berechnen. Dabei finden wir eine sehr gute Übereinstimmung mit dem Experiment. In früheren Interpretationen der Ramanspektren wurde die starke Abhängigkeit von der Laserenergie mit der selektiven Anregung von unterschiedlichen Nanotubes erklärt, da zu dieser Zeit die meisten Experimente an Proben mit vielen verschiedenen, zu Bündeln zusammengesetzten Tubes durchgeführt wurden. In dieser Interpretation würden die Spektren eines einzelnen Nanotubes nicht von der Anregungsenergie abhängen. Hier zeigen wir jedoch durch systematische Messungen an einem einzelnen Tube, dass das Ramanspektrum dieses Tubes ebenfalls variiert. Die besonderen Eigenschaften des Ramanspektrums, vor allem die Abhängigkeit von der Laserenergie, sind also ein Effekt eines einzelnen Nanotubes, wie von der Doppelresonanz vorhergesagt.

List of publications

Carbon Nanotubes: Basic Concepts and Physical Properties

S. Reich and C. Thomsen and J. Maultzsch,

Wiley-VCH, Berlin (2004).

Phonon dispersion in graphite

J. Maultzsch, S. Reich, C. Thomsen, H. Requardt, and P. Ordejón,

Phys. Rev. Lett. **92**, 075501 (2004).

High-energy phonon branches of an individual metallic carbon nanotube

J. Maultzsch, S. Reich, U. Schlecht, and C. Thomsen,

Phys. Rev. Lett. **91**, 087402 (2003).

The radial breathing mode frequency in double-walled carbon nanotubes: an analytical approximation

E. Dobardžić, J. Maultzsch, I. Milošević, C. Thomsen, and M. Damnjanović,

phys. stat. sol., **237**, R7 (2003).

Quantum numbers and band topology of nanotubes

M. Damnjanović, I. Milošević, T. Vuković, and J. Maultzsch,

J. Phys. A: Math. Gen. **36**, 5707 (2003).

Raman characterization of boron-doped multiwalled carbon nanotubes

J. Maultzsch, S. Reich, C. Thomsen, S. Webster, R. Czerw, D. L. Carroll, S. M. C. Vieira,

P. R. Birkett, and C. A. Rego,

Appl. Phys. Lett. **81**, 2647 (2002).

Tight-binding description of graphene

S. Reich, J. Maultzsch, C. Thomsen, and P. Ordejón,

Phys. Rev. B **66**, 035412 (2002).

Raman scattering in carbon nanotubes revisited

J. Maultzsch, S. Reich, and C. Thomsen,

Phys. Rev. B **65**, 233402 (2002).

Phonon dispersion of carbon nanotubes

J. Maultzsch, S. Reich, C. Thomsen, E. Dobardžić, I. Milošević, and M. Damnjanović,

Solid State Comm. **121**, 471 (2002).

Chirality-selective Raman scattering of the *D* mode in carbon nanotubes

J. Maultzsch, S. Reich, and C. Thomsen,

Phys. Rev. B **64**, 121407(R) (2001).

Resonant Raman scattering in GaAs induced by an embedded InAs monolayer

J. Maultzsch, S. Reich, A. R. Goñi, and C. Thomsen,

Phys. Rev. B **63**, 033306 (2001).

Manuscripts under review

Chirality distribution and transition energies of carbon nanotubes

H. Telg, J. Maultzsch, S. Reich, F. Hennrich, and C. Thomsen,

submitted to *Phys. Rev. Lett.* (2004).

Double-resonant Raman scattering in graphite: interference effects, selection rules and phonon dispersion

J. Maultzsch, S. Reich, and C. Thomsen,

submitted to *Phys. Rev. B* (2004).

Resonant Raman spectroscopy of nanotubes

C. Thomsen, S. Reich, and J. Maultzsch,

submitted to *Philosophical Transactions of the Royal Society* (2004).

The strength of the radial breathing mode in single-walled carbon nanotubes

M. Machón, S. Reich, J. Maultzsch, P. Ordejón, and C. Thomsen,

submitted to *Phys. Rev. Lett.* (2003).

Conference proceedings

Vibrational properties of double-walled carbon nanotubes

J. Maultzsch, S. Reich, P. Ordejón, R. R. Bacsa, W. Bacsa, E. Dobardžić, M. Damnjanović, and C. Thomsen,

Proc. of the XVIIth Intern. Winterschool on Electronic Properties of Novel Materials, Kirchberg, Austria, ed. by H. Kuzmany, J. Fink, M. Mehring, and S. Roth, (AIP 685), 324 (2003).

Double-resonant Raman scattering in an individual carbon nanotube

C. Thomsen, J. Maultzsch, and S. Reich,

ibid., p. 225.

Raman measurements on electrochemically doped single-wall carbon nanotubes

P.M. Rafailov, M. Stoll, J. Maultzsch, and C. Thomsen,

ibid., p. 135.

Hexagonal diamond from single-walled carbon nanotubes

S. Reich, P. Ordejón, R. Wirth, J. Maultzsch, B. Wunder, H.-J. Müller, C. Lathe, F. Schilling, U. Detlaff-Weglikowska, S. Roth, and C. Thomsen,

ibid., p. 164.

Raman characterization of nitrogen-doped multiwalled carbon nanotubes

S. Webster, J. Maultzsch, C. Thomsen, J. Liu, R. Czerw, M. Terrones, F. Adar, C. John, A. Whitley, and D. L. Carroll,

Mat. Res. Soc. Symp. Proc. **772**, M7.8.1 (2003).

Double-resonant Raman scattering in single-wall carbon nanotubes

J. Maultzsch and S. Reich and C. Thomsen,

Proc. 26th ICPS, ed. by A. R. Long and J. H. Davies, (Institute of Physics Publishing, Bristol, UK), D209 (2002).

Optical properties of 4 Å-diameter single-wall nanotubes

M. Machón, S. Reich, J. Maultzsch, P. M. Rafailov, C. Thomsen, D. Sánchez-Portal, and P. Ordejón,

Proc. of the XVIth Intern. Winterschool on Electronic Properties of Novel Materials, Kirchberg, Austria, ed. by H. Kuzmany, J. Fink, M. Mehring, and S. Roth, (AIP 633), 275 (2002).

Pressure and polarization-angle dependent Raman spectra of aligned single-wall carbon nanotubes in AlPO_4 -5 crystal channels

P. M. Rafailov, J. Maultzsch, M. Machón, S. Reich, C. Thomsen, Z. K. Tang, Z. M. Li, and I. L. Li,

ibid., p. 290.

Origin of the high-energy Raman modes in single-wall carbon nanotubes

J. Maultzsch, C. Thomsen, S. Reich, and M. Machón,

ibid., p. 352.

The dependence on excitation energy of the D-mode in graphite and carbon nanotubes

C. Thomsen, S. Reich, and J. Maultzsch,

Proc. of the XVth Intern. Winterschool on Electronic Properties of Novel Materials, Kirchberg, Austria, ed. by H. Kuzmany, J. Fink, M. Mehring, and S. Roth, (AIP 591), 376 (2001).

Resonant Raman scattering in an InAs/GaAs monolayer structure

J. Maultzsch, S. Reich, A. R. Goñi, and C. Thomsen,

Proc. 25th ICPS, ed. by N. Miura and T. Ando (Springer Berlin), 697 (2001).

Contents

1	Introduction	3
2	Symmetry	7
2.1	Structure of carbon nanotubes	7
2.2	Symmetry of single-walled carbon nanotubes	13
2.2.1	Symmetry operations	14
2.2.2	Symmetry-based quantum numbers	17
2.2.3	Irreducible representations	20
2.3	Summary	24
3	Electronic band structure	25
4	Phonons in graphite and carbon nanotubes	30
4.1	Inelastic light scattering	31
4.1.1	Inelastic X-ray scattering: experiment	33
4.2	Phonon dispersion of graphite	35
4.3	Phonon dispersion of carbon nanotubes	43
4.3.1	Phonon symmetries in carbon nanotubes	44
4.3.2	Force-constants calculations	48
4.3.3	Double-walled carbon nanotubes	50
5	Double-resonant Raman scattering in carbon nanotubes	54
5.1	Introduction: Double-resonant Raman scattering	56
5.1.1	Selection rules for $q \neq 0$ in carbon nanotubes	63
5.2	The D mode in carbon nanotubes	64
5.3	The D mode in graphite	71
5.3.1	Double-resonant scattering in one dimension	71
5.3.2	Interference effects	73
5.3.3	Double-resonant scattering in two dimensions	75

5.3.4	Selection rules in graphite	76
5.3.5	Calculation of the <i>D</i> mode in graphite	78
5.4	The high-energy modes	80
5.4.1	Experiments on individual nanotubes	85
5.4.2	Metallic nanotubes	88
5.4.3	Defects	91
5.5	Absolute Raman cross section	94
5.6	Summary: Single- and double-resonance interpretation	100
6	Conclusion	103
	Bibliography	106

1 Introduction

Carbon appears in several crystalline modifications, as a result of its flexible electron configuration. The carbon atom has six electrons; the $2s$ orbital and two or three of the $2p$ orbitals can form an sp^2 or sp^3 hybrid, respectively. The sp^3 configuration gives rise to the tetrahedrally bonded structure of diamond. The sp^2 orbitals lead to strong in-plane bonds of the hexagonal structure of graphite and the remaining p -like orbital to weak bonds between the planes. Besides diamond and graphite, other modifications of crystalline carbon have been found, among them the so-called buckyballs [1] and, first reported in 1991 by Iijima [2], carbon nanotubes. Soon after their discovery in multiwall form, carbon nanotubes consisting of one single layer were found [3,4]. The most famous one of the buckyballs is probably C_{60} , a spherical molecule formed by pentagons and hexagons, out of which single C_{60} crystals have been produced [5].

Carbon nanotubes are quasi-one dimensional crystals with the shape of hollow cylinders made of one or more graphite sheets; they are typically μm in length and 1 nm in diameter. Along the cylinder axis, they can therefore be regarded as infinitely long (approximately 10^4 atoms along $1\ \mu\text{m}$), whereas along the circumference there are only very few atoms (≈ 20). This gives rise to discrete wave vectors in the circumferential direction and quasi-continuous wave vectors along the tube axis. Although carbon nanotubes consist of merely carbon atoms, their physical properties can vary significantly, depending sensitively on the microscopic structure of the tube. Most prominent is their metallic or semiconducting character: roughly speaking $2/3$ of the possible nanotube structures are semiconducting and $1/3$ are metallic. Carbon nanotubes exhibit remarkable physical properties. They were reported to carry electric currents up to 10^9 A/cm^2 [6, 7]. Furthermore, nanotube ropes are of extraordinary mechanical strength with an elastic modulus on the order of 1 TPa , and a shear modulus of approximately 1 GPa [8, 9]. Therefore, they are extremely stiff along their axis but easy to bend perpendicular to the axis. The shear modulus in the ropes can be enlarged by introducing bonds between the tubes by electron beam irradiation [10].

The many possible applications of carbon nanotubes both on the nanometer scale and in the macroscopic range attract great attention. Some of them have been realized on an industry scale already, whereas others still require sophisticated preparation. The latter include single-

nanotube electronic devices such as field-effect transistors [11] or even logic circuits [12]. In so-called actuators, an electrolytically doped nanotube paper is bent by an applied bias [13, 14]. Furthermore, carbon nanotubes were suggested to be used as torsional springs [15, 16] or as single vibrating strings for ultrasmall force sensing. A major difficulty for these applications is the variety of nanotube structures that are produced simultaneously; in particular, a growth method which determines whether the tubes will be metallic or semiconducting is still not available. Instead, the production methods yield tube ensembles where presumably all nanotube structures are equally distributed, and the tubes are typically found in bundles. Other applications like nanotube field emitters or reinforcing materials by adding carbon nanotubes, do not require specific isolated tubes and are thus easier to realize.

Beyond the variety of applications, carbon nanotubes are interesting from a fundamental-physics point of view. Their one-dimensional character has been manifested in many experiments like scanning-tunneling spectroscopy, where the singularities in the density of states typical for one dimension have been measured [17–19]. They appear an ideal system for the study of Luttinger liquid behavior [20, 21]. Ballistic transport at room temperature up to several μm was reported [22]. Alternatively, defects or electrical contacts can act as boundaries, and zero-dimensional effects such as Coulomb blockade are observed [23, 24]. In contrast to many quasi-one-dimensional systems in semiconductor physics, where carriers are artificially restricted to a one-dimensional phase space by sophisticated fabrication like cleaved-edge overgrowth [25, 26] or experiments in the quantum-Hall regime [27], carbon nanotubes are natural quasi-one-dimensional systems with ideal periodic boundary conditions along the circumference. Furthermore, they have a highly symmetric microscopic structure which can be regarded a realization of the so-called line groups that were introduced to describe the symmetry properties of mono-periodic crystals [28–30].

Since carbon nanotubes were first reported in 1991, research in this field has made tremendous progress during the last years regarding both applications and fundamental properties [31]. This includes improved control over growth conditions (for a review see [32, 33]), the ability to deposit nanotubes onto specific sites of a substrate, to debundle the tubes and measure them individually [34], and, very recently, to prevent tubes from rebundling by enclosing them into a surfactant [35]. The latter allowed key experiments in the optical characterization, the observation of photoluminescence from the band gap of semiconducting tubes [36–39], and investigations of the carrier dynamics by time-resolved optical spectroscopy [40, 41]. Furthermore, given a stable solution of isolated nanotubes, metallic tubes could be separated from semiconducting ones by electrophoresis [42].

The third fundamental characteristics of a crystal, besides the transport and optical properties mentioned above, are the vibrational and elastic properties. For example, the long-

wavelength acoustic phonons give the elastic moduli. Moreover, the phonon spectrum determines the thermal properties and influences the non-radiative relaxation of excited carriers and electronic transport. Raman scattering is a powerful tool to study the vibrational properties of a crystal and provides deep insight into the fundamental physical processes that take place. The Raman process includes absorption and emission of light as well as inelastic scattering of electrons by phonons (or other quasi-particles like magnons and plasmons). Thus information on both electronic and vibrational properties and on electron-phonon interaction is obtained. If the details of the Raman process are well understood, the experiments can also be used for characterizing the sample.

Although one would expect a large number of phonon modes in the Raman spectrum of carbon nanotubes due to the confinement, there are in fact only three major bands in the first-order spectrum. This is a consequence of the high symmetry of the nanotube, leading to selection rules that prohibit most of the phonon modes in the Raman process. Because of the small mass of the carbon atoms combined with strong carbon-carbon bonds, the phonon frequencies are much larger than what is typically observed in semiconductors like GaAs or Si. The strongest Raman modes are the radial breathing mode (a breathing-like vibration of the entire tube) around 200 cm^{-1} , and in the high-energy range the disorder-induced *D* mode (1350 cm^{-1}) and the high-energy modes (1600 cm^{-1}). The Raman spectrum of carbon nanotubes has a number of peculiar properties. The first-order modes – except for the radial breathing mode – are not composed by single Lorentzian peaks but have a rather complex line shape. In particular, the high-energy mode consists of a multiple-peak structure that cannot simply be explained by the two allowed first-order Raman modes. It changes dramatically with laser energy, which was previously attributed to the selective excitation of metallic and semiconducting nanotubes. Even more surprising is the shift of the high-energy mode frequencies with excitation energy.

In spite of a large number of Raman studies in carbon nanotubes, the origin of the spectra was not fully understood. In particular, it was not clear whether the characteristics of the nanotube spectra, like the excitation-energy dependence, were results of averaging the properties of many tubes measured simultaneously in tube ensembles or whether these effects would be observed in single nanotubes as well. The proposal of defect-induced, double-resonant Raman scattering as the origin of the entire first-order spectrum in carbon nanotubes at the beginning of this thesis has led to controversial discussions [43–45]. This concept attributes the strong laser-energy dependence of the Raman modes to single-tube effects rather than to a selective excitation of different tubes. Besides the electronic band structure, the most important ingredient to the double-resonant Raman process is the phonon dispersion. Surprisingly, it had not even in graphite been determined experimentally, and theories were contradictory. Here we

want to solve these questions and develop a consistent description of the Raman scattering mechanism in carbon nanotubes.

To understand the Raman processes in carbon nanotubes, a profound knowledge of their symmetry properties is needed. First, the selection rules for electron-photon and electron-phonon interactions can be derived, which give rise to a systematic understanding of allowed and forbidden processes, independent of a specific model or approximation. Second, the symmetry-based treatment provides a simple and elegant way to describe quasi-particle states in the nanotube and their interaction. We devote Chap. 2 to the symmetry properties of carbon nanotubes [46], after a brief explanation of their geometrical structure and the construction of the Brillouin zone. We discuss the line-group formalism and two different sets of quantum numbers developed by Damnjanović *et al.* [47], which both are used in this work depending on the particular problem. Since resonant Raman scattering depends on the details of the electronic band structure, we will briefly review the electronic properties of carbon nanotubes in Chap. 3 as far as we will need them in the discussion of the scattering processes. We investigate in Chap. 4 the phonons themselves, going back to graphite as the reference material to carbon nanotubes. We measured for the first time the entire optical phonon dispersion in all high-symmetry directions in the graphite plane. These measurements had become possible by the recently developed experimental technique of inelastic X-ray scattering. Our experimental results solve long-standing discrepancies between different theoretical models. We performed force-constants calculations of the nanotube phonon dispersion. Furthermore, we briefly discuss *ab-initio* calculations of the phonon frequencies in double-walled carbon nanotubes. Finally, we can combine the understanding obtained on symmetry, electronic and vibrational properties of carbon nanotubes to work out the details of the Raman scattering processes in Chap. 5. In particular, we will address the question of single and double-resonant scattering and, closely related, the distinction between single-tube and tube-ensemble effects. The double-resonance picture of the disorder-induced *D* mode is further developed, using the experimental results of the graphite phonon dispersion to calculate the Raman spectra. For the high-energy modes, the key experiments to distinguish between double and single-resonant scattering are Raman measurements on the same individual tube at varying laser wavelengths. The results give clear evidence for the double-resonant nature of the Raman modes, and we show that by changing the excitation energy part of the phonon dispersion of a metallic tube can be mapped. Finally, the absolute Raman cross section of the radial breathing mode is measured and compared with *ab-initio* calculations.

2 Symmetry

Carbon nanotubes are hollow cylinders of graphite sheets. They can be viewed as single molecules, regarding their small size (\sim nm in diameter and \sim μ m length), or as quasi-one dimensional crystals with translational periodicity along the tube axis. There are infinitely many ways to roll a sheet into a cylinder, resulting in different diameters and microscopic structures of the tubes. These are defined by the chiral index that gives the angle of the hexagon helix around the tube axis. Some properties of carbon nanotubes like their elasticity [48] can be explained within a macroscopic model of an homogeneous cylinder, whereas others depend crucially on the microscopic structure of the tubes. The latter include, for instance, the electronic band structure, in particular, their metallic or semiconducting nature (Chap. 3). The fairly complex microscopic structure with tens to hundreds of atoms in the crystal unit cell can be described in a very general way with the help of the nanotube symmetry. This greatly simplifies understanding and calculating physical properties like optical absorption, phonon eigenvectors, and electron–phonon coupling.

In this chapter we first describe the geometric structure of carbon nanotubes and the construction of their Brillouin zone in relation to that of graphite (Sect. 2.1). The symmetry properties of single-walled tubes are presented in Sect. 2.2. We explain how to obtain the entire tube of a given chirality from one single carbon atom by applying the symmetry operations. Furthermore, we give an introduction to the theory of line groups of carbon nanotubes [46], and explain the quantum numbers, irreducible representations, and their notation.

2.1 Structure of carbon nanotubes

A tube made of a single graphite layer rolled up into a hollow cylinder is called a single-walled nanotube (SWNT); a tube comprising several, concentrically arranged cylinders is referred to as a multiwall tube (MWNT). Single-walled nanotubes, as typically investigated in the work presented here, are produced by laser ablation, high-pressure CO conversion (HiPCO), or the arc-discharge technique, and have a Gaussian distribution of diameters d with mean diameters $d_0 \approx 1.0 - 1.5$ nm [32, 33, 49, 50]. The chiral angles [Eq. (2.1)] are evenly distributed [51].

Single-walled tubes form hexagonal-packed bundles during the growth process. The wall-to-wall distance between two tubes is in the same range as the interlayer distance in graphite ($\approx 3.41 \text{ \AA}$). Multiwall nanotubes have similar lengths to single-walled tubes, but much larger diameters. Their inner and outer diameters are around 5 and 100 nm, respectively, corresponding to ≈ 30 coaxial tubes. Confinement effects are expected to be less dominant than in single-walled tubes, because of the larger circumference. Many properties of multiwall tubes are similar to those of graphite.

Because the microscopic structure of carbon nanotubes is derived from that of graphene¹, the tubes are usually labeled in terms of the graphene lattice vectors. Figure 2.1 shows the graphene honeycomb lattice. The unit cell is spanned by the two vectors \mathbf{a}_1 and \mathbf{a}_2 and contains two carbon atoms at the positions $\frac{1}{3}(\mathbf{a}_1 + \mathbf{a}_2)$ and $\frac{2}{3}(\mathbf{a}_1 + \mathbf{a}_2)$, where the basis vectors of length $|\mathbf{a}_1| = |\mathbf{a}_2| = a_0 = 2.461 \text{ \AA}$ form an angle of 60° . In carbon nanotubes, the graphene sheet is rolled up in such a way that a graphene lattice vector $\mathbf{c} = n_1\mathbf{a}_1 + n_2\mathbf{a}_2$ becomes the circumference of the tube. This circumferential vector \mathbf{c} , which is usually denoted by the pair of integers (n_1, n_2) , is called the chiral vector and uniquely defines a particular tube. We will see below that the electronic band structure or the spatial symmetry group of nanotubes vary dramatically with the chiral vector, even for tubes with similar diameter and direction of the chiral vector. For example, the (10,10) tube contains 40 atoms in the unit cell and is metallic; the close-by (10,9) tube with 1084 atoms in the unit cell is a semiconducting tube.

In Fig. 2.1, the chiral vector $\mathbf{c} = 8\mathbf{a}_1 + 4\mathbf{a}_2$ of an (8,4) tube is shown. The circles indicate the four points on the chiral vector that are lattice vectors of graphene; the first and the last circle coincide if the sheet is rolled up. The number of lattice points on the chiral vector is given by the greatest common divisor n of (n_1, n_2) , since $\mathbf{c} = n(n_1/n \cdot \mathbf{a}_1 + n_2/n \cdot \mathbf{a}_2) = n \cdot \mathbf{c}'$ is a multiple of another graphene lattice vector \mathbf{c}' .

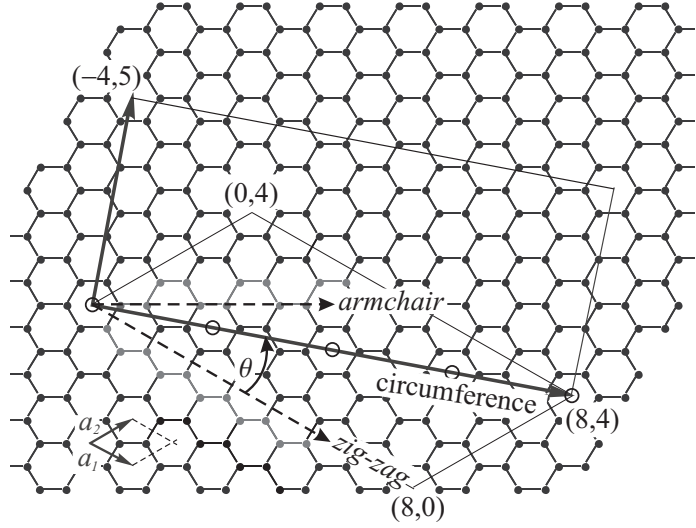
The direction of the chiral vector is measured by the chiral angle θ , which is defined as the angle between \mathbf{a}_1 and \mathbf{c} . The chiral angle θ can be calculated from

$$\cos \theta = \frac{\mathbf{a}_1 \cdot \mathbf{c}}{|\mathbf{a}_1| \cdot |\mathbf{c}|} = \frac{n_1 + n_2/2}{\sqrt{n_1^2 + n_1 n_2 + n_2^2}} \quad . \quad (2.1)$$

For each tube with θ between 0° and 30° an equivalent tube with θ between 30° and 60° exists, but the helix of graphene lattice points around the tube changes from right-handed to left-handed. Because of the six-fold rotational symmetry of graphene, to any other chiral vector an equivalent one exists with $\theta \geq 60^\circ$. We will hence restrict ourselves to the case $n_1 \geq n_2 \geq 0$ (or $0^\circ \leq \theta \leq 30^\circ$). Tubes of the type $(n, 0)$ ($\theta = 0^\circ$) are called zig-zag tubes, because they exhibit a zig-zag pattern along the circumference, see Fig. 2.1. (n, n) tubes are called armchair

¹Graphene is a single, two-dimensional layer of graphite.

Figure 2.1: Graphene honeycomb lattice with the lattice vectors \mathbf{a}_1 and \mathbf{a}_2 . The chiral vector $\mathbf{c} = 8\mathbf{a}_1 + 4\mathbf{a}_2$ of the (8,4) tube is shown with the 4 graphene-lattice points indicated by circles; the first and the last coincide if the sheet is rolled up. Perpendicular to \mathbf{c} is the tube axis z , the minimum translational period is given by the vector $\mathbf{a} = -4\mathbf{a}_1 + 5\mathbf{a}_2$. The vectors \mathbf{c} and \mathbf{a} form a rectangle, which is the unit cell of the tube, if it is rolled along \mathbf{c} into a cylinder. The zig-zag and armchair patterns along the chiral vector of zig-zag and armchair tubes, respectively, are highlighted.



tubes; their chiral angle is $\theta = 30^\circ$. Both, zig-zag and armchair tubes are achiral tubes, in contrast to the general chiral tubes.

The geometry of the graphene lattice and the chiral vector of the tube determine its structural parameters like diameter, unit cell, and its number of carbon atoms, as well as size and shape of the Brillouin zone. The diameter of the tube is simply given by the length of the chiral vector:

$$d = \frac{|\mathbf{c}|}{\pi} = \frac{a_0}{\pi} \sqrt{n_1^2 + n_1 n_2 + n_2^2} = \frac{a_0}{\pi} \sqrt{N}, \quad (2.2)$$

with $N = n_1^2 + n_1 n_2 + n_2^2$. The smallest graphene lattice vector \mathbf{a} perpendicular to \mathbf{c} defines the translational period a along the tube axis. For example, for the (8,4) tube in Fig. 2.1 the smallest lattice vector along the tube axis is $\mathbf{a} = -4\mathbf{a}_1 + 5\mathbf{a}_2$. In general, the translational period a is determined from the chiral indices (n_1, n_2) by

$$\mathbf{a} = -\frac{2n_2 + n_1}{n\mathcal{R}} \mathbf{a}_1 + \frac{2n_1 + n_2}{n\mathcal{R}} \mathbf{a}_2, \quad (2.3)$$

and

$$a = |\mathbf{a}| = \frac{\sqrt{3(n_1^2 + n_1 n_2 + n_2^2)}}{n\mathcal{R}} a_0, \quad (2.4)$$

where $\mathcal{R} = 3$ if $(n_1 - n_2)/3n$ is integer and $\mathcal{R} = 1$ otherwise. Thus, the nanotube unit cell is formed by a cylindrical surface with height a and diameter d . For achiral tubes, Eqs. (2.2) and (2.4) can be simplified to

$$\begin{aligned} a_z &= \sqrt{3} \cdot a_0 & |\mathbf{c}_z| &= n a_0 & (\text{zig-zag}) \\ a_A &= a_0 & |\mathbf{c}_A| &= \sqrt{3} \cdot n a_0 & (\text{armchair}). \end{aligned} \quad (2.5)$$

Figure 2.2: Structure of the (17,0), the (10,10) and the (12,8) tube. The unit cells of the tubes are highlighted; the translational period a is indicated.

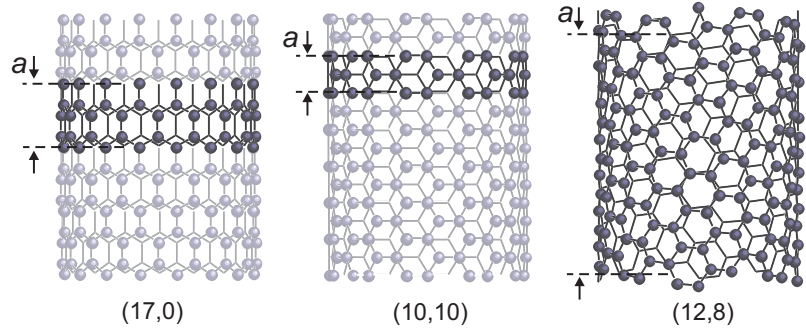
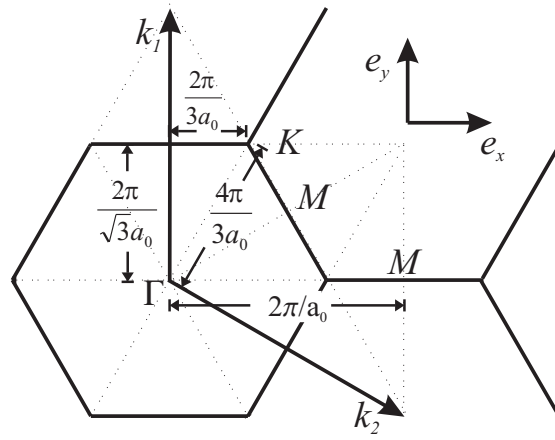


Figure 2.3: Brillouin zone of graphene with the high-symmetry points Γ , K , and M . The reciprocal lattice vectors \mathbf{k}_1 , \mathbf{k}_2 in Cartesian coordinates are $\mathbf{k}_1 = (0, 1)4\pi/\sqrt{3}a_0$ and $\mathbf{k}_2 = (0.5\sqrt{3}, -0.5)4\pi/\sqrt{3}a_0$.



For chiral tubes, \mathbf{a} and \mathbf{c} have to be calculated from Eqs. (2.2) and (2.4). Tubes with the same chiral angle θ , *i.e.*, with the same ratio n_1/n_2 , possess the same lattice vector \mathbf{a} . In Fig. 2.2 the structures of (17,0), (10,10), and (12,8) tubes are shown, where the unit cell is highlighted and the translational period a is indicated. Note that a varies strongly with the chirality of the tube; chiral tubes often have very long unit cells.

The number of carbon atoms in the unit cell, n_c , can be calculated from the area $S_t = a \cdot c$ of the cylinder surface and the area S_g of the hexagonal graphene unit cell. The ratio of these two gives the number q of graphene hexagons in the nanotube unit cell

$$q = S_t/S_g = \frac{2(n_1^2 + n_1 n_2 + n_2^2)}{n\mathcal{R}}. \quad (2.6)$$

Since the graphene unit cell contains two carbon atoms, there are

$$n_c = 2q = \frac{4(n_1^2 + n_1 n_2 + n_2^2)}{n\mathcal{R}} \quad (2.7)$$

carbon atoms in the unit cell of the nanotube. In achiral tubes, $q = 2n$. The structural parameters given above are summarized in Table 2.1.

After having determined the unit cell of carbon nanotubes, we now construct their Brillouin zone. For comparison, we show in Fig. 2.3 the hexagonal Brillouin zone of graphene with the

Table 2.1: Structural parameters of armchair (\mathcal{A}), zig-zag (\mathcal{Z}) and chiral (\mathcal{C}) nanotubes. The symbols are explained in the text.

	Tube	N	$q = n_c/2$
\mathcal{A}	(n, n)	$3n^2$	$2n$
\mathcal{Z}	$(n, 0)$	n^2	$2n$
\mathcal{C}	(n_1, n_2)	$n_1^2 + n_1 n_2 + n_2^2$	$2N/(n\mathcal{R})$
	Diameter d	Translational period a	Chiral angle θ
\mathcal{A}	$\sqrt{3} n a_0 / \pi$	a_0	30°
\mathcal{Z}	$n a_0 / \pi$	$\sqrt{3} a_0$	0°
\mathcal{C}	$\sqrt{N} a_0 / \pi$	$\sqrt{3N} a_0 / (n\mathcal{R})$	$\arccos(n_1 + n_2/2) / \sqrt{N}$

high-symmetry points Γ , K , and M and the distances between these points. In the direction of the tube axis, which we define as the z -axis, the reciprocal lattice vector k_z corresponds to the translational period a ; its length is

$$k_z = 2\pi/a. \quad (2.8)$$

As the tube is regarded as infinitely long, the wave vector k_z is continuous; the first Brillouin zone in the z -direction is the interval $(-\pi/a, \pi/a]$. The bracket types $()$ and $[]$ indicate open and closed intervals, respectively. Along the circumference \mathbf{c} of the tube, any wave vector k_\perp is quantized according to the boundary condition

$$m \cdot \lambda = |\mathbf{c}| = \pi \cdot d \quad \Leftrightarrow \quad k_{\perp, m} = \frac{2\pi}{\lambda} = \frac{2\pi}{|\mathbf{c}|} \cdot m = \frac{2}{d} \cdot m, \quad (2.9)$$

where m is an integer taking the values $-q/2 + 1, \dots, 0, 1, \dots, q/2$. A wave with wave vector $k_{\perp, m} = \frac{2}{d} \cdot m$ has $2m$ nodes around the circumference. The maximum $|k_{\perp, m}|$ (minimum wavelength) follows from the number of atoms ($2q$) in the unit cell: a projection of the carbon atoms on the circumference of the tube leads to equidistant pairs of carbon atoms; then at least 4 atoms are necessary for defining a wavelength, *i.e.*, $|m| \leq q/2$. The first Brillouin zone then consists of q lines parallel to the z -axis separated by $k_\perp = 2/d$ and $k \in (-\pi/a, \pi/a]$.

The quantized wave vector \mathbf{k}_\perp and the reciprocal lattice vector \mathbf{k}_z are found from the conditions

$$\begin{aligned} \mathbf{k}_\perp \cdot \mathbf{c} &= 2\pi & \mathbf{k}_\perp \cdot \mathbf{a} &= 0 \\ \mathbf{k}_z \cdot \mathbf{c} &= 0 & \mathbf{k}_z \cdot \mathbf{a} &= 2\pi. \end{aligned} \quad (2.10)$$

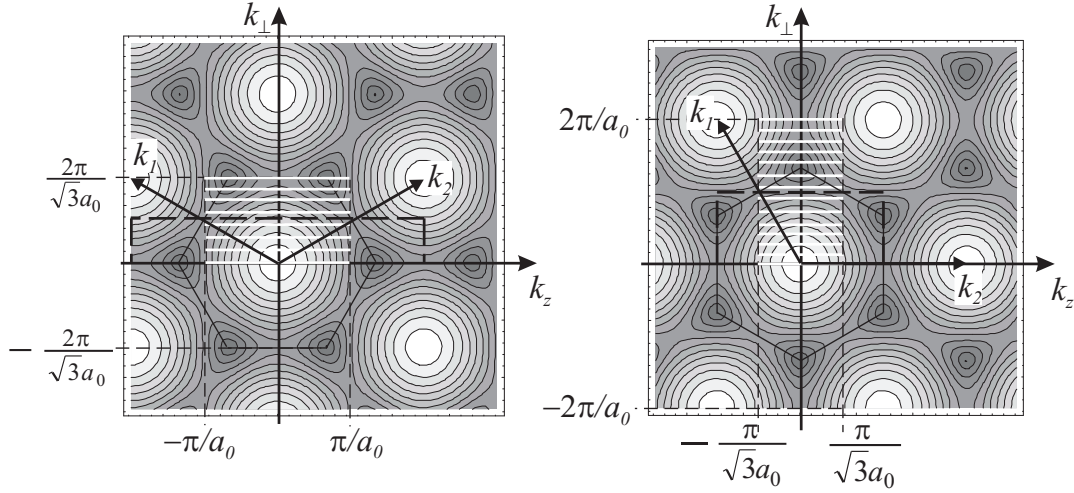


Figure 2.4: Brillouin zone of a (7,7) armchair and a (13,0) zig-zag tube (thick lines). The background is a contour plot of the electronic band structure of graphene (white indicates the maximum energy). The graphene Brillouin zone in the right panel is rotated by 30° . The Brillouin zone consists of $2n$ (i.e., 14 and 26, respectively) lines parallel to k_z , where k_z is the reciprocal lattice vector along the tube axis. Each line is indexed by $m \in [-n, n]$, where $m = 0$ corresponds to the line through the graphene Γ point ($k = 0$). Note that the Brillouin-zone boundary π/a is given by π/a_0 for armchair and $\pi/\sqrt{3}a_0$ for zig-zag tubes. It can be seen from the symmetry of the graphite hexagonal Brillouin zone that lines with index m and $-m$ are equivalent. The same holds for k and $-k$ with the same index m .

This yields

$$\mathbf{k}_\perp = \frac{2n_1 + n_2}{qn\mathcal{R}} \mathbf{k}_1 + \frac{2n_2 + n_1}{qn\mathcal{R}} \mathbf{k}_2 \quad (2.11)$$

$$\mathbf{k}_z = -\frac{n_2}{q} \mathbf{k}_1 + \frac{n_1}{q} \mathbf{k}_2. \quad (2.12)$$

In Fig. 2.4 the Brillouin zones of a (7,7) armchair and a (13,0) zig-zag tube are shown for $m \in [-n, n]$ in relation to the graphene Brillouin zone. The line through the graphene Γ point has the index $m = 0$. The position of the lines with $m = 0$ and $m = n$ is the same for all zig-zag and all armchair tubes, respectively, independent of their diameter. With increasing diameter the number of lines increases while their distance decreases. For chiral tubes, see Fig. 2.8.

To a first approximation, the properties of carbon nanotubes are related to those of graphite by taking from graphene the lines that correspond to the nanotube Brillouin zone, according to Eqs. (2.11) and (2.12). For example, the electronic band structure of a particular nanotube is found by cutting the two-dimensional band structure of graphene (see background of Fig. 2.4) into q lines of length $2\pi/a$ and distance $2/d$ parallel to the direction of the tube axis. This approach is called *zone folding* and is commonly used in nanotube research. Since the zone-

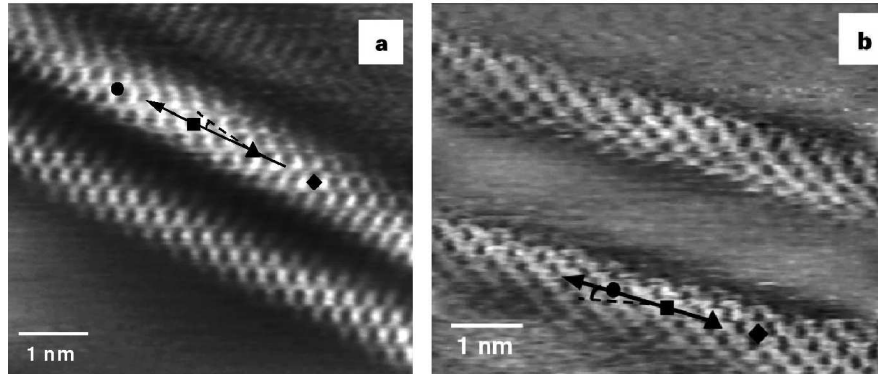


Figure 2.5: Scanning tunneling microscopy images of an isolated semiconducting (a) and metallic (b) single-walled carbon nanotube on a gold substrate. The solid arrows are in the direction of the tube axis; the dashed line indicates the zig-zag direction. Based on the diameter and chiral angle determined from the STM image, the tube in (a) was assigned to a $(14, -3)$ tube and in (b) to a $(12, 3)$ tube. The semiconducting and metallic behavior of the tubes, respectively, was confirmed by tunneling spectroscopy at specific sites. From Ref. [17].

folding procedure, however, neglects any effects of the cylinder geometry and curvature of the tube walls, results obtained by zone folding have to be used with great care.

Experimentally, the atomic structure of carbon nanotubes can be investigated either by direct imaging techniques, such as transmission electron microscopy [2, 52] and scanning probe microscopy [17, 19, 53–58], or by electron diffraction [59–62], *i.e.*, imaging in reciprocal space. Scanning tunneling microscopy (STM) offers measurements with atomic resolution, see Fig. 2.5. From both, STM and electron diffraction, the chiral angle and tube diameter can be determined, and hence the chiral vector (n_1, n_2) , in principle, can be found experimentally. Interpretation of the images is, however, delicate and often requires computations of the images and cross-checking with other experimental results.

2.2 Symmetry of single-walled carbon nanotubes

The symmetry of carbon nanotubes is described by the so-called line groups, which were introduced by Damnjanović *et al.* [28–30, 63, 64]. Line groups are the full space groups of one-dimensional systems including translations in addition to the point-group symmetries like rotations or reflections. Therefore, they provide a complete set of quantum numbers. Damnjanović *et al.* [46, 47, 65] showed that every nanotube with a particular chirality (n_1, n_2) belongs to a different line group. Only armchair and zig-zag tubes with the same n belong to the same symmetry group. Moreover, starting from a single carbon atom, the successive application of all symmetry operations of the group constructs the whole tube. Because the relation between the carbon atoms and the symmetry operations is one-to-one, the nanotubes can be viewed as

a realization of the line groups. Here we present the basic concepts of line groups and their application in carbon nanotube physics.

2.2.1 Symmetry operations

In order to find the symmetry groups of carbon nanotubes, the symmetry operations of graphene are considered [46, 65]. Those that are preserved when the graphene sheet is rolled into a cylinder form the nanotube symmetry group. Translations by multiples of a of the graphene sheet parallel to \mathbf{a} remain translations of the nanotube parallel to the tube axis, see Fig. 2.2. They form a subgroup \mathbf{T} containing the pure translations of the tube. Translations parallel to the circumferential vector \mathbf{c} (perpendicular to \mathbf{a}) become pure rotations of the nanotube about its axis. Given n graphene lattice points on the chiral vector \mathbf{c} , the nanotube can be rotated by multiples of $2\pi/n$. Single-walled nanotubes thus have n pure rotations in their symmetry group, which are denoted by C_n^s ($s = 0, 1, \dots, n-1$). These again form a subgroup \mathbf{C}_n of the full symmetry group.

Translations of the graphene sheet along any other direction are combinations of translations in the \mathbf{a} and the \mathbf{c} direction. Therefore, when the graphene sheet is rolled up, they result in translations combined with rotations about the nanotube axis. The order of these screw axis operations is equal to the number q of graphene lattice points in the nanotube unit cell. They are denoted by $(C_q^w | an/q)^t$ with the parameter

$$w = \frac{q}{n} \text{Fr} \left[\frac{n}{q\mathcal{R}} \left(3 - 2 \frac{n_1 - n_2}{n_1} \right) + \frac{n}{n_1} \left(\frac{n_1 - n_2}{n} \right)^{\varphi(n_1/n) - 1} \right]. \quad (2.13)$$

$\text{Fr}[x]$ is the fractional part of the rational number x , and $\varphi(n)$ is the Euler function [66]. On the unwrapped sheet the screw-axis operation corresponds to the primitive graphene translation $\frac{w}{q}\mathbf{c} + \frac{n}{q}\mathbf{a}$. The nanotube line group always contains a screw axis; this can be seen from Eq. (2.6), which yields $q/n \geq 2$. In achiral tubes, $q/n = 2$ and $w = 1$, thus the screw axis operations in these tubes consist of a rotation by π/n followed by a translation by $a/2$, see Fig. 2.2.

From the six-fold rotation of the hexagon about its midpoint only the two-fold rotation remains a symmetry operation in carbon nanotubes. Rotations by any other angle do not preserve the tube axis and are therefore not symmetry operations of the nanotube. This rotational axis, which is present in both chiral and achiral tubes, is perpendicular to the tube axis and denoted by U . In Fig. 2.6 the U -axis is shown in the (8,6), the (6,0), and the (6,6) nanotube. The U -axis points through the midpoint of a hexagon perpendicular to the cylinder surface. Equivalent to the U -axis is the two-fold axis U' through the midpoint between two carbon atoms.

Mirror planes perpendicular to the graphene sheet must either contain the tube axis (vertical mirror plane σ_x) or must be perpendicular to it (horizontal mirror plane σ_h) in order to transform

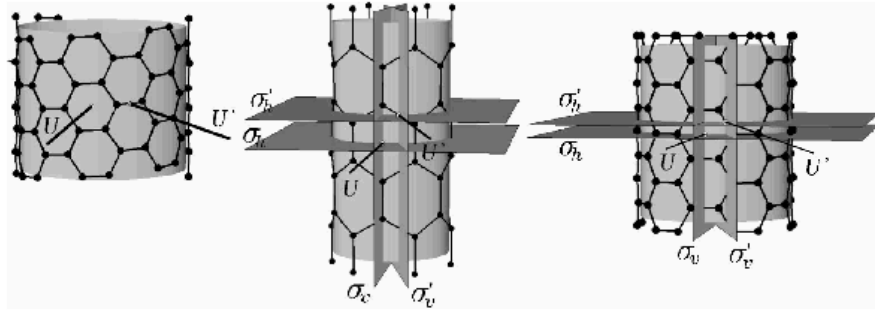


Figure 2.6: Mirror and glide planes and the two-fold rotational axes. *Left:* (8,6) nanotube with the U and U' axes. As a chiral tube, it does not have mirror symmetries. *Middle:* (6,0) tube (zig-zag). *Right:* (6,6) tube (armchair). The achiral tubes possess the horizontal rotational axes (U and U'), the horizontal (σ_h) and the vertical (σ_v) mirror planes (σ_x is in the Figure indicated as σ_v), the glide plane σ_x' (σ_v'), and the roto-reflection plane σ_h' . Taken from Ref. [46].

the nanotube into itself. Only in achiral tubes the vertical and horizontal mirror planes, σ_x and σ_h , are present [46], see Fig. 2.6. They contain the midpoints of the graphene hexagons. Additionally, in achiral tubes the vertical and horizontal planes through the midpoints between two carbon atoms form vertical glide planes (σ_x') and horizontal roto-reflection planes (σ_h') (Fig. 2.6).

In summary, the general element of any carbon-nanotube line group is denoted as

$$l(t, u, s, v) = (C_q^w | \frac{an}{q})^t C_n^s U^u \sigma_x^v, \quad (2.14)$$

$$\begin{aligned} \text{with } t &= 0, \pm 1, \dots; \\ s &= 0, 1, \dots, n-1; \\ u &= 0, 1; \\ v &= \begin{cases} 0, 1 & \text{achiral} \\ 0 & \text{chiral} \end{cases} \end{aligned}$$

and w, n, q as given above. Note that $\sigma_h = U \sigma_x$. The elements in Eq. (2.14) form the line groups \mathbf{L} , which are given by the product of the point groups \mathbf{D}_n and \mathbf{D}_{nh} for chiral and achiral tubes, respectively, and the axial group \mathbf{T}_q^w :

$$\mathbf{L}_{AZ} = \mathbf{T}_{2n}^1 \mathbf{D}_{nh} = \mathbf{L}2n_n/mcm \quad (\text{armchair and zig-zag}) \quad (2.15)$$

and

$$\mathbf{L}_C = \mathbf{T}_q^w \mathbf{D}_n = \mathbf{L}q_p22 \quad (\text{chiral tubes}). \quad (2.16)$$

Here $2\pi w/q$ determines the screw axis of the axial group. The international notation is included for a reference to the Tables of Kronecker Products in Refs. [63] and [64].²

For many applications of symmetry it is not necessary to work with the full line group. Instead, the point group is sufficient. For example, electronic and vibrational eigenfunctions at the Γ point always transform as irreducible representations of the isogonal point group. For optical transitions or first-order Raman scattering the point group is sufficient, because these processes do not change the wave vector k . The point groups isogonal to the nanotube-line groups, *i.e.*, with the same order of the principal rotational axis, where the rotations include the screw-axis operations, are

$$\begin{aligned} & \mathbf{D}_q \quad \text{for chiral} \\ \text{and } & \mathbf{D}_{2nh} \quad \text{for achiral tubes.} \end{aligned} \tag{2.17}$$

Since carbon-nanotube line groups always contain the screw axis, they are non-symmorphic groups, and the isogonal point group is not a subgroup of the full symmetry group. We will consider this below in more detail when we introduce the quantum numbers.

After having determined the symmetry operations that leave the whole tube invariant, we now investigate whether they leave a single atom invariant or not. Those that do form the site symmetry of the atom and are called stabilizers; the others form the transversal of the group [47]. In principle, a calculation for all carbon atoms in the unit cell can be restricted to those atoms that by application of the transversal form the entire system. As an example we show how the atomic positions of the tube can be obtained from a single carbon atom [46]. We start with an arbitrary carbon atom and apply the U -axis operation. The atom is mapped onto the second atom of the graphene unit cell (hexagon). The n -fold rotation about the tube axis then generates all other hexagons with the first atom on the circumference. The screw-axis operations (without pure translations) map these atoms onto the remaining atoms of the unit cell. Finally, translating all the atoms of the unit cell by the translational period a forms the whole tube. Thus if we know for example the electronic wave function of the tube at the starting atom, we know the wave function of the entire tube.

Just a single atom is needed to construct the whole tube by application of the symmetry operations of the tube; such a system is called a single-orbit system. The line groups of chiral tubes comprise, besides the identity element, no further symmetry operations but those that have been used for the construction of the tube. Therefore, the stabilizer of a carbon atom in chiral tubes is the identity element; its site symmetry is \mathbf{C}_1 . In achiral tubes, on the other hand, there are additional mirror planes σ_h and σ_x . Reflections in the σ_h plane in armchair tubes and in the σ_x plane in zig-zag tubes leave the carbon atom invariant. Thus the site symmetry of

²In these references, the meanings of the symbols n and q in are interchanged.

Table 2.2: Symmetry properties of armchair (\mathcal{A}), and zig-zag (\mathcal{Z}) and chiral (\mathcal{C}) nanotubes. The symbols are explained in the text. From the position \mathbf{r}_{000} of the first carbon atom the whole tube can be constructed by application of the line-group symmetry operations, see Eq. (2.19).

Tube	Line group	Isogonal point group		\mathbf{r}_{000}	
\mathcal{A}	(n, n)	$T_{2n}D_{nh}$	D_{2nh}	$L2n_n/mcm$	$(r_0, \frac{2\pi}{3n}, 0)$
\mathcal{Z}	$(n, 0)$	$T_{2n}D_{nh}$	D_{2nh}	$L2n_n/mcm$	$(r_0, \frac{\pi}{n}, \frac{a_0}{2\sqrt{3}})$
\mathcal{C}	(n_1, n_2)	$T_q^r D_n$	D_q	$Lq_p 22$	$(r_0, 2\pi \frac{n_1+n_2}{2N}, \frac{n_1-n_2}{2\sqrt{3N}} a_0)$

the carbon atoms in achiral tubes is \mathbf{C}_{1h} . We will see later that the higher site symmetry of achiral nanotubes imposes strict conditions on their phonon eigenvectors and electronic wave functions.

Using the symmetry operations of the tube, the atomic positions \mathbf{r} in the unit cell can be easily found. The position of the first carbon atom is defined at $\frac{1}{3}(\mathbf{a}_1 + \mathbf{a}_2)$ and the U -axis is chosen to coincide with the x -axis. Then in cylindrical coordinates the position of the first carbon atom in the nanotube is given by [46]

$$\mathbf{r}_{000} = (r_0, \Phi_0, z_0) = (d/2, 2\pi \frac{n_1+n_2}{2N}, \frac{n_1-n_2}{2\sqrt{3N}} a_0), \quad (2.18)$$

where $2N = nq\mathcal{R} = 2(n_1^2 + n_1n_2 + n_2^2)$. An element $(C_q^w | \frac{na}{q})^t C_n^s U^u$ acting on the atom maps it onto the new position

$$\begin{aligned} \mathbf{r}_{tsu} &= (C_q^{wt} C_n^s U^u | t \frac{na}{q}) \mathbf{r}_{000} \\ &= \left[d/2, (-1)^u \Phi_0 + 2\pi \left(\frac{wt}{q} + \frac{s}{n} \right), (-1)^u z_0 + \frac{tn}{q} a \right], \end{aligned} \quad (2.19)$$

where $u = 0, 1, s = 0, 1, \dots, n-1$, and $t = 0, \pm 1, \pm 2, \dots$. With the help of Eq. (2.19), the positions of all carbon atoms can be constructed for any nanotube. We summarize the symmetry properties in Table 2.2.

2.2.2 Symmetry-based quantum numbers

A given symmetry of a system always implies the conservation law for a related physical quantity. Well-known examples in empty space are the conservation of linear momentum caused by the translational invariance of space or the conservation of the angular momentum (isotropy of space). The rotational symmetry of an atomic orbital reflects the conserved angular-momentum quantum number. The most famous example in solid-state physics is the Bloch theorem, which

states that in the periodic potential of the crystal lattice the wave functions are given by plane waves with an envelope function having the same periodicity as the crystal lattice.

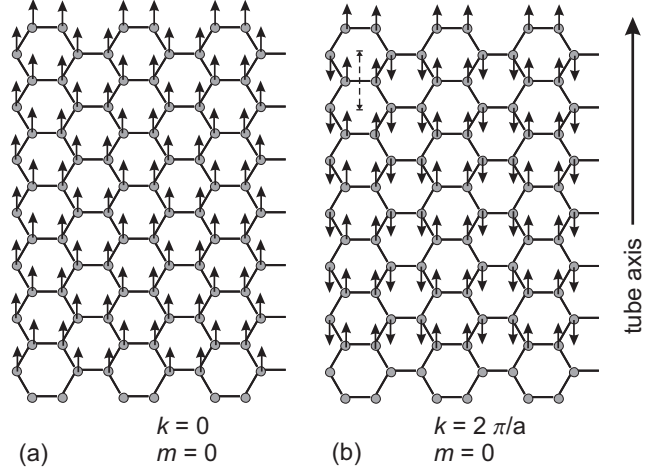
Likewise, any quasi-particle of the nanotube or a particle that interacts with it “feels” the nanotube symmetry. The state of the (quasi-) particle then corresponds to a particular representation of the nanotube line group, *i. e.*, its wave function is transformed in the same way by the symmetry operations as the basis functions of the corresponding representation. Using this, we can calculate selection rules for matrix elements, according to which a particular transition is allowed or not. The probability for a transition from state $|\alpha\rangle$ to state $|\beta\rangle$ via the interaction X is only non-zero, if $\langle X|\alpha\rangle$ and $\langle\beta|$ have some components of their symmetry in common. If they do not share any irreducible component, their wave functions are orthogonal and the matrix element $\langle\beta|X|\alpha\rangle$ vanishes [67–70]. X can be, *e.g.*, the dipole operator of an optical transition.

In the next section we describe the irreducible representations of the carbon-nanotube line groups in more detail. Here, we first introduce two types of quantum numbers to characterize the quasi-particle states in carbon nanotubes and show their implications for conservation laws.

We start by describing the general state inside the Brillouin zone by the quasi-linear momentum k along the tube axis and the quasi-angular momentum m . The first corresponds to the translational period; the latter to both the pure rotations and the screw-axis operations [47]. These states $|km\rangle$ are shown by the lines forming the Brillouin zone, as depicted in Fig. 2.4 for achiral tubes. For $k = 0, \pi/a$ and $m = 0, n$ the state is additionally characterized by its even or odd parity with respect to the U -axis. Achiral tubes have additionally the parity with respect to the vertical and horizontal mirror planes. k is a fully conserved quantum number, since it corresponds to the translations of the tube, which by themselves form a group \mathbf{T} . In contrast, m arises from the isogonal point group \mathbf{D}_q , which is not a subgroup of the nanotube line group. Therefore, m is not fully conserved and care has to be taken when calculating selection rules. As long as the process remains within the first Brillouin zone $(-\pi/a, \pi/a]$ for achiral tubes and within the interval $[0, \pi/a]$ for chiral tubes, m can be regarded as a conserved quantum number. But if the Brillouin zone boundary or the Γ point is crossed, m is no longer conserved. Such a process is often called an *Umklapp* process.

The change of m in *Umklapp* processes is illustrated in Fig. 2.7. A graphene rectangle is shown, which is an unrolled (3,3) tube. The arrows indicate the displacement vectors of the atoms along the tube axis. In (a), the translation of the tube along the tube axis is shown. This mode has infinite wavelength along the tube axis and along the circumference, *i.e.*, $k = 0$ and $m = 0$. If we want to relate the displacement in (b) to the z -translation, we find two solutions. First, if we view the displacement as a Γ -point mode, we find $2n = 6$ nodes along the circumference. The vibrational state in (b) is then characterized by $k = 0$ and $m = n$.

Figure 2.7: Phonon eigenvectors for an unwrapped (3,3) tube. The arrows indicate the atomic displacements. In (a) the translation of the tube along the tube axis is shown. This vibration has infinite wavelength ($k = 0$) and zero nodes along the circumference $m = 0$. The vibration in (b) can be understood as a Γ -point mode with $2n = 6$ nodes along the circumference. Alternatively, we can view the displacement as an $m = 0$ vibration with $\lambda = a$ (dashed line). Thus the same displacement pattern can be understood as a mode with $k = 0$ and $m = n$ or as a mode with $k = 2\pi/a$ and $m = 0$.



Alternatively, we can regard the vibration in (b) as an $m = 0$ mode, as in (a). The wavelength of the vibration is in this case $\lambda = a$ (dashed line). Thus the state with $k = 2\pi/a$ and $m = 0$ is equivalent to the state with $k = 0$ and $m = n$. In this example, m jumps by n when going into the second Brillouin zone. This holds in general for achiral tubes. In an *Umklapp* process m changes into m' according to the following rules [63]

$$m' = (m \pm n) \bmod q \quad (\text{achiral tubes}). \quad (2.20)$$

In chiral tubes, the *Umklapp* rules are [64]

$$\begin{aligned} m' &= (m + p) \bmod q && \text{when crossing the zone boundary at } \pi/a \\ m' &= -m && \text{when crossing the } \Gamma \text{ point,} \end{aligned} \quad (2.21)$$

where p is given by

$$p = q \operatorname{Fr} \left[\frac{nR}{q} \cdot \frac{q \cdot \left(\frac{2n_2 + n_1}{nR} \right)^{\varphi((2n_1 + n_2)/nR) - 1} - n_2}{2n_1 + n_2} \right]. \quad (2.22)$$

$\operatorname{Fr}[x]$ is again the fractional part of the rational number x and $\varphi(n)$ the Euler function [66]. Note that for achiral tubes $p = n$ and Eq. (2.21) becomes Eq. (2.20).

Another illustration for these *Umklapp* rules was shown in Fig. 2.4. Let us follow the nanotube Brillouin zone along the allowed wave vectors (white lines). We start with a line given by $k \in [0, \pi/a]$ and index m . From the symmetry of the graphene hexagonal Brillouin zone and the contour plot it is seen that following this line in the interval $[\pi/a, 2\pi/a]$ yields the same parts of the Brillouin zone as following the line with $m' = n - m$ from $k = -\pi/a$ to $k = 0$. This corresponds to application of Eq. (2.20).

Instead of the conventional “linear” quantum numbers k and m , the so-called “helical” quantum numbers, \tilde{k} and \tilde{m} , can be used [47, 71–73]. The helical quantum numbers are fully

conserved. In contrast to m , the new quantum number \tilde{m} corresponds to the *pure* rotations of the nanotube, which form the subgroup \mathbf{D}_n of the nanotube-line group. Therefore, \tilde{m} is fully conserved and takes n integer values in the interval $(-n/2, n/2]$. The screw-axis operations are incorporated in \tilde{k} , which can be considered as a “helical” momentum. Because the screw-axis operations including pure translations form the subgroup \mathbf{T}_q^w , \tilde{k} , too, is a conserved quantum number in carbon nanotubes. The minimum roto-translational period is now $\frac{n}{q}a$, and $\tilde{k} \in (-\tilde{\pi}/a, \tilde{\pi}/a]$, where $\tilde{\pi} = \pi q/n$.³ In the Brillouin zone “BZ” defined by \tilde{k}, \tilde{m} there are as many states as in the conventional Brillouin zone. The number of lines indexed by m is reduced by a factor q/n , while the interval $(-\pi/a, \pi/a]$ for k is extended by the same factor for \tilde{k} . The linear and helical quantum numbers can be transformed into each other by the following equations [74]

$$|\tilde{k}, \tilde{m}\rangle = \left| k + \frac{wm}{n} \frac{2\pi}{a} + \tilde{K} \frac{2\tilde{\pi}}{a}, m + \tilde{M}n \right\rangle \quad (2.23)$$

$$|k, m\rangle = \left| \tilde{k} - \frac{w\tilde{m}}{n} \frac{2\pi}{a} + K \frac{2\pi}{a}, \tilde{m} - Kp + Mq \right\rangle. \quad (2.24)$$

Here, \tilde{K}, \tilde{M}, K , and M are integers determined by the condition that the quantum numbers are in the intervals

$$k \in \left(-\frac{\pi}{a}, \frac{\pi}{a}\right] \quad m \in \left(-\frac{q}{2}, \frac{q}{2}\right] \quad (2.25)$$

$$\tilde{k} \in \left(-\frac{q\pi}{na}, \frac{q\pi}{na}\right] \quad \tilde{m} \in \left(-\frac{n}{2}, \frac{n}{2}\right]. \quad (2.26)$$

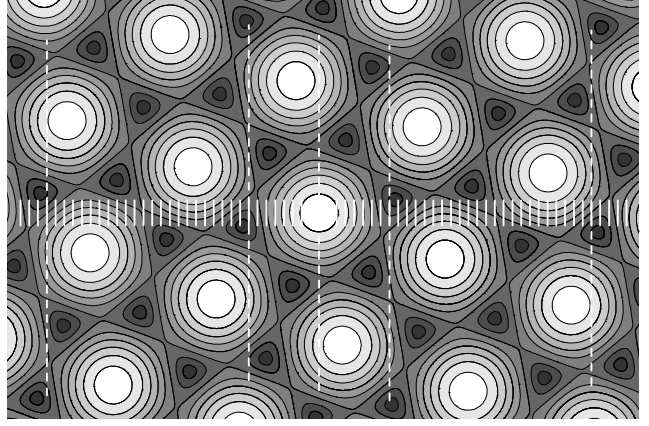
Figure 2.8 illustrates the relation between the “ k, m ” and the “ \tilde{k}, \tilde{m} ” quantum numbers for a (10,5) tube. The number of atoms in the unit cell is $2q = 140$; the linear quantum number $m \in (-q/2, q/2]$ takes $q = 70$ values. Thus the conventional Brillouin zone of the (10,5) tube consists of 70 equidistant lines, which are depicted by the short solid white lines in Fig. 2.8. Their direction is parallel to the tube axis, their length is $2\pi/a$, where the translational period $a = 11.3 \text{ \AA}$, and their distance is $2/d$. The BZ indicated by the dashed white lines consists of $n = 5$ lines indexed by \tilde{m} . Their length is $2\frac{q}{n}\frac{\pi}{a} = 28\frac{\pi}{a}$. At $\tilde{k} = 0$ and $\tilde{m} = 0$ is the Γ point of graphene, *i.e.*, $k = 0$ and $m = 0$. We will see in Sects. 4.3 and 5.2 that for chiral tubes the helical quantum numbers are much more helpful than the linear quantum numbers for, *e.g.*, displaying the phonon dispersion and using it in further calculations.

2.2.3 Irreducible representations

In this section we introduce the irreducible representations of the carbon-nanotube symmetry groups. We shall explain the line-group notation used in Refs. [63] and [47], which, in contrast to the more common molecular notation of crystal point groups, includes the full space group.

³Note that all intervals are defined modulo these intervals.

Figure 2.8: Brillouin zone of the (10,5) tube. The background is a contour plot of the conduction band of graphene; the darkest points are at the K point; the white points are the Γ point of graphene. The short solid white lines indicate the Brillouin zone of the (10,5) tube given by the quantum numbers k and m ; it is formed by $q = 70$ parallel lines of length $2\pi/a$. The dashed white lines form the equivalent Brillouin zone given by the quantum numbers \tilde{k} and \tilde{m} . There are $n = 5$ lines; their length is $2\tilde{\pi}/a = 28\pi/a$.



For a group consisting of rotations only, all irreducible representations would be one-dimensional, since a cyclic group is an abelian group [67]. We thus have to examine the other generating elements of the groups $T_{2n}^1 D_{nh}$ and $T_q^w D_n$ to determine the dimensions of the irreducible representations. The other generating elements are the mirror planes for achiral tubes and the U -axis for both chiral and achiral tubes. We start again with a general state $|km\rangle$ with $k \in (0, \pi/a)$ and $m \in (0, q/2)$. The U -axis maps the state $|km\rangle$ into $|-k-m\rangle$ and hence a two-dimensional irreducible representation exists with the basis $\{|km\rangle, |-k-m\rangle\}$. The action of the two-fold rotation about the U -axis onto $\{|km\rangle, |-k-m\rangle\}$ can be written as

$$\begin{pmatrix} |-k-m\rangle \\ |km\rangle \end{pmatrix} = \begin{pmatrix} 0 & 1 \\ 1 & 0 \end{pmatrix} \begin{pmatrix} |km\rangle \\ |-k-m\rangle \end{pmatrix}. \quad (2.27)$$

The symmetry groups of chiral tubes contain no further generating elements, thus the irreducible representations of the groups $T_q^w D_n$ are either one- or two-dimensional.

In achiral tubes, in addition, the vertical and horizontal mirror planes map the state $|km\rangle$ into $|k-m\rangle$ (vertical mirror plane) or into $|-km\rangle$ (horizontal mirror plane). Therefore, the irreducible representations describing a state inside the Brillouin zone are four-dimensional. If we choose the basis as $\{|km\rangle, |k-m\rangle, |-km\rangle, |-k-m\rangle\}$, the action of, *e.g.*, σ_x can be written as

$$\begin{pmatrix} |k-m\rangle \\ |km\rangle \\ |-k-m\rangle \\ |-km\rangle \end{pmatrix} = \begin{pmatrix} 0 & 1 & 0 & 0 \\ 1 & 0 & 0 & 0 \\ 0 & 0 & 0 & 1 \\ 0 & 0 & 1 & 0 \end{pmatrix} \begin{pmatrix} |km\rangle \\ |k-m\rangle \\ |-km\rangle \\ |-k-m\rangle \end{pmatrix}. \quad (2.28)$$

The irreducible representations of the groups $T_{2n}^1 D_{nh}$ are thus one-, two- or four-dimensional. Note that the degeneracy of k and $-k$ in both chiral and achiral tubes is specific to the line-group notation. In contrast, it is common not to count this degeneracy. In this case, chiral

tubes possess only non-degenerate representations and achiral tubes one- or two-dimensional representations.

The examples given in Eq. (2.27) and Eq. (2.28) for chiral and achiral tubes, respectively, apply to a state $|km\rangle$ inside the Brillouin zone. At the Brillouin zone edges, on the other hand, states with k and $-k$ are the same; m and $-m$ describe the same quantum number if $m = 0$ or $m = q/2$. Then the dimension of the irreducible representation is reduced. Additionally, states at the Brillouin-zone edges are characterized by parity quantum numbers with respect to the U -axis and, in achiral tubes, to the mirror planes. The *Umklapp* rules, Eqs. (2.20) and (2.21), are reflected by the fact that at the Brillouin zone boundaries the bands m are degenerate with the bands $m' = (m + p) \bmod q$ [75]. An overview of the irreducible representations, degeneracy as well as symmetry of polar and axial vectors and their symmetric and antisymmetric products can be found in Ref. [75].

In the following we explain the line-group notation for the irreducible representations:

$$\begin{array}{l} \text{wave vector} \rightarrow kX_m^\pi \quad \begin{array}{l} \leftarrow \sigma_h / U\text{-axis parity} \\ \leftarrow m \text{ quantum number} \end{array} \\ \quad \quad \quad \uparrow \\ \quad \quad \quad \text{dimension } (X = A, B, E, G). \end{array}$$

X is given by a letter that indicates the dimension of the representation: A and B are one-dimensional, E two-dimensional, and G four-dimensional representations. For achiral tubes, A and B give at the same time the parity quantum number with respect to the σ_x operation. A corresponds to even and B to odd parity. In chiral tubes at $k = 0$, the subscript $+$ or $-$ denotes even or odd parity under the U -axis operation and, in achiral tubes, under the σ_h operation. For example, in achiral tubes ${}_0B_0^-$ is the one-dimensional irreducible representation of a Γ -point state ($k = 0$) with zero nodes around the circumference ($m = 0$). This state has odd parity under both the vertical (B) and the horizontal ($-$) reflections. In chiral tubes, ${}_kE_2$ denotes a two-fold degenerate (E) state inside the Brillouin zone, *i.e.*, $k \neq 0$ and $k \neq \pi/a$, with 4 nodes around the circumference ($m = 2$). This state has no defined parity under rotation about the U -axis. A summary of all irreducible representations of chiral and achiral carbon nanotubes is given in Tables A1 and A2 of Ref. [47].

The irreducible representations at $k = 0$ can be related to the more common molecular notation [76] of the corresponding isogonal point groups D_{2nh} and D_q . In chiral tubes, ${}_0A_0^+$ is the fully symmetric representation A_1 ; ${}_0A_0^-$ possesses odd parity under the U -axis operation and therefore corresponds to A_2 in the molecular notation. For $m = q/2$, the states have odd parity under rotation by $2\pi/q$ about the principal axis, thus the representations ${}_0A_{q/2}^+$ and ${}_0A_{q/2}^-$ translate into B_1 and B_2 , respectively. The degenerate representations ${}_0E_m$ are the same in the molecular notation (E_m).

Achiral tubes possess a center of inversion, thus the fully symmetric representation ${}_0A_0^+$ is A_{1g} in molecular notation; ${}_0A_0^-$ is A_{2u} . The correspondence of the degenerate representations

Table 2.3: Correspondence of the line-group notation for achiral tubes ($(L_{\mathcal{A},z})$) at the Γ -point to the molecular notation for the isogonal point group D_{2nh} . For chiral tubes, the subscripts “g” and “m” are omitted; n is replaced by $q/2$.

${}^0A_0^+$	${}^0A_0^-$	${}^0B_0^+$	${}^0B_0^-$	${}^0A_n^+$	${}^0A_n^-$	${}^0B_n^+$	${}^0B_n^-$	${}^0E_{\pm m}^+$	${}^0E_{\pm m}^-$
A_{1g}	A_{2u}	A_{2g}	A_{1u}	n even: B_{1g}	B_{2u}	B_{2g}	B_{1u}	m even: E_{mg}	E_{mu}
				n odd: B_{2u}	B_{1g}	B_{1u}	B_{2g}	m odd: E_{mu}	E_{mg}

${}^0E_m^\pm$ to E_{mg} or E_{mu} depends on whether m is even or odd. For example, we consider the representation ${}^0E_1^-$. The inversion of the achiral tube is given by the symmetry operation $\sigma_h C_{2n}^n$. The character of ${}^0E_1^-$ for the inversion is therefore $-2 \cos(nm2\pi/q) = +2$. Thus ${}^0E_m^-$ transforms into E_{mg} if m is odd. We summarize the relationship between the line-group and the molecular notation in Table 2.3. For chiral tubes, the subscripts “g” and “m” are omitted; n is replaced by $q/2$.

Finally, we want to give an example of the use of the line-group symmetry to calculate selection rules. We consider optical absorption in carbon nanotubes in the dipole approximation. The momentum operator has the same symmetry as a polar vector. The z -component of a polar vector in an achiral nanotube belongs to a non-degenerate representation. It has even parity with respect to the vertical mirror plane σ_x and odd parity under σ_h . Therefore, it transforms as the irreducible representation ${}^0A_0^-$. The x - and y -components are degenerate and have even parity with respect to σ_h , therefore given by ${}^0E_{\pm 1}^+$ [30]. In the dipole approximation, an optical transition between the states $|i\rangle$ and $|f\rangle$ is allowed if the representations of the polar vector and of the electronic states have a common component:

$$D^{|f\rangle} \otimes D^{pv} \otimes D^{|i\rangle} \supseteq {}^0A_0^+. \quad (2.29)$$

This can be evaluated in the standard way by using the character tables in Refs. [64] and [63]. More elegant and much faster, however, is the direct inspection of the quantum numbers. Because of its ${}^0A_0^-$ symmetry, z -polarized light can change neither m ($\Delta m = 0$), nor the σ_x parity (A). But since it carries a negative σ_h parity quantum number, it changes the σ_h parity of the quasi-particle it interacts with. Similarly, x/y -polarized light changes the m quantum number by $\Delta m = \pm 1$, but leaves the σ_h parity unchanged. For example, the electronic bands crossing at the Fermi level in armchair tubes (see Chap. 3) possess ${}_kE_n^A$ and ${}_kE_n^B$ symmetry. Between these two bands, an optical transition with z -polarized light ($\Delta m = 0$) is forbidden, because it cannot change the σ_x parity of the electronic states from A to B .

2.3 Summary

In this chapter we showed how to construct the atomic structure and the reciprocal lattice of carbon nanotubes from a given chiral vector (n_1, n_2) . Single-walled carbon nanotubes have line-group symmetry [46], *i.e.*, they possess a translational periodicity only along the tube axis. Within the concept of line groups, any state of a quasi-particle can be characterized by a set of quantum numbers consisting of the linear momentum k , the angular momentum m , and, at special points in the Brillouin zone only, parity quantum numbers. Only achiral tubes possess additional vertical and horizontal mirror planes. When crossing the boundaries of the Brillouin zone in a scattering process, special *Umklapp* rules apply, because m is not a fully conserved quantum number. Alternatively, a different set of quantum numbers can be used, the so-called helical quantum numbers. The notation and the application of the line-group symmetry for calculating selection rules are explained.

3 Electronic band structure

In resonant Raman scattering one or more of the electronic transitions are real, and the Raman signal is strongly enhanced. Thus the Raman intensity and, as we will show in Chap. 5 for double-resonant scattering, also the Raman frequency depend sensitively on the electronic band structure. In this chapter we summarize the basic properties of the carbon nanotube band structure, as we will use them in Chap. 5 for the calculation of the Raman spectra.

Carbon nanotubes can be metallic or semiconducting. The simplest argument for that is given by the zone-folding approach (Sect. 2.1), where the nanotube bands are obtained by cutting the graphene bands according to the allowed wave vectors: In graphene, the conduction and valence bands cross the Fermi level at singular points, the K points in the Brillouin zone [77]. Therefore, the tube is metallic, if the allowed states of the nanotube (Fig. 2.4) contain the graphite K point, otherwise it is semiconducting [31]. For example, in all armchair tubes the band with $m = n$ includes the K point, thus they are always metallic. In general, the tubes with chiral index (n_1, n_2) such that $(n_1 - n_2)/3$ is integer, are metallic in this approximation.

Figure 3.1 shows the band structures of the (10,10) and the (17,0) tube, obtained by zone folding of the graphene π and π^* bands. These were calculated within the tight-binding approximation including third-nearest neighbors, where the parameters were fit to the bands from *ab-initio* calculations in the visible range of transition energies [78]. The (10,10) tube is metallic with the Fermi wave vector k_F at $2/3$ of the Brillouin zone; the (17,0) tube is semiconducting. The bands near the Fermi level are labeled by their symmetry (for the (17,0) tube the Γ -point symmetry) [47, 75]. As an example for a chiral tube we show the band structure of the (16,4) tube in Fig. 3.2. The bands are given by the helical (\tilde{k}, \tilde{m}) quantum numbers. The (16,4) tube is metallic as well in this approximation, again with the Fermi wave vector at $2/3$ of the helical Brillouin zone. In general, the Fermi wave vector or, in semiconducting tubes, the wave vector of the lowest transition energies is at the Γ point in tubes with $\mathcal{R} = 1$ and at $2/3$ of the Brillouin zone in $\mathcal{R} = 3$ tubes [79].

The transition energies are to first approximation proportional to the inverse tube diameter [80, 81]. This is easily understood from the zone-folding approach, assuming linear, isotropic bands at the graphite K point. Since the distance between two lines of the nano-

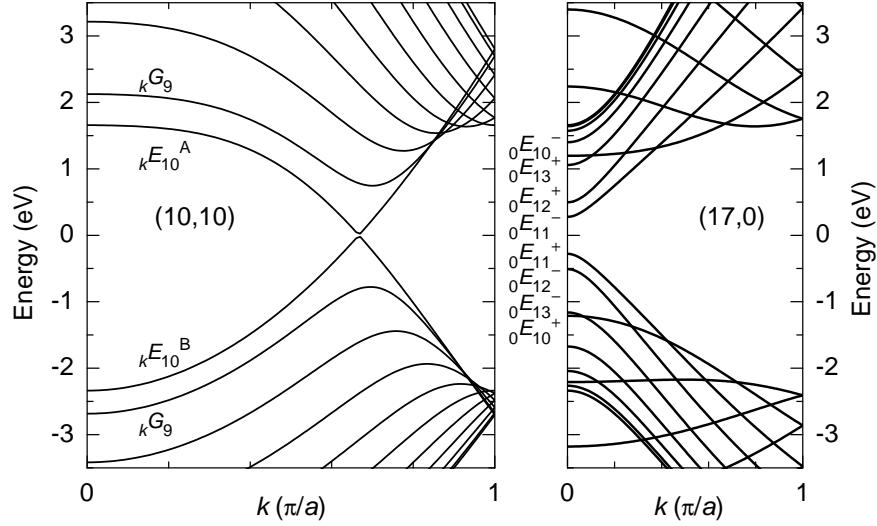
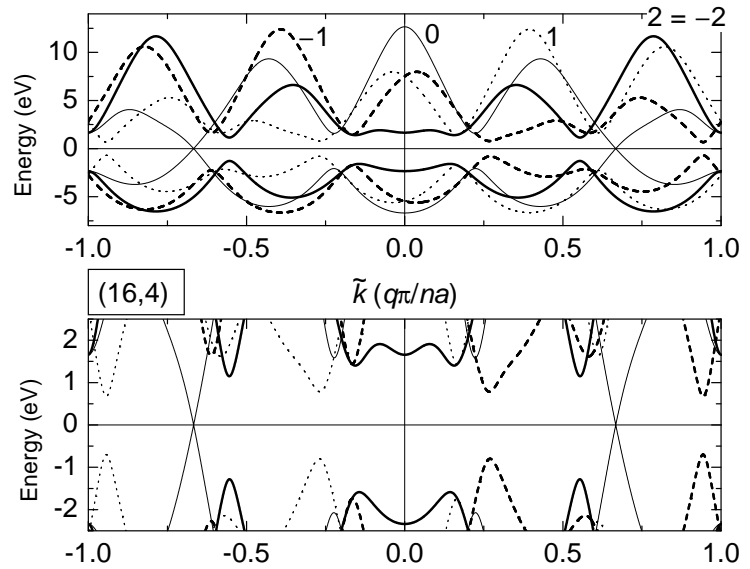


Figure 3.1: Band structure of the (10,10) armchair and of the (17,0) zig-zag tube calculated from the third-nearest neighbor tight-binding approximation [78]. The lowest electronic states are labeled by their symmetry (irreducible representations) according to the line-group notation explained in Sect. 2.2.3 [75]. The (10,10) tube is metallic, because the bands with $m = n = 10$ cross at the Fermi level. The Fermi wave vector k_F is at $2/3$ of the Brillouin zone. Optical transitions between these two bands are forbidden because of the A/B parity quantum numbers with respect to the vertical mirror plane. The (17,0) tube is semiconducting; the band gap is determined by the bands with m closest to $2n/3$.

Figure 3.2: Electronic band structure of the (16,4) tube given by (\tilde{k}, \tilde{m}) quantum numbers, calculated from the third-nearest neighbors tight-binding approximation. The \tilde{m} indices are given next to the bands; the thin solid line indicates $\tilde{m} = 0$, the dotted and dashed lines $\tilde{m} = +1$ and $\tilde{m} = -1$, respectively, and the thick solid line $\tilde{m} = 2$. The states with $\tilde{m} = 2$ are identical to those with $\tilde{m} = -2$, therefore the band is symmetric with respect to the Γ point, as well as the band $\tilde{m} = 0$. States given by (\tilde{k}, \tilde{m}) are degenerate with those given by $(-\tilde{k}, -\tilde{m})$, see Chap. 2. In the (16,4) tube, $q/n = 56/4 = 14$. Bottom: Same band structure but restricted to the visible energy range of light.



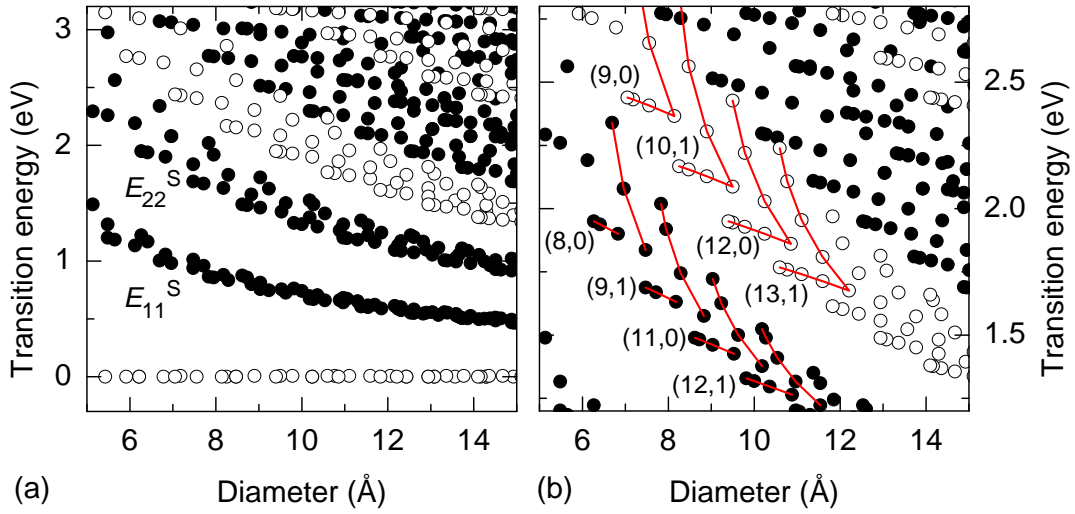


Figure 3.3: Transition energies of carbon nanotubes as a function of diameter (so-called Kataura plot [82]) from a third-nearest neighbor tight-binding calculation. Closed symbols indicate semiconducting tubes; open circles are metallic tubes. E_{11}^S and E_{22}^S are the first and second transitions in semiconducting tubes, respectively. (a) The transition energies follow roughly a $1/d$ dependence, where the systematic deviations from this behavior increase with smaller diameter and with increasing excitation energy. (b) Enlarged part of E_{22}^S and E_{11}^M from (a). The lines connect nanotubes with $(n'_1, n'_2) = (n_1 - 1, n_2 + 2)$; the chiral indices of the tubes at the outermost position on the lower side of the semiconducting and of the metallic families are given. The lower branches of the E_{22}^S transitions consist of the tubes with $(n_1 - n_2) \bmod 3 = -1$, the tubes in the upper branches have $(n_1 - n_2) \bmod 3 = +1$.

tube Brillouin zone is $2/d$, the energies obtained by cutting the graphene bands for different tubes increase linearly with the inverse diameter. Systematic deviations from the $1/d$ dependence are seen when the three-fold symmetry of the bands around the K point is taken into account (so-called trigonal warping, see also the contour plot of the graphene conduction band in Fig. 2.4). These deviations are even stronger if graphene bands obtained from *ab-initio* calculations or tight-binding results including third-nearest neighbors interaction [78] are used in the zone-folding procedure. The third-nearest neighbor tight binding results agree throughout the Brillouin zone much better with the *ab-initio* calculation in the local-density approximation than the usual nearest-neighbors tight-binding expression [78].

We show in Fig. 3.3 the transition energies obtained from the third-nearest neighbor tight-binding approach as a function of tube diameter. Such a plot, usually shown for the simple nearest-neighbor approximation, is commonly referred to as a Kataura plot [82]. Filled and open circles indicate semiconducting and metallic tubes, respectively. The energies form v-like branches below and above the $1/d$ line, as can be seen clearly in (b). The lines connect tubes with $(n'_1, n'_2) = (n_1 - 1, n_2 + 2)$, where the zig-zag or small-chiral angle tubes are at the outer positions. The chiral angle increases along such a branch towards the inner position; for the metallic tubes, the inner tubes are of armchair type. For example, the branch starting with the

(9,0) tube consists of the (9,0), (8,2), (7,4), and (6,6) tube. Within the semiconducting E_{22}^S transitions, the lower-branch tubes belong to the $(n_1 - n_2) \bmod 3 = -1$ family, whereas the tubes in the upper branches have $(n_1 - n_2) \bmod 3 = +1$, and *vice versa* for the E_{11}^S transitions. The $(n_1 - n_2) \bmod 3 = \pm 1$ family reflects from which side of the K point the electronic bands result in the zone-folding scheme. In the nanotubes with $(n_1 - n_2) \bmod 3 = -1$ the first transition (E_{11}^S) comes from between the Γ and K point, and the second transition (E_{22}^S) from between the K and M point. The opposite situation occurs for the $(n_1 - n_2) \bmod 3 = +1$ nanotubes. Since the dispersion of the electronic bands is different in the Γ - K and the K - M directions, this results in systematic differences in the transition energy.

So far we did not include any effects of curvature, instead we treated the nanotube as a flat rectangle from graphene with periodic boundary conditions. Blase *et al.* [83] first pointed out that mixing and rehybridization of the π and σ orbitals in the curved graphite sheet can significantly change the electronic band structure. These effects become particularly strong for small-diameter nanotubes. For example, the (5,0) tube is metallic in contrast to what is expected from zone folding [84]. Moreover, the rehybridization effects as seen when comparing *ab-initio* calculations with zone-folding results, are larger for zig-zag (small chiral angle) tubes than for armchair tubes [85]. The deviation from the zone-folding bands is particularly large for those transition energies that belong to the lower branches in Fig. 3.3 (b), and small for the upper branches. This means that the lower branches are in fact bent downwards towards the small-chiral angle tubes. Such a strong down-bending shape was recently confirmed experimentally, where the transition energies were obtained by resonance Raman profiles [86], and by photoluminescence excitation experiments [36–38].

A geometrical effect of the curvature is the small secondary gap opening at the Fermi level in all chiral tubes that were above predicted to be metallic ($(n_1 - n_2) \bmod 3 = 0$) [72, 79]. This can be understood from the structure of the curved graphite sheet, where the three bonds between a carbon atom and its neighbors differ in length. Armchair tubes have still a zero gap, if the geometry of the curved sheet is taken into account, but the Fermi wave vector shifts [79]. Alternatively, the opening of the gap can be understood as a consequence of symmetry: only in armchair tubes the two electronic states at the Fermi level possess different quantum numbers, *i.e.*, the A/B parity with respect to the vertical reflection, see Fig. 3.1. In chiral tubes, in contrast, the vertical mirror planes are absent; both electronic states would have the same quantum numbers. Therefore, an anti-crossing of the bands occurs, resulting in the small gap at the Fermi level in chiral tubes; only armchair tubes are thus truly metallic.

In summary, the electronic band structure of carbon nanotubes can be reasonably well predicted by zone folding of the third-nearest neighbor tight-binding results, as is seen from the good agreement with the *ab-initio* calculations. On the other hand, the excited electronic states

are typically underestimated by $\approx 10\%$ in local-density calculations. The transition energies on the lower branches in the Kataura plot in Fig. 3.3 (b) depend stronger on the chiral angle than predicted by zone folding. Excitonic effects have to be considered as well, see Refs. [87, 88]. Therefore, from a single measurement of the optical transition energy one cannot determine the diameter or even the chirality of the tube as was sometimes attempted. Nevertheless, zone folding combined with the third-nearest neighbor tight-binding approach provides an easy calculation of the band structure for any chirality of nanotubes. In particular, the position of the optical transitions in the Brillouin zone and the overall shape of the electronic bands are correctly predicted [78]. Therefore, we will use the electronic band structure from this approximation in Chap. 5 in the modeling of the Raman spectra.

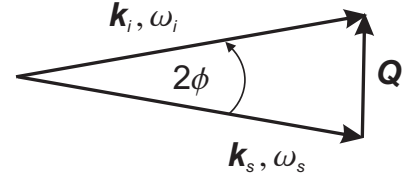
4 Phonons in graphite and carbon nanotubes

Phonons are the quasi-particles that describe the quantized lattice vibrations or normal modes of a crystal. The crystal possesses $3N$ phonon branches where N is the number of atoms in the unit cell. A three-dimensional crystal has three acoustic modes with zero frequency at the Γ point, corresponding to uniform displacements of the crystal. All remaining branches, where the atoms in the unit cell move out-of-phase, are referred to as optical phonons, since in polar crystals they can directly couple to light [89]. Phonons are bosons and contribute the major part to the heat capacity of a crystal. They play an important role for both transport and optical properties, because they are main path by which excited electrons or other quasi-particles can decay into lower energy states. In fact, in an ideal crystal at finite temperature phonons are the only source of electrical resistance.

The knowledge of the phonon modes, of their dispersion and of the selection rules governing their interaction with other quasi-particles is therefore essential for a consistent understanding of optical spectra and electrical transport characteristics. Information on the properties of the phonons can be obtained from direct absorption of light by phonons (infrared spectroscopy, for carbon nanotubes see Ref. [90,91]), measurements of the specific heat and the phonon density of states [92–94], Raman scattering (Chap. 5), or from transport experiments. In principle, the phonon dispersion of a crystal can be measured by inelastic scattering of neutrons, electrons, or X-ray photons. For these experiments, a minimum size of a single crystal is required, which is not available from carbon nanotubes at present. The closest experimental approximation to the phonon dispersion of carbon nanotubes is therefore the in-plane phonon dispersion of graphite.

Even in graphite the phonon dispersion was not known from experiments, because the standard method of inelastic neutron scattered requires single crystals on the order of cm in size, which do not exist. For the novel method of inelastic X-ray scattering, on the other hand, single crystals $\sim 100\mu\text{m}$ are sufficient. We describe the experimental technique of inelastic X-ray scattering in Sect. 4.1 and present the experimental phonon dispersion of graphite in

Figure 4.1: Definition of the quasi-momenta in the inelastic scattering process. \mathbf{k}_i and \mathbf{k}_s are the wave vectors of the incoming and scattered light, respectively. $\mathbf{Q} = \mathbf{q} \pm \mathbf{H}$, where \mathbf{H} is a reciprocal lattice vector. The angle between \mathbf{k}_i and \mathbf{k}_s is defined as 2ϕ for convenience.



Sect. 4.2. In Sect. 4.3 we discuss the phonon properties of carbon nanotubes, including their relation to graphite, their symmetry and eigenvectors, and force-constants calculations of their dispersion.

4.1 Inelastic light scattering

The dispersion relation of quasi-particles in a crystal can experimentally be determined from the transfer of quasi-momentum and energy in an inelastic scattering process. For example, by inelastic scattering of neutrons the phonon dispersion of many solids has been measured, such as Si, Ge, GaAs, and diamond [95–99].

In the following we will discuss inelastic scattering of light by phonons to study the relation between their wave vector \mathbf{q} and energy $\hbar\omega_{ph}$; the general principles apply to inelastic scattering by other quasi-particles as well. In Fig. 4.1 we define the wave vectors \mathbf{k}_i and \mathbf{k}_s of the incoming and scattered light, respectively, and the scattering wave vector (wave vector transfer) $\mathbf{Q} = \mathbf{q} \pm \mathbf{H}$, where \mathbf{H} is a reciprocal lattice vector of the crystal. The conservation of quasi-momentum and energy reads

$$\mathbf{k}_i = \mathbf{k}_s + \mathbf{q} \pm \mathbf{H} \quad (4.1)$$

$$\hbar\omega_i = \hbar\omega_s \pm \hbar\omega_{ph}, \quad (4.2)$$

where the plus and minus sign, respectively, indicate the creation and annihilation of a phonon. The magnitude $|\mathbf{Q}| = Q$ of the wave vector transfer is given by

$$Q^2 = k_i^2 + k_s^2 - 2k_i k_s \cos(2\phi), \quad (4.3)$$

where 2ϕ is the angle between \mathbf{k}_i and \mathbf{k}_s , see Fig. 4.1. If $|\mathbf{k}_i| \approx |\mathbf{k}_s|$,

$$Q \approx 2k_i \sin \phi. \quad (4.4)$$

This approximation applies to inelastic scattering of light by phonons: the phonon energy is typically 1 – 2 orders of magnitude smaller than the photon energy in the visible range. For example, the longitudinal optical (LO) phonon in GaAs is at 36 meV, whereas the energy of

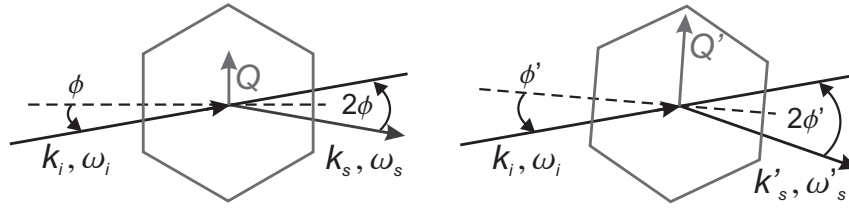


Figure 4.2: The magnitude of the momentum transfer is varied by changing the scattering angle 2ϕ . To conserve the direction of the wave vector \mathbf{Q} , the sample (indicated by the hexagon) has to be rotated by $\Delta 2\phi/2$.

visible light is around 2.5 eV. Thus incoming and scattered light have almost the same energy and therefore momentum. When changing the scattering angle 2ϕ by $\Delta(2\phi) = 2\phi' - 2\phi$, the magnitude of the scattering wave vector \mathbf{Q} is varied, see Fig. 4.2. The direction of \mathbf{Q} is kept the same, if the sample is simultaneously rotated by $\Delta(2\phi)/2$. The maximum momentum transfer is obtained for $2\phi = 180^\circ$ (backscattering geometry) with $Q = 2k_i$.

In the visible range, inelastic scattering of light by phonons is called Raman scattering [100]. The wave vector of visible light $k_i = 2\pi n/\lambda$ is on the order of $5/10^2 \text{ nm}^{-1} = 0.5 \times 10^{-2} \text{ \AA}^{-1}$ at $\lambda = 500 \text{ nm}$ in a material with refractive index $n = 4$. In contrast, the extension π/a of the Brillouin zone, *i.e.*, the range of phonon wave vectors, is typically $\sim 1 \text{ \AA}^{-1}$. Therefore, the maximum momentum transfer $Q = 2k_i$ is by about two orders of magnitude smaller than π/a , and only Γ -point phonons ($q \approx 0$) can be probed by conventional Raman scattering.

In order to measure phonons from the entire Brillouin zone, either the photon energy (and hence momentum) has to be increased by several orders of magnitude into the X-ray range ($\sim 10 \text{ keV}$), or higher-order Raman processes have to be studied. In higher-order Raman scattering, two or more phonons are involved. Then the $q \approx 0$ rule can be fulfilled by two phonons with large but opposite wave vector and $q_1 + q_2 \approx 0$. Another higher-order process includes elastic scattering by defects instead of scattering by a second phonon. Usually, however, it is not possible to measure the phonon dispersion relation by higher-order scattering. All phonon wave vectors contribute simultaneously to the spectra, and the second-order Raman spectra resemble the phonon density of states [101]. An exception to this are resonant higher-order Raman processes where particular phonon modes are enhanced, depending on the excitation energy [102]. Such processes allow a mapping of the phonon dispersion and will be discussed in detail in Chap. 5. Here we follow the first approach, *i.e.*, first-order Raman scattering using X-rays for excitation, and present the measurement of the phonon dispersion relations in graphite.

4.1.1 Inelastic X-ray scattering: experiment

Inelastic X-ray scattering for measuring phonon dispersion relations is a comparatively young experimental technique. The first experiments were carried out about 15 years ago [103], for a review see Ref. [104]. Although inelastic neutron scattering has been used for measuring phonon dispersion relations for several decades already and become a standard technique [95, 96, 105, 106], there are several advantages of using X-rays instead of neutrons for excitation. Inelastic X-ray scattering can be applied to relatively small samples, for example for investigations under high pressure in a diamond anvil cell [107] or if only small amounts of the sample are available.

One major challenge is the high energy resolution of $\Delta E/E \approx 10 \text{ meV}/10 \text{ keV} = 10^{-6}$ that is required in order to detect the inelastically scattered light only $\Delta E \sim 10 \text{ meV}$ apart from the elastically scattered signal at $\sim 10 \text{ keV}$ and moreover to measure the typically flat dispersion of optical phonons. This high resolution can be achieved by using Bragg reflection in backscattering geometry from single crystals for the main monochromators [103].

We performed the inelastic X-ray scattering at the beamline ID28 at the European Synchrotron Radiation Facility. The experimental setup is schematically drawn in Fig. 4.3. The white beam is first pre-monochromatized and then backscattered from a second, high-resolution monochromator. The selected photon energy was 17794 eV. The monochromators are single crystals of Si; in the present experiment we used the (999)-reflection plane for the backscattering monochromator, resulting in an energy resolution of 3.1 meV. The energy difference between incident and scattered light was scanned by changing the temperature of the main monochromator. The temperature controls the lattice constant of the Si crystal and hence the wavelength selected by the Bragg condition. Here, a temperature difference of 1 K between main monochromator and analyzer corresponded to 46 meV energy difference between incoming and detected light. The advantage of this method of scanning the energy is that the monochromator is not rotated and the energy resolution is constant. In contrast to common Raman experiments the energy of the incoming light was varied, whereas the detection energy was kept constant. The energy axis was calibrated by setting the energy transfer to zero at the position of the Bragg peak. The beam can be focused by horizontal and vertical mirrors to a spot size of $30 \times 60 \mu\text{m}^2$ in the sample. The 7 m long spectrometer arm was equipped with a set of five analyzers, allowing the simultaneous detection from five different \mathbf{q} vectors.

By rotating the spectrometer arm, the scattering angle 2φ is selected. The sample is mounted on a goniometer head with the same vertical axis of rotation as the spectrometer arm, allowing to vary the angle φ between a given direction in the sample and the incoming beam. We show the selection of angles and wave vectors in Fig. 4.4 in more detail. In (a) an elastic scattering process, *i.e.*, Bragg reflection, is depicted in reciprocal space, using the

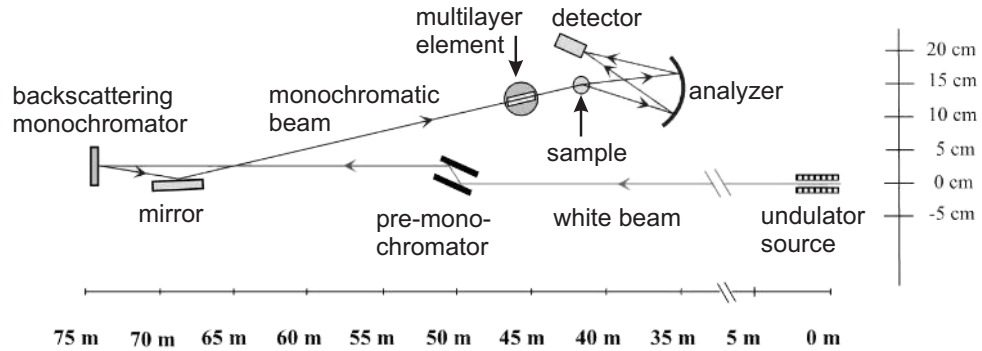


Figure 4.3: Experimental setup of the inelastic X-ray scattering at beamline ID28 at the European Synchrotron Radiation Facility. The monochromators select an energy of the incident beam of 17794 eV. The monochromatized beam is focused by the multilayer element (horizontal) and a cylindrical mirror (vertical) onto the sample. Rotation of the spectrometer arm and of the sample select the scattering wave vector \mathbf{Q} and the phonon wave vector \mathbf{q} . The monochromators and analyzers are formed by Si crystals; the detectors are Peltier-cooled Si diodes. From <http://www.esrf.fr>.

Ewald-construction [108, 109]. The dots indicate the reciprocal lattice of the crystal. In elastic scattering, incoming and scattered wave vectors have the same magnitude. The wave vector transfer \mathbf{Q} is exactly a reciprocal lattice vector \mathbf{H} , measuring in real space the distance between the lattice planes perpendicular to \mathbf{H} .

In Fig. 4.4 (b) an inelastic scattering process is shown, assuming again $k_i = k_s$ for inelastic X-ray scattering with phonons. The sample is rotated by an angle ϑ with respect to the incident beam. If the spectrometer arm, *i.e.*, the direction of \mathbf{k}_s , is rotated by 2ϑ , the direction of the wave vector transfer \mathbf{Q} is the same as in (a), but it has now a smaller magnitude $Q = H - q$. Thus inelastically scattered light is observed in the direction of \mathbf{k}_s . Its energy difference with respect to the incoming photon energy is equal to the phonon energy at wave vector \mathbf{q} . Note that the scattering angle “ 2φ ” is not always twice the angle “ φ ” of the sample. For example, to measure $\mathbf{q} \perp \mathbf{H}$ in Fig. 4.4 (b), the scattering angle “ 2φ ” has to be enlarged. If the *change* 2ϑ in scattering angle, however, is twice the change ϑ in the angle of the sample, the direction of a chosen scattering wave vector \mathbf{Q} remains constant.

The amplitude of the inelastically scattered light is proportional to

$$\sum_n \exp(-i(\mathbf{k}_s - \mathbf{k}_i + \mathbf{q}) \cdot \mathbf{r}_n) i\mathbf{Q} \cdot \mathbf{u} \exp(-i(\omega_i \pm \omega(\mathbf{q})t)), \quad (4.5)$$

where the sum runs over all atoms and \mathbf{u} indicates the displacement of the atoms. From this expression the common rule is derived that only phonon modes with polarization parallel to the scattering vector \mathbf{Q} can be observed.

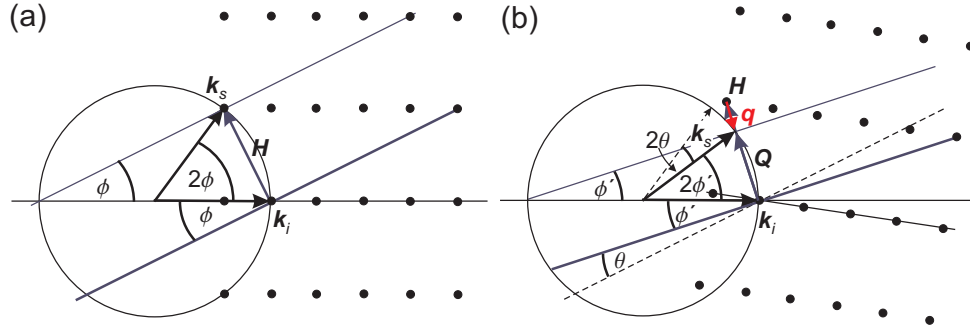


Figure 4.4: (a) Ewald construction for elastic X-ray scattering. The dots indicate the reciprocal lattice. The difference between the wave vectors of incoming and scattered light matches a reciprocal lattice vector \mathbf{H} . The lines perpendicular to \mathbf{H} are in the direction of the lattice planes. (b) Inelastic scattering process with $k_i = k_s$, where the wave vector transfer \mathbf{Q} differs from the reciprocal lattice vector \mathbf{H} by the phonon wave vector \mathbf{q} . The sample is rotated by ϑ such that the direction of \mathbf{Q} is still parallel to \mathbf{H} . The dashed lines indicate the direction of the lattice planes and of k_s in (a).

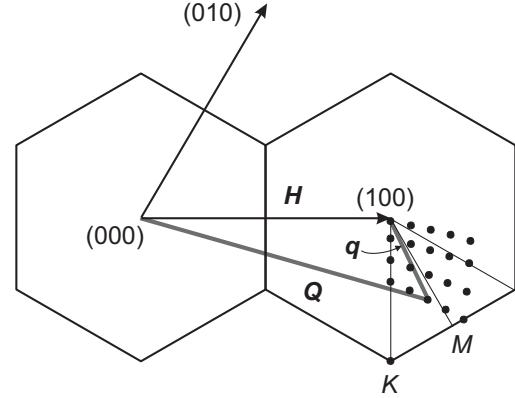
4.2 Phonon dispersion of graphite

The phonon dispersion of graphite was until now not fully determined from experiments. Inelastic neutron scattering provided the dispersion along the c -axis and only the acoustic branches up to 400 cm^{-1} in the basal plane [110]. The optical branches with frequencies up to 1600 cm^{-1} were partly measured by electron energy loss spectroscopy (EELS), but data were missing along the high-symmetry direction K - M and around the K point [111–113]. The main obstacle is the lack of large, single crystals of graphite. Although in some types of graphite samples the c -axis is very well oriented, such as in highly-ordered pyrolytic graphite (HOPG), the crystallites are usually not ordered with respect to the in-plane axes.

Because of the lack of experimental data, there exist a variety of partly contradicting theoretical models of the phonon dispersion of graphite [114–118]. They differ strongly in their slopes and absolute frequencies, resulting in different shapes of the optical branches with respect to crossing of the branches and local minima or maxima. Therefore, an experimental clarification of these discrepancies is needed.

For inelastic X-ray scattering, single crystals with a size $\sim 100 \mu\text{m}$ are sufficient. This technique is therefore perfectly suited for the determination of the full phonon dispersion relations of graphite. In this section we present our results on the optical phonon branches of graphite in all high-symmetry directions of the in-plane Brillouin zone. The sample was a natural flake of graphite [119]. It consisted of monocrystals with $100 - 200 \mu\text{m}$ length in the basal plane and a well-oriented c -axis. The experiment was performed as described in Sect. 4.1.1; the scattering plane was the basal plane. The small focal spot allowed us to select a specific

Figure 4.5: Measured \mathbf{Q} vectors corresponding to the five analyzers in several scans. The reciprocal lattice vectors \mathbf{k}_1 and \mathbf{k}_2 are given by (100) and (010), respectively. Note that the angle between \mathbf{k}_1 and \mathbf{k}_2 is 60° here, whereas it is 120° if the lattice vectors in real space form an angle of 60° . The setting of the analyzers was chosen such that one of them was always exactly on the Γ - K direction in each of the scans. The transverse modes were detected because \mathbf{Q} is almost perpendicular to the Γ - K direction. Those \mathbf{q} vectors that were not exactly along any high-symmetry direction, were projected onto the closest high-symmetry direction for the representation of the data in Fig. 4.9.



microcrystal of the sample during the entire experiment. In Fig. 4.5 we show an example of the five simultaneously measured \mathbf{Q} vectors for several scans.

As for optical absorption or conventional Raman scattering, the symmetry of the crystal and the scattering configuration determine selection rules, allowing only particular phonon modes to be excited. The space group of graphite is D_{6h}^4 ($P6_3/mmc$ in international notation) [120]; its isogonal point group is D_{6h} , where the c -axis is the principal rotational axis. The K and M point of the Brillouin zone belong to the subgroups D_{3h} and D_{2h} , respectively. Any other point along the high-symmetry lines is invariant under the symmetry operations of C_{2v} , where the twofold rotational axis is within the plane, coinciding with the \mathbf{q} -vector. For a general description of point groups and their notation, see textbooks on group theory, for example Refs. [67, 76]. The character tables of the D_{6h} , D_{3h} , D_{2h} , and C_{2v} point groups and their correlation tables are compiled in appendix A of Ref. [31].

At the Γ point of graphite, the longitudinal optical (LO) and the in-plane transverse (TO) phonon are degenerate and possess E_{2g} symmetry. The degeneracy is split when going inside the Brillouin zone, and the E_{2g} representation transforms into $A_1 \oplus B_1$ in C_{2v} . Along Γ - M , the LO phonon is fully symmetric (A_1), and the TO has B_1 symmetry, as can be derived from the phonon eigenvectors. *Vice versa*, the TO mode belongs to the A_1 and the LO mode to the B_1 representation in the Γ - K direction. The longitudinal acoustic (LA) mode transforms according to A_1 in both directions. The out-of-plane modes belong to the A_2 and B_2 representations. The symmetry at the K and M point can be found from the correlation of the groups as well. At the K point, the TO-derived branch is fully symmetric in the K -point group D_{3h} (A_1'), see Fig. 4.6; the LO and LA phonons form the degenerate E' mode.

The selection rules [121, 122] for inelastic X-ray scattering are determined by the symmetry of the phonon wave vector \mathbf{q} and the strict point group of the scattering wave vector \mathbf{Q} , where “strict” means that only those symmetry operations are included that transform \mathbf{Q} into itself. Symmetry operations transforming \mathbf{Q} into another wave vector \mathbf{Q}' which differs by a reciprocal

Figure 4.6: Fully symmetric (A'_1) eigenvector of the TO-derived branch at the K point of graphene.

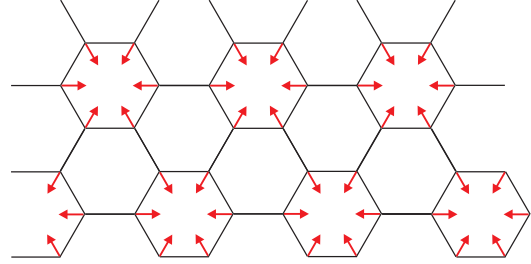


Table 4.1: Selection rules for inelastic X-ray scattering in graphite. The scattering configurations used in the experiment are listed; the scattering plane was within the plane of the graphene layers in the entire experiment. The symmetry is given by the molecular notation and by the Koster notation with respect to the point groups of the \mathbf{q} vectors, D_{2h} (M point), D_{3h} (K point), and C_{2v} (between Γ , K , and M).

\mathbf{q}	\mathbf{q}^*	\mathbf{H}	\mathbf{Q}	allowed symmetry
M point	$(-0.5 \ 0 \ 0)$	(100)	$(1.5 \ 0 \ 0)$	A_g, B_{3u} M_1^+, M_4^-
	$(1 \ -0.5 \ 0)$	$(2\bar{1}0)$	$(1 \ -0.5 \ 0)$	A_g, B_{2u} M_1^+, M_3^-
	$(-1 \ 0.5 \ 0)$	(100)	$(2 \ -0.5 \ 0)$	$A_g, B_{1g}, B_{2u}, B_{3u}$ $M_1^+, M_2^+, M_3^-, M_4^-$
K point	$(-2/3 \ 1/3 \ 0)$	(100)	$(5/3 \ -1/3 \ 0)$	A'_1, A'_2, E' K_1, K_2, K_5
	$(-1/3 \ 2/3 \ 0)$	(100)	$(4/3 \ -2/3 \ 0)$	A'_1, A'_2, E'
	$(2/3 \ -1/3 \ 0)$	$(2\bar{1}0)$	$(4/3 \ -2/3 \ 0)$	A'_1, A'_2, E'
$\mathbf{q} \in [\Gamma-M]$		(100)	$\mathbf{Q} \parallel \mathbf{q}$	A_1 Σ_1
$\mathbf{q} \in [\Gamma-M]$		(100)	$\mathbf{Q} \text{ not } \parallel \mathbf{q}$	A_1, B_1 Σ_1, Σ_3
$\mathbf{q} \in [\Gamma-K]$		$(2\bar{1}0)$	$\mathbf{Q} \parallel \mathbf{q}$	A_1 T_1
$\mathbf{q} \in [\Gamma-K]$		$(2\bar{1}0)$	$\mathbf{Q} \text{ not } \parallel \mathbf{q}$	A_1, B_1 T_1, T_3

*Note that \mathbf{q} is defined with a reversed sign in the Tables by Perez-Mato *et al.* [122]: $\mathbf{Q} = \mathbf{H} - \mathbf{q}$.

lattice vector from \mathbf{Q} , do not belong to the strict point group [122]. If the phonon eigenvector is not uniquely determined by symmetry, the additional rule applies that only those phonons are observed which possess a polarization component parallel to the scattering vector \mathbf{Q} , see Eq. (4.5).

The selection rules for the relevant scattering geometries, as found by Perez-Mato *et al.* [122, 123], are summarized in Table 4.1. If $\mathbf{Q} \parallel \mathbf{H}$, and hence $\mathbf{q} \parallel \mathbf{H}$, the fully symmetric modes are always allowed. For example, the fully symmetric LO phonon along $\Gamma-M$ is allowed if \mathbf{Q} is along $\Gamma-M$ as well [$\mathbf{H} = (100)$]. In contrast, the LO phonon has B_1 symmetry in the $\Gamma-K$ direction and is therefore forbidden in parallel configuration [$\mathbf{H} = (2\bar{1}0)$], see Fig. 4.7 (a). The TO mode, although it possesses the allowed A_1 symmetry, has a weak signal close to the Γ point because its polarization is perpendicular to \mathbf{Q} . At increasing wave vector, on the other

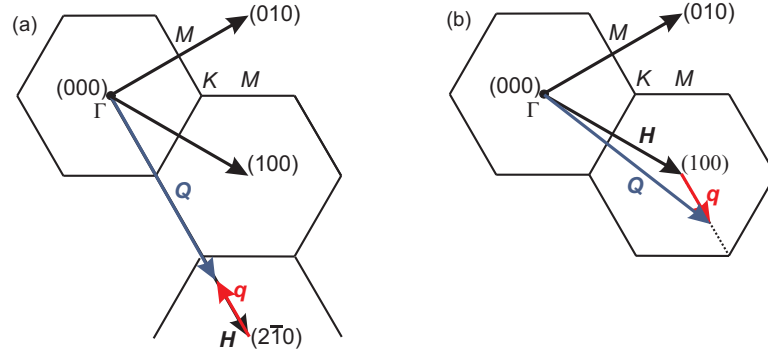


Figure 4.7: Two different scattering configurations for phonon wave vectors along Γ - K . (a) The scattering wave vector is parallel to q ; only A_1 modes are allowed by symmetry. (b) The reciprocal lattice vector H is chosen along Γ - M , i.e., q and Q are not parallel. Thus A_1 and B_1 modes are allowed.

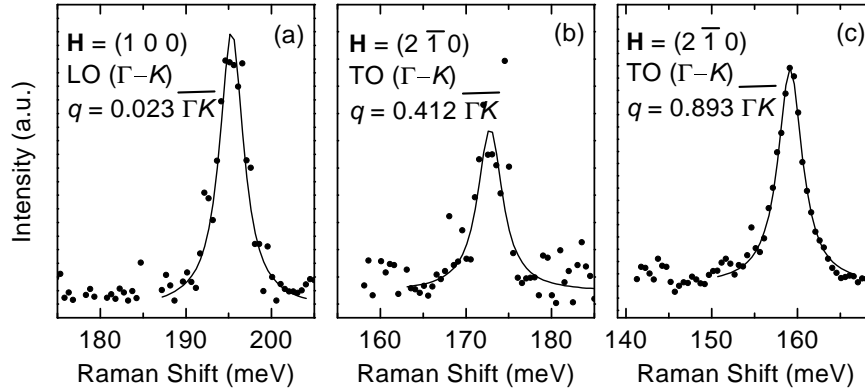


Figure 4.8: Inelastic X-ray spectra of the LO and TO branches along Γ - K . (a) Scattering configuration as in Fig. 4.7 (b), where the LO phonon is allowed. (b) and (c) Q and q are parallel, and only the A_1 -symmetry TO mode is allowed. The TO can be detected, because it is of mixed longitudinal and transverse character at large q .

hand, it loses its purely transverse character and can be detected, see Fig. 4.8 (b) and (c). Choosing $H = (100)$, where Q is not parallel to q , we could detect the LO branch in the Γ - K direction as well, see Fig. 4.7 (b) and Fig. 4.8 (a). The selection rules and the symmetry of the phonon modes help to find a correct assignment of the experimental data to the particular phonon branches, as we show below.

The experimental results of the graphite phonon dispersion are shown in Fig. 4.9 by filled dots. The irreducible representations indicating the symmetry of the phonon modes are given in the molecular notation and in the Koster notation [67, 89]. For convenience, we list the experimental phonon frequencies in Table 4.2.

Close to the Γ point, the measured frequencies agree well with the values found from Raman scattering on single crystals of graphite ($1575\ \text{cm}^{-1}$ [125]) and highly-oriented pyrolytic

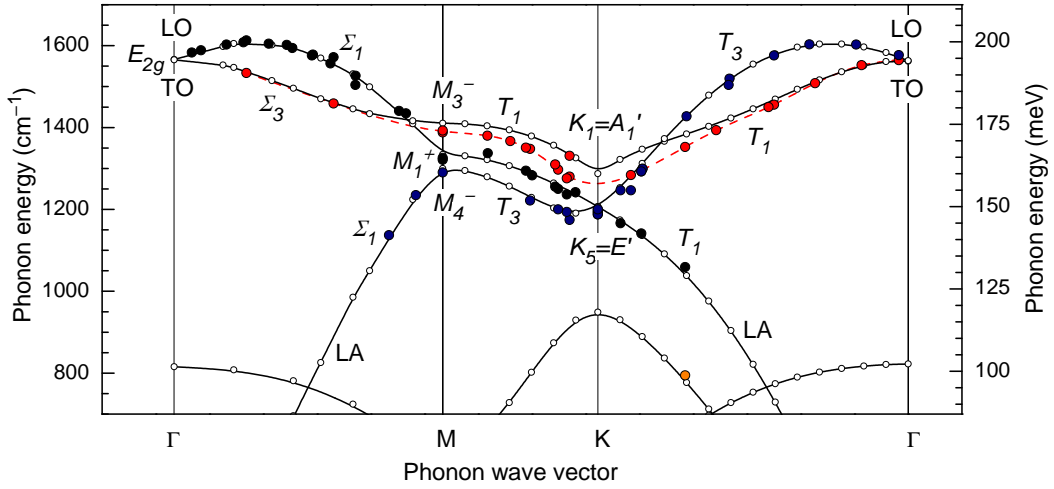


Figure 4.9: Phonon dispersion of graphite. Filled dots are experimental values; the experimental error is smaller than the size of the symbols. Open dots indicate *ab-initio* calculations of graphene that were overall scaled by 1% to smaller frequencies [124]. The phonon modes are labeled by their symmetry; between the K and M point the two upper branches belong to the T_1 representation. The dashed line is a cubic spline fit to the experimental TO branch.

graphite (1582 cm^{-1}). Starting from the Γ point, the LO branch first bends upwards (so-called overbending) in both directions, Γ - K and Γ - M . Its maximum is at $q \approx 0.15k_1$, where the length of the reciprocal lattice vectors is $|k_1| = |k_2| = \frac{4\pi}{\sqrt{3}a_0}$, and has a frequency $\approx 30 \text{ cm}^{-1}$ above the Γ -point frequency. Then the LO branch decreases rapidly, crossing in both directions the TO bands. At the K point, the LO (B_1) and the LA (A_1) form the $A_1 \oplus B_1 = E'$ mode at 1194 cm^{-1} , as predicted by symmetry. At the M point, the LO and LA phonons are close in frequency as well (1323 cm^{-1} and 1290 cm^{-1} , respectively). They cannot cross before the M point, because they have the same symmetry.

The spectra of the M -point phonons are shown in Fig. 4.10 (a) in different scattering configurations. The largest phonon energy ($172 \text{ meV} \equiv 1388 \text{ cm}^{-1}$, dashed line) was recorded with $\mathbf{Q} \parallel \mathbf{q} \parallel (2\bar{1}0)$, *i.e.*, with the scattering wave vector along Γ - K - M . The allowed phonon symmetries are A_g and B_{2u} . Because of the polarization rule, only the transverse polarization component of a phonon propagating along Γ - M gives rise to a large signal. Therefore, the peak at the highest frequency in Fig. 4.10 (a) is due to the TO-derived phonon mode. It has B_{2u} symmetry, because the A_g representation is compatible only with the symmetry of the longitudinal phonons, A_1 . The spectra shown by the thin solid lines were measured again in parallel configuration, but now the scattering wave vector $\mathbf{Q} \parallel \mathbf{q}$ was along the Γ - M direction. Therefore, the longitudinal polarization is preferred. The allowed modes are A_g and B_{3u} . Since the LA and LO branches cannot cross before the M point, the upper peak at 164 meV (1323 cm^{-1}) comes from the LO branch and has A_g symmetry. The small shoulder at 160 meV (1290 cm^{-1}) is very

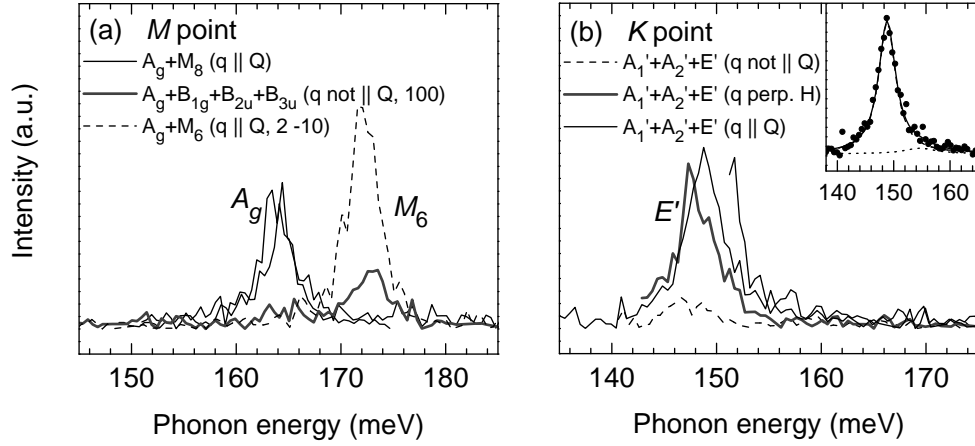


Figure 4.10: (a) Inelastic X-ray spectra from phonons at the M point in several scattering geometries. (b) Inelastic X-ray spectra from phonons at the K point. In all of the chosen scattering configurations both modes, A'_1 and E' are allowed. The signal comes mainly from the E' mode. The inset shows a fit to one of the spectra by two Lorentzians. The second peak (dotted line) at 155 ± 5 meV, however, is very weak and not well defined.

weak; we attributed it to the LA phonon at the M point (B_{3u} symmetry). In the spectrum given by the gray line, the chosen phonon wave vector is not parallel to the scattering wave vector. Since \mathbf{Q} is not along any high-symmetry line, the allowed phonon symmetries are now A_g , B_{1g} , B_{2u} , and B_{3u} . The strongest peak is again from the TO (B_{2u}) phonon, because \mathbf{Q} – and hence the preferred polarization direction – is almost perpendicular to the Γ - M direction.

At the K point, the TO-derived phonon is the highest mode as well, yet the TO branch has a pronounced minimum and is very close in frequency to the E' mode from the LO and LA branch, see Fig. 4.9. We show in Fig. 4.10 (b) the spectra of the K -point phonons. In all three scattering configurations, the phonon symmetries A'_1 , A'_2 , and E' are allowed. We attributed the peak at 148 meV (1194 cm^{-1}) to the E' phonon, which is expected to give the strongest signal [122, 123]. A fit by two Lorentzians of the spectra is shown in the inset to Fig. 4.10 (b). The second peak at 155 ± 5 meV is very broad and not well defined but might be the TO (A'_1) mode. When scanning the energy up to 190 meV, no signal could be detected above the one shown in Fig. 4.10 (b). Therefore, we performed a cubic-spline extrapolation of the measured TO branch, indicated by the dashed line in Fig. 4.9, and found $1265 \pm 10 \text{ cm}^{-1}$ for the A'_1 mode at the K point.

The shape of the TO branch with its large negative slope towards the K point and the small frequency difference to the E' mode at the K point (only 70 cm^{-1}) are in sharp contrast to the majority of theoretical predictions. Although directly at the K point the signal from the TO phonon was too weak and probably overlapped with the peaks from the LO/LA modes, the TO data near the K point are below 1300 cm^{-1} as well. In contrast, most of the calculations

Table 4.2: Experimental data of the in-plane optical phonon frequencies measured by inelastic X-ray scattering, see Fig. 4.9. The terms LO, LA, and TO refer to the properties of the phonons close to the Γ point along Γ - K - M , *i.e.*, the data follow the phonon branches in Fig. 4.9 from right to left. The \mathbf{q} vectors were projected onto the closest high-symmetry line (see Fig. 4.5); their magnitude is given in units of reciprocal lattice vectors. The M point in the Γ - K - M direction is at $0.5\sqrt{3}$, and the K point is at $2/3$ of this line; the distance Γ - M is 0.5.

	LO		LA		TO		
Γ - K	0.017	1577			0.017	1565	
	0.097	1602			0.087	1552	
	0.184	1603			0.173	1508	
	0.250	1576			0.250	1456	
	0.333	1519			0.260	1450	
	0.334	1504			0.357	1394	
	0.412	1427	0.415	1059	0.415	1352	
	0.494	1299			0.494	1299	
	0.497	1293	0.497	1141	0.497	1293	
	0.516	1247			0.516	1247	
K	0.535	1247	0.535	1166			
	0.577	1194	0.577	1194			
K - M			0.619	1242	0.630	1280	
	0.630	1174			0.630	1330	
	0.635	1194	0.635	1236	0.635	1276	
	0.651	1200	0.651	1250	0.651	1297	
	0.704	1222	0.700	1283	0.704	1348	
			0.711	1294	0.711	1351	
					0.740	1367	
			0.782	1337	0.783	1380	
	M	0.866	1290	0.866	1323	0.866	1323
	M - Γ	0.916	1235	0.934	1435		
0.966		1137	0.947	1440			
			1.028	1527			
			1.029	1504			
			1.069	1572	1.069	1459	
			1.075	1556			
			1.107	1578			
			1.109	1576			
			1.146	1594			
			1.156	1602			
		1.190	1605				
		1.231	1613	1.231	1533		
		1.237	1608				
		1.268	1602				
		1.316	1589				
		1.333	1583				

Table 4.3: Optical-phonon frequencies (in cm^{-1}) of graphite at the high-symmetry points Γ , K , and M predicted from theory. (The values from the GGA calculation [124] were not scaled as in Fig. 4.9.) The bottom line displays the frequencies found by inelastic X-ray scattering (IXS), see Fig. 4.9.

method	Γ	K		M		
force-constants [114]	1595	1365	1270	1545	1365	1200
<i>ab-initio</i> , LDA [115]	1700	1535	1270	1600	1470	1285
<i>ab-initio</i> , LDA [117]	1600	1370	1240	1440	1385	1340
molecules, <i>ab-initio</i> [116]	1540	1235	1215	1380	1355	1340
Raman scattering [127]	1595	1450	1275	1620	1340	1120
<i>ab-initio</i> , DFPT [126]	1580	1340	1220	1400	1340	1320
<i>ab-initio</i> , GGA, Fig. 4.9 [124]	1581	1300	1220	1425	1350	1315
experiment IXS, Fig. 4.9 [124]		1265	1194	1390	1323	1290

published so far predicted the A'_1 mode well above 1300 cm^{-1} , see Table 4.3. Calculations from empirically determined force-constants showed even a local maximum of the TO branch at the K point [114]. Although the first-principles calculations agree with the experimental data regarding the existence of the minimum, the splitting between the A'_1 and E' modes in these calculations ranges from 120 cm^{-1} to 265 cm^{-1} [115, 117, 126] and is thus significantly larger than the experimentally obtained splitting of 70 cm^{-1} . Except for the K point, the best agreement with the experimental data of Fig. 4.9 was found in the *ab-initio* calculation within density-functional perturbation theory by Pavone *et al.* [126]. Mapelli *et al.* [116] calculated the graphite dispersion from a valence force field obtained by *ab-initio* calculations of small aromatic molecules. This molecular approach leads to an overall softening of the phonon frequencies, for example, the Γ -point frequency is at 1540 cm^{-1} . In spite of this general underestimation of the frequencies, the K -point frequency of the TO branch is very close to the measured value, and the splitting between the A'_1 and the E' mode is only 20 cm^{-1} in this calculation.

In Fig. 4.9 we show by open dots (connected by solid lines) an *ab-initio* calculation of graphene, performed by S. Reich [124]. The calculation was done within density-functional theory in the generalized gradient approximation [128] (GGA) using the SIESTA code [129]. Because of the weak interaction between the graphite layers, the high-energy phonons of graphite have approximately the same frequencies as in graphene and are twofold degenerate. The agreement of the calculation with the experimental data is excellent. In particular, the overbending in the longitudinal branches, the slopes and the frequencies at the high-symmetry points match the experimental values very well. The calculated TO branch is around the K

point still above the experiment, but much closer than previous *ab-initio* calculations [117]. The calculated splitting between the A'_1 and the E' modes at the K point is only 80 cm^{-1} , in good agreement with the experimental value of $\approx 70 \text{ cm}^{-1}$.

The slight overall softening of the calculated frequencies compared to previous *ab-initio*-LDA calculations is due to the second-order generalized-gradient approximation, which typically gives rise to slightly larger lattice constants [130]. More important, however, is the strong softening of the A'_1 mode at the K point, which is not a result of using GGA in the calculation. Because the forces are long-ranged in a semimetal like graphite, the phonon frequencies can be obtained only at those wave vectors that are commensurate with the supercell used in the calculation. Therefore, the softening of the K -point phonon is observed only if the K point is explicitly included [124]. The large frequency drop of the A'_1 mode indicates a strong coupling of this phonon to the electronic system. Indeed, the fully symmetric K -point phonons couple the electrons at the Fermi wave vectors from two inequivalent K points. This coupling is experimentally supported by transport measurements [131, 132] and double-resonant Raman scattering of the D mode [133, 134]. In Chap. 5 we will use the experimental phonon dispersion to explicitly calculate the Raman D mode in graphite.

4.3 Phonon dispersion of carbon nanotubes

In carbon nanotubes, the phonon dispersion cannot be measured at present, because one would need single crystals of single-walled nanotubes of the same chirality. Only Γ -point phonons are probed by conventional Raman scattering. In the Chap. 5 we will show that by defect-induced, double-resonant Raman scattering parts of the phonon dispersion can be measured. For complete phonon dispersion relations of nanotubes we have to rely on theoretical predictions for the moment. Although simple zone-folding from graphite yields some systematic errors for the acoustic branches, we can relate the nanotube phonon modes to the ones in graphite to some extent. In general, the tangential modes will be less affected than the radial modes by rolling the graphite sheet into a cylinder.

In this section we first summarize the general properties of phonons in carbon nanotubes that are derived from their structure and symmetry and hence do not depend on a specific model (Sect. 4.3.1). Then we present symmetry-based force-constants calculations that were obtained in collaboration with the group of M. Damnjanović (Belgrade University) in Sect. 4.3.2 [135]. Finally, we investigate the special case of double-walled carbon nanotubes, where the phonon frequencies are additionally affected by the interaction between the two nanotube walls (Sect. 4.3.3).

4.3.1 Phonon symmetries in carbon nanotubes

The nanotube unit cell contains $2q$ atoms, where q is the number of graphene hexagons in the unit cell (Sect. 2.1), thus the tube possesses $3 \times 2q$ phonon modes. In the zone-folding picture, they correspond to the six phonon bands of graphene, where from each graphene band in the two-dimensional Brillouin zone q lines with $m \in (-q/2, q/2]$ are taken, see Chap. 2. In achiral tubes, the modes with index m and $-m$ are degenerate for the same k , thus $6 \times (n+1)$ phonon branches are actually seen in a plot of the phonon dispersion. In chiral tubes, a phonon given by $|km\rangle$ is only degenerate with $| -k - m \rangle$, see Sect. 2.2. Therefore, all $6q$ phonon branches are plotted in linear quantum numbers. They can be “unfolded” into $6n$ bands by using the helical quantum numbers, where n is the order of the pure rotational axis.

Damjanović *et al.* [46] derived the dynamical representations in the nanotube line groups and their decomposition into irreducible representations. Each of these irreducible representations corresponds to a specific phonon mode. In zig-zag (\mathcal{Z}) and armchair (\mathcal{A}) tubes the decomposition for the Γ -point modes reads (in molecular notation)

$$D_{\mathcal{Z}}^{\text{dyn}} = 2(A_{1g} + A_{2u} + B_{1g} + B_{2u}) + A_{2g} + A_{1u} + B_{2g} + B_{1u} + 3 \sum_m (E_{mg} + E_{mu}) \quad (4.6)$$

$$D_{\mathcal{A}}^{\text{dyn}} = 2(A_{1g} + A_{2g} + B_{1g} + B_{2g}) + A_{2u} + A_{1u} + B_{2u} + B_{1u} + \sum_{\text{modd}} (4E_{mu} + 2E_{mg}) \\ + \sum_{\text{meven}} (4E_{mg} + 2E_{mu}) \quad \text{for } n \text{ even} \quad (4.7)$$

$$D_{\mathcal{A}}^{\text{dyn}} = 2(A_{1g} + A_{2g} + B_{1u} + B_{2u}) + A_{2u} + A_{1u} + B_{2g} + B_{1g} + \sum_{\text{modd}} (4E_{mu} + 2E_{mg}) \\ + \sum_{\text{meven}} (4E_{mg} + 2E_{mu}) \quad \text{for } n \text{ odd,}$$

where the sum is over the integer values $m = 1, \dots, (n-1)$. In chiral (\mathcal{C}) tubes, the dynamical representation is decomposed into

$$D_{\mathcal{C}}^{\text{dyn}} = 3(A_1 + A_2 + B_1 + B_2) + 6 \sum_m E_m, \quad (4.8)$$

where m takes integer values from $(-n/2, n/2]$.

In contrast to three-dimensional crystals, the nanotube (like any one-dimensional crystal) possesses four acoustic modes instead of three. These are the translations into three directions and the rotation about the tube axis. The rotational mode, which becomes a twisting vibration at finite wave vector, results from the translation of graphene along the chiral vector. The symmetry of the acoustic modes is $A_{2(u)}$ for the z -translation, $E_{1(u)}$ for the xy -translation and $A_{2(g)}$ for the rotational mode. The subscripts u and g apply to achiral tubes only.

The irreducible representations which transform like a polar vector determine the infrared-active phonons. In the nanotube line groups, the z -component of the polar vector corresponds to the non-degenerate $A_{2(u)}$ representation; the x - and y - components transform like $E_{1(u)}$. Therefore, the infrared-active modes (after subtracting the acoustic modes) are [136]

$$\begin{aligned}
 \text{infrared active: } & A_{2u} + 2E_{1u} && (\text{zig-zag}) \\
 & 3E_{1u} && (\text{armchair}) \\
 & A_2 + 5E_1 && (\text{chiral tubes}). \tag{4.9}
 \end{aligned}$$

From the symmetric part of the direct product of two polar-vector representations, $[(A_{2u} \oplus E_{1u}) \otimes (A_{2u} \oplus E_{1u})]$, the symmetry of the Raman-active phonons is derived to be $A_{1g} + E_{1g} + E_{2g}$ in achiral tubes and $A_1 + E_1 + E_2$ in chiral tubes [30]. The Raman active modes in carbon nanotubes are then

$$\begin{aligned}
 \text{Raman active: } & 2A_{1g} + 3E_{1g} + 3E_{2g} \quad \text{or} \quad 2_0A_0^+ + 3_0E_1^- + 3_0E_2^+ \quad (\text{zig-zag}) \\
 & 2A_{1g} + 2E_{1g} + 4E_{2g} \quad \text{or} \quad 2_0A_0^+ + 2_0E_1^- + 4_0E_2^+ \quad (\text{armchair}) \\
 & 3A_1 + 5E_1 + 6E_2 \quad \text{or} \quad 3_0A_0^+ + 5_0E_1 + 6_0E_2 \quad (\text{chiral tubes}). \tag{4.10}
 \end{aligned}$$

In a Raman process, the polarization of incoming and scattered (detected) light determine which of the Raman active phonons are observed. For example, if both incoming and outgoing light have parallel polarization to the tube axis ($A_{2u} \equiv_0 A_0^-$), the net change of the m quantum number is zero. Therefore, only the fully symmetric phonons contribute to the Raman signal in (z, z) geometry. The $E_{1(g)}$ phonon can be observed, if the m quantum number changes by ± 1 in total, *i.e.*, one of the photons must be z -polarized ($\Delta m = 0$) and the other one x/y -polarized ($\Delta m = \pm 1$). Finally, if the polarization of both incoming and outgoing light is perpendicular to the tube axis, $A_{1(g)}$ and $E_{2(g)}$ phonons are allowed.

In Fig. 4.11 we show the phonon eigenvectors corresponding to the A_{1g} modes in armchair and zig-zag tubes. The radial breathing mode (RBM), where all carbon atoms move in-phase in the radial direction is fully symmetric ($A_{1g} =_0 A_0^+$) for any chirality of tubes [Fig. 4.11 (a)]. Its frequency is comparatively low ($150 - 300 \text{ cm}^{-1}$ for typical tube diameters between 0.7 and 1.5 nm), because the restoring forces, *i.e.*, the carbon-carbon bonds, are almost perpendicular to the displacement direction. The RBM frequency decreases with increasing tube diameter and becomes zero in the limit of infinite diameter, which corresponds to the out-of-plane acoustic mode of graphite.

The tangential $A_{1(g,u)}$ modes, in contrast, have frequencies up to 1600 cm^{-1} . They are shown in Fig. 4.11 (b) and (c). In armchair tubes, the circumferential optical mode is fully symmetric, as is in zig-zag tubes the axial mode. Since the horizontal mirror planes in armchair

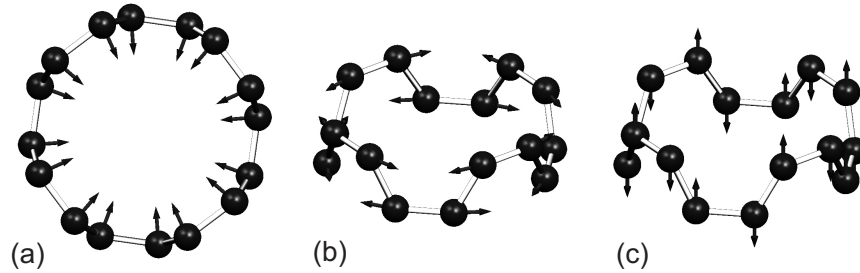


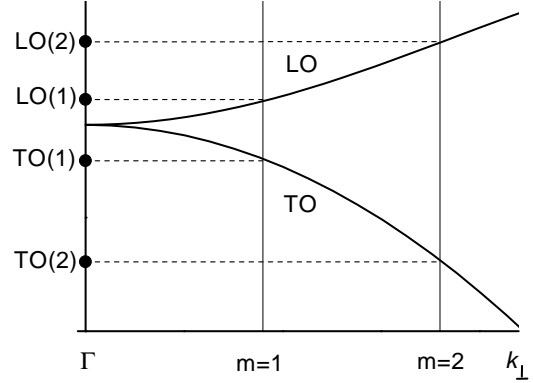
Figure 4.11: Unit cell and phonon eigenvectors of the (4,4) armchair tube. (a) Radial breathing mode (fully symmetric and Raman active, ${}_{0}A_{0}^{+}$); (b) circumferential (TO) mode (${}_{0}A_{0}^{+}$); (c) axial (LO) mode (not Raman active, ${}_{0}B_{0}^{-}$).

tubes contain the carbon atoms, the A_{1g} displacement is restricted to be within the plane. For the same reason, the fully symmetric modes in zig-zag tubes must vibrate within the vertical planes. In chiral tubes, the mirror planes do not constitute symmetry operations, and the displacement of the A_1 modes is not restricted to any direction. In particular, the longitudinal and transverse optical modes mix in chiral tubes [137].

Similarly, the radial breathing mode is not restricted by symmetry to the purely radial direction; it can in principle mix with the high-energy A_{1g} modes. Although this mixing is likely to be small because of the large differences in the force constants for radial and tangential displacement, it has been found in several calculations as a small non-radial component of the RBM [136, 138, 139].

The zone-folding approach – although it does not predict the correct frequencies – relates the high-energy modes of carbon nanotubes to those of graphene. Here, we explain this idea in some detail, because contradictory notations for the high-energy vibrations are used in the literature based on zone folding. Some properties of the high-energy phonon dispersion in nanotubes can still be understood within this simple picture. The nanotube modes that correspond directly to the Γ -point E_{2g} mode of graphene are the modes with $m = 0$ and $k = 0$, which have A_1 symmetry (A_{1g} and A_{1u} in achiral tubes). Because the wave vector is confined along the circumference of the tube (Sect. 2.1), non- Γ -point phonons of graphene transform into Γ -point modes of carbon nanotubes. These are the phonons with wave vector $k_z = 0$ and $m = 1, 2, \dots, n$. Within the zone-folding approach, A_1 modes always have the same frequency as the Γ -point mode in graphene. The $E_{1(g)}$ and $E_{2(g)}$ modes of the tube correspond in the zone-folding picture to the graphene phonons at $k_{\perp} = 2/d$ ($m = 1, 2$ nodes along the circumference) and $k_{\perp} = 4/d$ ($m = 2, 4$ nodes), respectively. Because the LO phonon in graphene exhibits an overbending in all directions of the Brillouin zone, one of the $E_{1(g)}$ and $E_{2(g)}$ modes each have in nanotubes a higher frequency at the Γ point than the fully symmetric $m = 0$ modes.

Figure 4.12: Zone-folding scheme for the high-energy modes. The graphene LO and TO branches are shown in the direction of the quantized wave vector k_{\perp} of the nanotube. For $m = 1$ and $m = 2$, the slices at $k_{\perp} = 2/d$ and $k_{\perp} = 4/d$ (vertical lines) are cut along the direction k_z , which is perpendicular to the plane of the paper. The dots indicate the derived frequencies at the Γ point of the nanotube ($k_z = 0$). The notation on the left is the one used here, where LO- and TO-derived refers to the graphene phonon branches. The graphene LO phonon propagating along k_{\perp} has (by definition) a displacement parallel to k_{\perp} , *i.e.*, in the circumferential direction, and, *vice versa*, the TO phonon has a displacement perpendicular to k_{\perp} , *i.e.*, along the nanotube axis. For small m the LO-derived dispersion in nanotubes resembles the graphene LO dispersion.



In Fig. 4.12 we show schematically part of the longitudinal (LO) and transverse (TO) phonon dispersion of graphene along the direction of the quantized wave vector k_{\perp} of the nanotube. The graphene LO phonon in this direction has (near the Γ point) a displacement parallel to k_{\perp} . When cutting “slices” of the graphene dispersion along k_z (perpendicular to k_{\perp}) and with $k_{\perp} = 2m/d$, we label all bands obtained from the graphene LO branch as LO-derived and those obtained from the TO branch as TO-derived. For $m = 0$, *i.e.*, at $k_{\perp} = 0$, the LO-derived phonon is indeed a longitudinal vibration with both the propagation direction (k_z) and the displacement along the tube axis.¹ For small k_{\perp} ($m = 1$ or $m = 2$), the LO- and TO-derived bands are still similar in shape to the LO and TO dispersion in graphene, respectively. On the other hand, the LO- or TO-derived modes for $m > 0$ cannot unambiguously be named as longitudinal or transverse. As an example, we take the nanotube modes with $m = 1$ and $k_z = 0$. These are in Fig. 4.12 the frequencies where the first vertical line cuts the LO and the TO dispersion. The LO-derived mode has the higher frequency and the TO-derived mode the lower frequency. Since the LO-derived phonon has an atomic displacement parallel to k_{\perp} , it is a circumferential mode, whereas the TO-derived one is an axial mode. A different notation is often used, where axial modes are always named LO, as their displacement is along the propagation direction k_z (neglecting k_{\perp}), and all circumferential modes are called TO. In this alternative notation the LO-derived phonons with $m > 0$ are named TO and *vice versa*. For $m = 0$ both notations are the same. Here we will either name the phonons by their axial or circumferential displacement or stay with the notation first introduced as LO- and TO-derived, where LO and TO merely refers to the resemblance of the graphene LO and TO dispersion but not to the displacement direction.

¹We neglect for the moment the deviation from the purely longitudinal or transverse character of the modes in chiral tubes, see Ref. [137].

The acoustic phonon modes in carbon nanotubes cannot be directly obtained from zone folding, except for the translation along the tube axis, which corresponds to a translation of the graphite sheet. The in-plane translation of graphene perpendicular to the direction of the nanotube axis transforms into the rotational mode. The out-of-plane translation of graphite becomes the radial breathing mode, which has finite frequency at the Γ point and is hence not an acoustic mode. *Vice versa*, the two remaining acoustic modes in nanotubes, *i.e.*, the x, y - translations perpendicular to the tube axis, have non-zero frequency if the nanotube is unwrapped into the flat graphite sheet.

4.3.2 Force-constants calculations

In this section we present calculations of the phonon dispersion in carbon nanotubes that relied on the earlier determined force-constants of graphite, which, as we know by now, are for some parts of the optical-phonon dispersion not correct [124]. The work on revised empirical force constants based on the experimental data of graphite is in progress. Nevertheless, some general or qualitative properties are still valid and will be discussed here.

In Fig. 4.13 we show the non-degenerate phonon branches of achiral nanotubes. The calculations are based on the nanotube symmetry, *i.e.*, the eigenvalue problem is reduced to the low-dimensional interior space of a single carbon atom, from which the entire nanotube can be constructed by applying all symmetry operations of the tube [136]. Modified force constants of graphite were used [114, 135], where the change of the atom positions in the curved graphite sheet with respect to the flat graphene plane was incorporated by explicitly including the change in bond angle on the curved graphene wall. Additionally, the energy of the rotation about the tube axis (fourth acoustic mode) was required to vanish. Up to fourth-nearest neighbor interaction was included in order to reproduce the experimentally observed overbending in the optical phonon bands. The phonon branches are labeled by their symmetry and by the direction of the atomic displacement at the Γ point. In most cases, the displacement direction changes along a given phonon branch, in correlation with an anti-crossing, as can be seen for example between the RBM branch and the z -translational mode. The parity with respect to the vertical mirror plane (A/B) remains the same in the entire Brillouin zone; the horizontal mirror plane parity (subscripts $+/-$) is not defined for $q \neq 0$.

In armchair tubes, $q = 2\pi/(3a)$ for $m = n$ corresponds to the K point of graphite. The minimum at $\approx 1250 \text{ cm}^{-1}$ thus comes from the LO-derived K -point phonon in graphite; the upper $m = n$ branch stems from the TO-derived A'_1 mode at the K point. As in previous force-constants calculations for graphite [114], this mode shows in our calculation a maximum instead of the experimentally observed minimum (Sect. 4.2). Therefore, we expect significant changes in the high-energy $m = n$ branches around $q = 2\pi/(3a)$, if revised force constants are

Figure 4.13: Phonon dispersion of the (6,6) and the (12,0) tube. Only the non-degenerate branches ($m = 0$ and $m = n$) are shown; their symmetry at the Γ point is given. The letters “L”, “T”, and “R” refer to longitudinal (along the tube axis), transverse (perpendicular to the axis) and radial displacement at the Γ point.

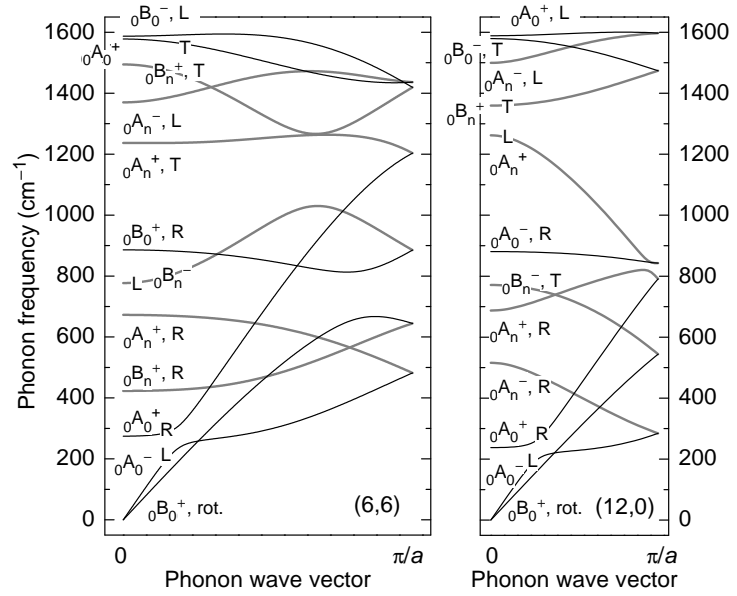
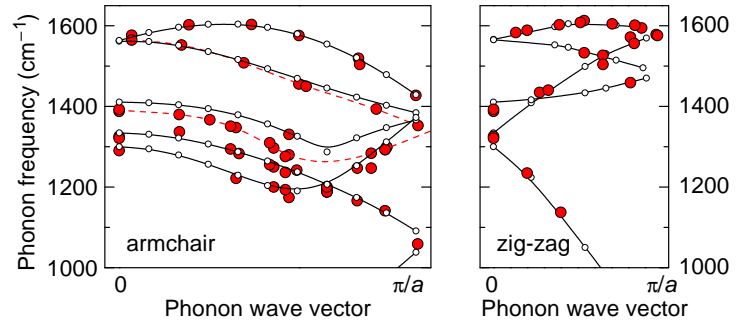


Figure 4.14: Phonon dispersion of the non-degenerate branches ($m = 0$ and $m = n$) of an armchair and an zig-zag tube obtained from zone-folding of the experimental graphite dispersion. Full dots are the experimental data; open dots indicate the *ab-initio* calculation, see Fig. 4.9.



taken into account. For comparison, we show in Fig. 4.14 the non-degenerate phonon bands obtained by zone-folding of the experimentally determined graphite dispersion. We expect the general shape of the dispersion in nanotubes to be similar to the one Fig. 4.14, in particular the softening of the TO-derived $m = n$ branch at $q = 2\pi/(3a)$. In zig-zag tubes, the LO-derived $m = n$ branch shows a much larger dispersion in the zone-folding approximation than in the calculation of Fig. 4.13, because the LO and TO-derived modes in graphite cross between the Γ and the M point.

In Fig. 4.15 we show the phonon dispersion of the (14,5) nanotube. It is a metallic tube with $\mathcal{R} = 3$ and 388 atoms in the unit cell. Therefore, it is convenient to display the phonon dispersion by helical quantum numbers with only 6 ($\tilde{m} = 0$) phonon branches. Again, the wave vector at $2/3$ of the helical Brillouin zone corresponds to the K point of graphite (indicated by the dashed vertical line). Therefore we expect that the highest phonon branch, different

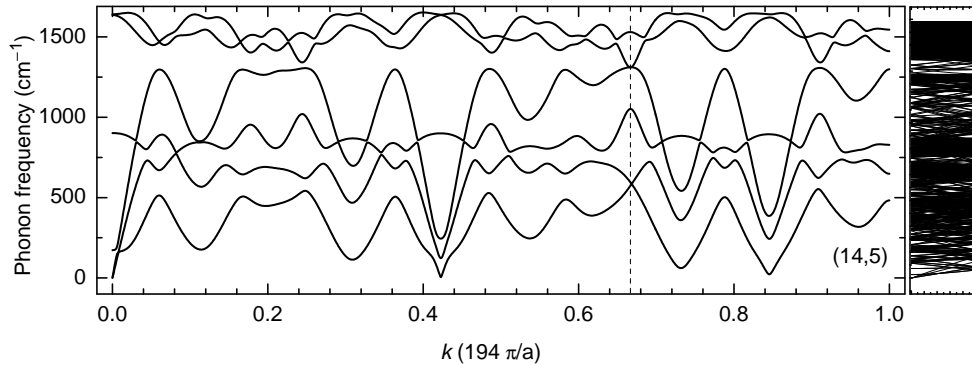


Figure 4.15: Phonon dispersion of the (14,5) tube given by helical quantum numbers. In the (14,5) tube $n = 1$, thus there are 6 phonon branches with $\tilde{m} = 0$. They correspond to the 6×194 phonon branches in the description of linear quantum numbers shown to the right. The dashed line at $2/3$ of the helical Brillouin zone indicates the K -point wave vector in the zone-folding picture. See Ref. [135].

from our calculation, has a minimum close to the second-highest optical branch at $2/3$ of the Brillouin zone.

4.3.3 Double-walled carbon nanotubes

In double-walled carbon nanotubes (DWNT) the effect of tube–tube interactions on the vibrational modes can be studied. Still they have some properties of their constituent single-walled tubes, such as the RBM signal and the double-peak high-energy modes in the Raman spectra (Chap. 5). The interaction between the inner and outer tube is often investigated with respect to the breathing-like phonon modes [140, 141]. In addition, the comparatively small diameter of the inner tube in typical DWNT samples has led to a number of Raman studies which attempted an assignment of the inner tube chirality based on the radial breathing mode frequencies [142–144]. In these investigations, the interaction between the tube walls is often modeled by adding a constant to the dependence of the RBM frequency on the inverse tube diameter. In both theoretical and experimental studies the distance between the tube walls is usually assumed the same as the interlayer distance in graphite, *i.e.*, $\approx 3.4 \text{ \AA}$.

In this section we study the vibrational properties of double-walled carbon nanotubes by *ab-initio* density-functional calculations for several pairs of armchair tubes and show that double-walled nanotubes with interwall distances different from the value in graphite may exist. In double-walled tubes with a smaller wall distance [(4,4)@(8,8)], the phonon modes exhibit a strong mixing; in all other investigated DWNTs each of the constituents vibrates independently. In the (3,3)@(8,8) tube, the change in phonon frequencies due to the wall interaction is larger for the high-energy optical phonon modes than for the RBM.

E_{tot} eV/atom	radius Å	E_{tot} eV/atom	radius (inner)	radius (outer)	interwall distance	E_{tot} gain eV/atom
(3,3) -154.8697	2.102	(3,3)@(8,8) -155.1776	2.103	5.458	3.355	0.020
(4,4) -155.0691	2.769	(4,4)@(8,8) -155.1983	2.725	5.546	2.821	-0.002
(8,8) -155.2663	5.463	(3,3)@(9,9) -155.1873	2.106	6.121	4.015	0.010
(9,9) -155.2803	6.141	(4,4)@(9,9) -155.2341	2.772	6.123	3.351	0.019

Table 4.4: Total energy per carbon atom after relaxation of the atomic positions.

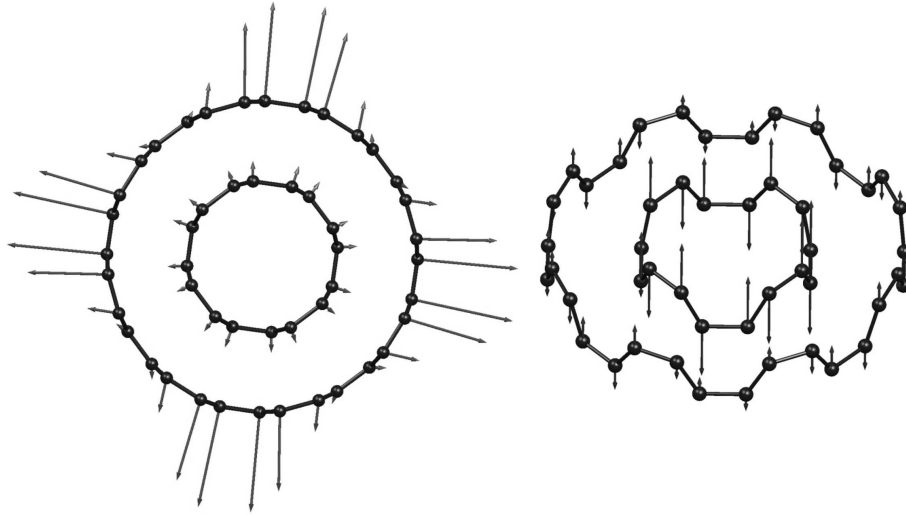


Figure 4.16: (4,4)@(8,8) tube: in-phase breathing mode at 232 cm^{-1} (left) and out-of-phase LO mode at 1582 cm^{-1} (right).

We performed *ab-initio* calculations using the SIESTA code within the local-density approximation [129]. A double- ζ , singly polarized basis set of localized atomic orbitals was used for the valence electrons. In Table 4.4 we summarize the total energy per carbon atom after the relaxation of the atomic positions in the investigated double-walled tubes. All four double-walled nanotubes, with the inter-wall distance ranging from 2.8 Å [(4,4)@(8,8)] to 4.0 Å [(3,3)@(9,9)], appear stable. The energy gain per carbon atom from the sum of the two isolated constituents to the double-walled tube is given in the last column of Table 4.4.

In the (4,4)@(8,8) and the (3,3)@(9,9) tube, the two constituents have a fourfold and threefold rotational axis in common, respectively, *i.e.*, they are commensurate with respect to rotations about the tube axis. In the other two double-walled tubes, the only symmetry operations besides the translation along the tube axis are the horizontal mirror plane and the U axis [46,63]. Thus for the incommensurate double-walled tubes a very low friction between the walls is expected if the tubes are rotated against each other, whilst there is interaction between the walls in

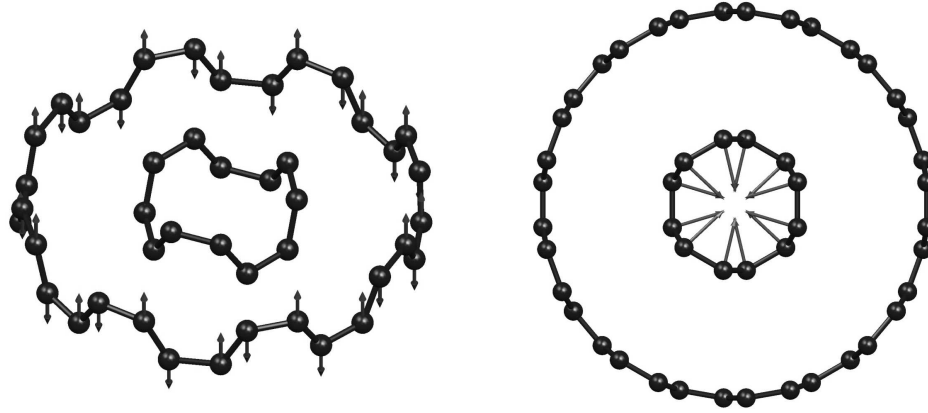


Figure 4.17: Longitudinal optical mode in the (3,3)@(8,8) tube (left) and RBM mode in the (3,3)@(9,9) tube (right). In both double-walled tubes, the inner and outer tubes vibrate independently.

the commensurate ones [145]. Since the calculation of the acoustic phonon frequencies is not accurate enough, we investigated this prediction by rotating the inner tube in the (4,4)@(8,8) and the (3,3)@(8,8) and comparing the total energy before and after the rotation. We found a change in total energy less than 1 meV/atom for the (3,3)@(8,8) when the (3,3) tube was rotated. In the (4,4)@(8,8) tube the total energy increased by several meV per carbon atom upon rotation of the (4,4) tube, in agreement with the group-theoretical prediction.

We calculated the Γ -point phonon frequencies of the DWNTs, of their isolated constituents and, for comparison, of their constituents with the same (unrelaxed) atomic positions as in the DWNTs. As expected, because of their small interwall distance and the commensurability, the RBM frequencies in the (4,4)@(8,8) tube are upshifted by 25-55 cm^{-1} with respect to the RBM in single-wall tubes. The longitudinal optical (LO) phonon mode is upshifted as well by up to 100 cm^{-1} . Moreover, the phonon displacements exhibit a strong mixing in the (4,4)@(8,8) tube. The in-phase and out-of-phase displacements of the two tubes are clearly seen (Fig. 4.16). Due to the symmetry reduction in the double-walled tube, the amplitude of the RBM vibration does not necessarily remain constant along the circumference of the tube. Instead, the in-phase RBM amplitude is modulated by $\pi/2$ along the circumference.

In the (3,3)@(8,8) tube, we found no significant change in the RBM frequencies. Surprisingly, the transversal optical (TO) phonon mode of the (8,8) tube exhibits a downshift by 30 cm^{-1} . Most of the phonon eigenvectors in this double-walled tube are independent vibrations of their constituents; either the inner or the outer tube is displaced, while the amplitude of the other tube's displacement is zero (see Fig. 4.17). Also in the (3,3)@(9,9) tube the RBM frequencies are not affected by a wall-wall interaction. This might partly be due to the large

interwall distance of 4 Å. On the other hand, from the commensurability of the tubes we would expect some interaction between the walls.

In summary, we have shown that double-walled nanotubes with interwall distances between 2.8 and 4.0 Å may exist. We found from *ab-initio* calculations that for some double-walled nanotubes the high-energy optical phonon modes are even more affected by the wall-wall interaction than the RBM modes. Since the effect on the RBM frequency of the inner tube is predicted to increase strongly with the tube diameter [140, 141, 146], *ab-initio* calculations for larger double-walled tubes are necessary.

5 Double-resonant Raman scattering in carbon nanotubes

Raman scattering is a powerful tool for the investigation of the vibrational and electronic properties of a material, in particular of the phonon frequencies and their dispersion that were discussed in the previous chapter. In carbon nanotubes the interpretation of the experimental results is not straightforward but rather complex and controversial. The concept of double-resonant Raman scattering is shown in this chapter to be the key to a consistent understanding of the Raman spectra of carbon nanotubes.

A typical Raman spectrum of single-walled carbon nanotubes is shown in Fig. 5.1. The first-order spectrum is usually divided into the low-energy and the high-energy region. The strongest low-energy Raman mode is the fully symmetric radial breathing mode (RBM, see Sect. 4.3.1), where all atoms move in phase in the radial direction. The RBM frequency is approximately proportional to the inverse tube diameter and is therefore frequently used for diameter determination [115, 136, 138, 147]. Even an assignment of the tube chiralities was attempted on the basis of the radial breathing mode, although there is considerable disagreement on the precise relationship between diameter and RBM frequency [143, 144, 148]. In the high-energy region, the phonons correspond to tangential displacements of the atoms. The Raman peaks at $\approx 1600 \text{ cm}^{-1}$ stem from the high-energy optical, fully symmetric modes close to the Γ point and are referred to as high-energy modes (HEM). They can be related to the graphite E_{2g} phonon, whose degeneracy is lifted by rolling the graphite sheet into a nanotube. To emphasize this connection to the graphite G mode, the high-energy modes are often also called G mode. The peak at $\approx 1350 \text{ cm}^{-1}$ is the so-called D mode, which is also present in graphite [125]. The D mode is induced by the presence of defects and stems from inside the Brillouin zone (with a wave vector close to $2/3$ of the Brillouin zone) [133, 149]. The strongest peak in the second-order spectrum is the overtone of the D mode at $\approx 2700 \text{ cm}^{-1}$; the overtone of the high-energy modes at $\approx 3200 \text{ cm}^{-1}$ is much weaker. The overtone of the D mode is called D^* or G' in the literature. A number of additional Raman peaks is observed in the intermediate frequency range, which are due to combination modes of optical and acoustic phonons [150].

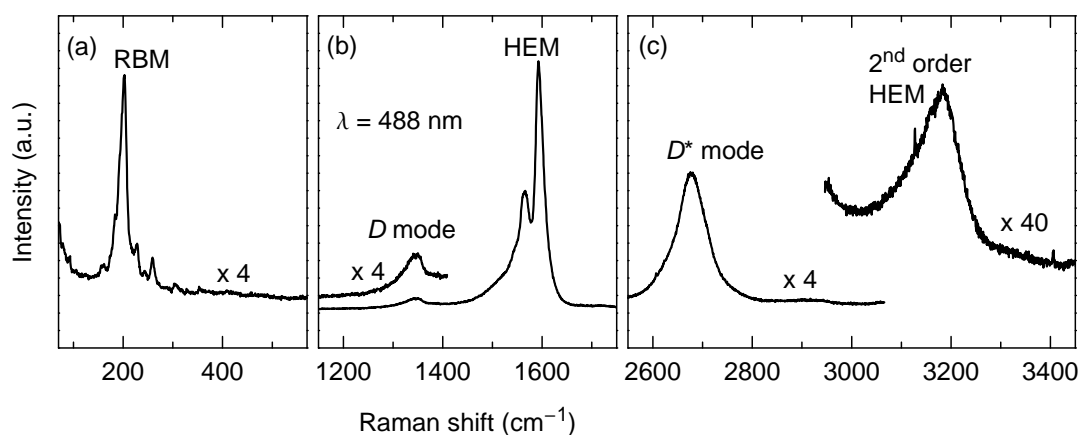
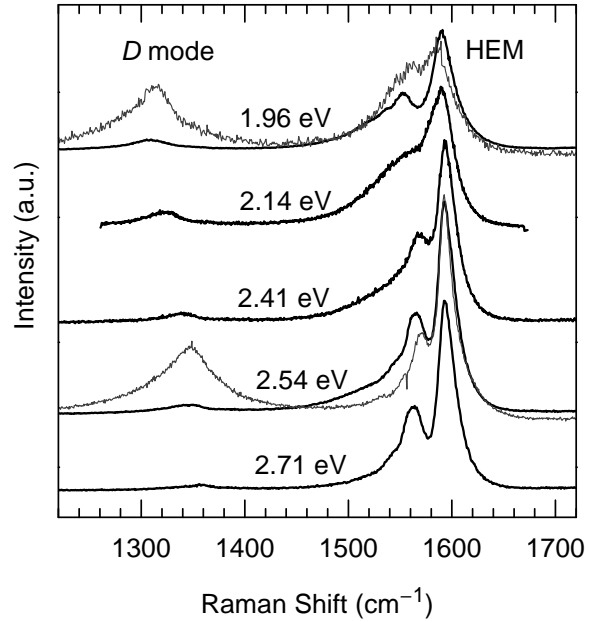


Figure 5.1: First- and second-order Raman spectrum of carbon nanotubes recorded at a laser wavelength of 488 nm (2.54 eV). (a) radial breathing modes; (b) *D* mode and high-energy modes; (c) second-order overtones of the *D* mode and the HEM. The spectra were scaled as indicated.

The Raman spectra of carbon nanotubes depend significantly on the wavelength of the exciting light. Besides the intensity of the signal, as in common resonant or nearly-resonant Raman scattering, this includes also the position and shape of the peaks. A prominent example of this unusual behavior is the *D* mode in carbon nanotubes as well as in graphite. Its frequency shifts by $\approx 50 \text{ cm}^{-1}/\text{eV}$ because of a double-resonant scattering process, where at each excitation energy a different phonon mode is selectively enhanced. In Fig. 5.2 we show the Raman spectra of carbon nanotubes recorded at different laser wavelengths. The position of the *D* mode depends strongly on the laser energy. The high-energy modes shift as well, although much less than the *D* mode. On the other hand, their line shape changes significantly with excitation energy. The spectra excited with 1.96 eV show a broad and slightly downshifted HEM structure with a large signal down to $\approx 1540 \text{ cm}^{-1}$. This appearance is usually attributed to the excitation of metallic nanotubes [151–153], see also Sect. 5.4.2. Furthermore, at the same laser energy the Raman spectra depend on the type of sample and on the diameter of the tubes.

Although the origin of the large variation in the spectra is not fully understood, Raman experiments are widely used to characterize the tubes in the sample. Reliable information about the nanotubes from Raman experiments, however, can only be obtained if the origin of this excitation-energy dependence is known. We show here that it can be explained by defect-induced, double-resonant Raman scattering. The observation of a different Raman spectrum means that different phonons are involved but all stem from the same nanotube. In contrast, previous interpretations based on single-resonances [155] assumed that the same phonon modes from different tubes cause the variation of the spectra. An unambiguous answer to this con-

Figure 5.2: Raman spectra of bundled carbon nanotubes (HiPCO-produced “bucky-pearls” [50, 154]) at different excitation energies. The mean tube diameter is ≈ 1 nm. The gray lines were measured on arc-discharge grown nanotubes with mean tube diameter ≈ 1.4 nm. The spectra are scaled to approximately the same HEM amplitude and offset vertically. The *D* mode is much larger in the sample of arc-discharge grown tubes than in the HiPCO tubes, if compared to the HEM intensity. In both samples the position of the *D* mode and the HEM changes with laser energy.



troversty is found by Raman experiments on the same individual tube, which we present in this chapter.

An introduction to the general theory of double-resonant Raman scattering is given in Sect. 5.1. In the two following sections we describe this concept for the *D* mode in carbon nanotubes and graphite, respectively. In Sect. 5.4 we show that the double-resonance model fully explains the origin and properties of the high-energy modes in carbon nanotubes, in contrast to previous interpretations. The essential experiments that support our interpretation are Raman measurements on an individual nanotube (Sect. 5.4.1). The case of metallic tubes is discussed in Sect. 5.4.2; the role of defects in the scattering process is studied in Sect. 5.4.3. In Sect. 5.5 we present measurements of the absolute Raman cross section of the RBM in carbon nanotubes and compare them with theoretical predictions. The discussion on the competing models of single- and double-resonance scattering is summarized in the last section. Parts of this chapter were published in Ref. [31].

5.1 Introduction: Double-resonant Raman scattering

In this section we give an introduction to defect-induced, double-resonant Raman scattering [156]. We explain the characteristics of this effect, in particular the process which leads to a laser-energy dependence of the Raman frequencies in higher-order scattering. In principle, the defect allows large phonon wave vectors \mathbf{q} to contribute to the spectra; the double-resonance

mechanism then selectively enhances *specific* large- q modes. The observed frequency shift as a function of laser energy thus corresponds to scanning part of the phonon dispersion.

The Raman cross section for first-order Raman scattering is proportional to $|K_{2f,10}|^2$, where the Raman matrix element [156]

$$K_{2f,10} = \sum_{a,b} \frac{\langle \omega_2, f, i | H_{eR,\rho} | 0, f, b \rangle \langle 0, f, b | H_{ep} | 0, 0, a \rangle \langle 0, 0, a | H_{eR,\sigma} | \omega_1, 0, i \rangle}{(E_l - E_{ai}^e - i\gamma)(E_l - \hbar\omega_{ph} - E_{bi}^e - i\gamma)}. \quad (5.1)$$

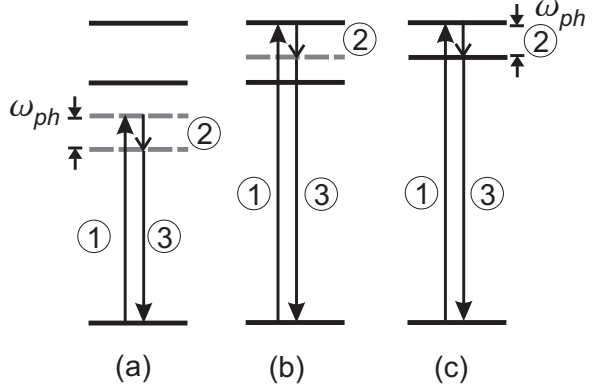
The states are indicated by the electronic ground state i and the intermediate electronic states a and b , by the initial and final phonon states 0 and f , which denote the absence and the excitation of the phonon, respectively, and by the incoming (ω_1) and outgoing (ω_2) photon. E_l denotes the laser energy and $\hbar\omega_{ph}$ the phonon energy. E_{ai}^e , E_{bi}^e are the energy differences between the electronic intermediate states and the ground state. γ is a broadening parameter reflecting the inverse lifetime of the electronic states.

Figure 5.3 shows a schematic view of (a) non-resonant, (b) single-resonant, and (c) double-resonant Raman scattering.¹ The solid lines indicate real electronic states; the dashed gray lines denote virtual intermediate states. The incoming photon with energy E_l excites an electron-hole pair (1), the excited electron is scattered by emitting a phonon with energy $\hbar\omega_{ph}$ (2), and the electron recombines with the hole by emitting a photon with energy E_2 (3). If both intermediate states are virtual as in Fig. 5.3 (a), the process is called non-resonant. If the laser energy matches the transition energy between two real electronic states [Fig. 5.3(b)], the Raman process is single-resonant. In this case, in Eq. (5.1) the first term in the denominator vanishes for $\gamma = 0$ and the Raman intensity diverges. To obtain double-resonant scattering, where two of the intermediate states are real [Fig. 5.3(c)], the electronic states must provide three suitable energy levels with energy differences equal to E_l , $\hbar\omega_{ph}$, and $E_l - \hbar\omega_{ph}$. Experimentally, this rather restrictive condition can be fulfilled, if the electronic band structure of the material is tuned accordingly by applying uniaxial stress, an electric or magnetic field [157–160]. In semiconductor superlattices the intersubband transitions can be designed to match the required energy differences for the double-resonance condition [161]. In these examples, double-resonant scattering is obtained for only one particular wavelength of the incoming light.

In the above description of resonant and non-resonant Raman scattering, we restricted ourselves to first-order scattering which (for visible light) involves only Γ -point phonons. We extend the discussion now to higher-order processes, including scattering by two phonons of

¹In fact, in first-order scattering the process shown in Fig. 5.3 (c) is triply resonant, because the first two resonant transitions determine the remaining third one. The third transition is automatically resonant if there are no additional intermediate states.

Figure 5.3: Non-resonant Raman scattering (a), single-resonant (b), and multiple-resonant scattering (c). The solid lines indicate real electronic states. The dashed lines represent virtual states, *i.e.*, energies which are not eigenenergies of the system. In the non-resonant process (a), both intermediate electronic states are virtual. If the laser energy matches a real electronic transition [first step in (b)], the Raman process is single resonant. If the special condition (c) is met, *i.e.*, in addition to (b) another electronic transition matches the phonon energy, a double- or triple-resonance occurs.



opposite wave vector or elastic scattering mediated by defects. In higher-order processes, the phonon wave vectors are not restricted to zero, see Sect. 4.1.

In Fig. 5.4 (a) two linear electronic bands are shown, which can be taken as an approximation to the graphene bands at the K point or the bands that cross the Fermi level in metallic tubes, see Chap. 3. Here, for any incoming laser energy a real transition is found. With increasing laser energy, the resonant transition occurs at larger electron wave vector \mathbf{k}_i . If the resonantly excited electron can be scattered by phonons with arbitrary wave vector \mathbf{q} , a second resonance is found for a particular phonon. Both, energy and wave vector of this phonon are determined by the phonon dispersion and the double-resonance condition. The two resonant transitions which constitute the double resonance, are in our example the excitation of the electron by the incoming light and the inelastic scattering by the phonon. Because quasi-momentum is conserved, the process indicated in Fig. 5.4 (a) must include the scattering by a second phonon (“second-order” Raman scattering) or by a defect (elastic scattering, shown here). In the case of defect-scattering, the Raman matrix element is given by [156]

$$K_{2f,10} = \sum_{a,b,c} \frac{\mathcal{M}_{eR,\rho} \mathcal{M}_{e-def} \mathcal{M}_{ep} \mathcal{M}_{eR,\sigma}}{(E_l - E_{ai}^e - i\gamma)(E_l - \hbar\omega_{ph} - E_{bi}^e - i\gamma)(E_l - \hbar\omega_{ph} - E_{ci}^e - i\gamma)} + \sum_{a,b,c} \frac{\mathcal{M}_{eR,\rho} \mathcal{M}_{ep} \mathcal{M}_{e-def} \mathcal{M}_{eR,\sigma}}{(E_l - E_{ai}^e - i\gamma)(E_l - E_{bi}^e - i\gamma)(E_l - \hbar\omega_{ph} - E_{ci}^e - i\gamma)}, \quad (5.2)$$

where the notation is the same as in Eq. (5.1) and the matrix elements in the numerator are abbreviated as \mathcal{M}_i . \mathcal{M}_{e-def} is the matrix element for the interaction between the electron and the defect. The first term in the sum describes the process, where the electron is first inelastically scattered by a phonon and second elastically by a defect; in the second term, the time order is reversed. For scattering by two phonons, Eq. (5.2) is modified accordingly.

The sum over all possible intermediate electronic states a, b, c in Eq. (5.2) includes all non-resonant and single-resonant processes. The case $\mathbf{q} = 0$ is given if the electron wave vector

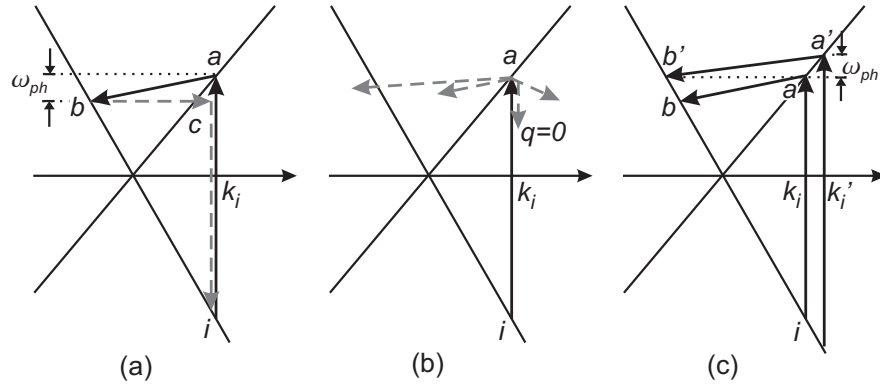


Figure 5.4: (a): Double-resonant Raman scattering at two linear electronic bands as at the K point in graphene. Resonant (non-resonant) transitions are indicated by solid (dashed, gray) arrows. The incoming light resonantly excites an electron-hole pair at wave vector k_i . The electron is resonantly scattered by a phonon from state a to b . From b the electron is elastically scattered by a defect back to c (with $k_c \approx k_i$), where it recombines with the hole. The last two transitions are non-resonant. (b): Examples of single-resonant scattering, where only the first transition is resonant. The excited electron is non-resonantly scattered by phonons with different wave vectors, including the case $q = 0$. (c): Double-resonant scattering at two different laser energies. The double-resonant phonon wave vector and hence frequency depend on the incoming energy. In (b) and (c) the last two transitions are omitted for simplicity, *i.e.*, elastic scattering by the defect and recombination of the electron and hole.

$k_b = k_a$. This is illustrated in Fig. 5.4 (b), where some examples for single-resonant scattering with different phonon wave vectors and phonon frequencies are shown, including the process for $q = 0$. The intensity of the single-resonant processes shown in Fig. 5.4 (b) is large, because one of the terms in the denominator of the Raman cross section vanishes. If for a particular combination of q and $\hbar\omega_{ph}$ the double-resonance condition is fulfilled, however, a second term vanishes and the Raman intensity is further increased. The double-resonant phonon mode is selectively enhanced and gives rise to a peak in the Raman spectrum. For laser energies below the first optical transition energy, *i.e.*, in non-resonant scattering, the Raman spectrum resulting from higher-order scattering resembles the phonon density of states; such scattering, however, is comparatively weak.

In Fig. 5.4 (c) we illustrate the effect on the Raman spectra when changing the incoming photon energy. As mentioned above, the electron wave vector $k_i = k_a$ at which the incoming resonance occurs increases with laser energy. Consequently, the phonon that scatters the electron *resonantly* to a state $k_b = k_a - q$ must have a larger wave vector. Scattering by this phonon will be enhanced and appears in the Raman spectrum. The Raman frequency of this mode is different from the frequency observed at smaller laser energy, depending on the phonon dispersion. Therefore, by changing the laser energy one can, in principle, measure the phonon dispersion. In general, this unusual dependence of Raman frequencies on the wavelength of the incoming light is a signature of double-resonant Raman scattering, if the process involves phonons with non-zero wave vector.

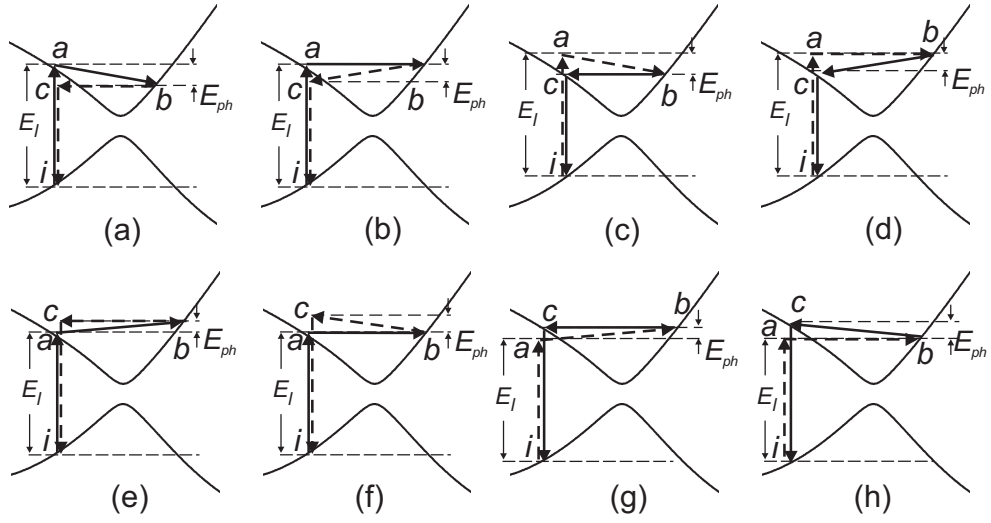


Figure 5.5: Double-resonant processes for Stokes (a-d) and anti-Stokes (e-h) scattering. Solid and dashed arrows indicate resonant and non-resonant transitions, respectively. In each row, the first two pictures show an incoming resonance; the last two pictures show an outgoing resonance. In (a) [and from hereon in every other picture] the electron is scattered first inelastically by a phonon and then elastically by a defect. This time order is reversed in (b) and the corresponding other sets.

In the examples above the incoming light was in resonance with the electronic states (incoming resonance). Alternatively, the scattered light can be in resonance (outgoing resonance). We show in Fig. 5.5 (upper row) the four processes resulting from the two time orders in Eq. (5.2) and incoming/outgoing resonance. Moreover, in case of different electron and hole dispersions, the analogous processes have to be taken into account, where the hole instead of the electron is scattered. Finally, if the bands are not symmetric with respect to the minimum, the contributions depend on whether the optical transitions occur on the left or on the right of the minimum. All processes shown in Fig. 5.5 (a)-(d) are automatically contained in Eq. (5.2), if the sum is taken over all intermediate states.

The first term of Eq. (5.2) can be evaluated for the example of Fig. 5.4 and yields [133]

$$K_{2f,10} \propto \frac{b}{(\kappa_2 - q \frac{v_2}{v_2 - v_1})(\kappa_2 + q \frac{v_1}{v_2 - v_1})}, \quad (5.3)$$

where v_1 and v_2 are the Fermi velocities in the two bands and b is a slowly varying function of q , $b = \ln(\kappa_2/\kappa_1)(2\kappa_2 - q)/[(v_2 - v_1)^2 \hbar \omega_{ph}]$, and $\kappa_1 = (E_l - i\hbar\gamma)/(v_2 - v_1)$ and $\kappa_2 = (E_l - \hbar\omega_{ph} - i\hbar\gamma)/(v_2 - v_1)$. A double resonance occurs for those combinations of phonon wave vector q and energy $\hbar\omega_{ph}(q)$, for which one of the terms in the denominator of Eq. (5.3) vanishes [156]. Here the second term corresponds to the double-resonance process shown in Fig. 5.4 (a), where the optical transition occurs to the right ($k_i > 0$); the first term yields a double-resonance if $k_i < 0$ in our example. The denominator vanishes for the double-resonant phonon wave vectors

$$q_1 = \frac{E_l - \hbar\omega_{ph}(q)}{v_2} \quad \text{and} \quad q_2 = \frac{E_l - \hbar\omega_{ph}(q)}{-v_1}. \quad (5.4)$$

In the approximation of $\hbar\omega_{ph} \approx 0$ and symmetric electron bands, we can simplify this condition to the so-called $q = 2k$ rule, *i.e.*, the double-resonant phonon wave vector is given by twice the wave vector of the resonantly excited electron. This is correct if the defect is involved in a resonant transition as for instance shown in Fig. 5.5 (b) and (f), and if $v_1 = -v_2$. The $q = 2k$ rule is a useful approximation for estimating the double-resonant phonon wave vector. It cannot, however, substitute the full integration of the Raman cross section in Eq. (5.2) when deriving precise phonon frequencies or calculating a Raman spectrum.

In Fig. 5.6 we plot the Raman intensity, calculated from the analytical expression in Eq. (5.3), as a function of q for different laser energies. We chose $\hbar\omega_{ph}(q)$ to depend linearly on q ; the Raman spectrum is obtained if the q axis is transformed into $\hbar\omega_{ph}(q)$.² We see in Fig. 5.6 the clear dependence of the selected phonon wave vectors and hence the Raman frequencies on excitation energy. The double-peak structure is due to the contributions q_1 and q_2 in Eq. (5.4). Because of the linear electron and phonon dispersion, the shift with laser energy is linear as well. The effect of the electronic bands on the laser-energy dependence is shown in Fig. 5.6 (b), where the Fermi velocities v_1 and v_2 were doubled. Now the same change in laser energy results in a smaller change in the electron wave vector k_i of the resonant optical transition. Therefore, the double-resonant phonon wave vector is less affected as well. Again, as the dispersion relations are linear in our example, the shift of the Raman peaks with laser energy decreases by a factor of two when the slope of the electronic bands is doubled. It is obvious that a larger phonon dispersion results in a more pronounced laser-energy dependence of the Raman spectra.

So far, we considered Stokes scattering, the creation of a phonon in the Raman process. Usually, Stokes and anti-Stokes spectra differ only in intensity, depending on the lattice temperature. In contrast, in double-resonant scattering also the observed phonon frequencies depend on whether the Stokes or the anti-Stokes spectrum is recorded. Again, this is a consequence of

²This is trivial for a linear phonon dispersion. Otherwise the phonon density of states has to be taken into account.

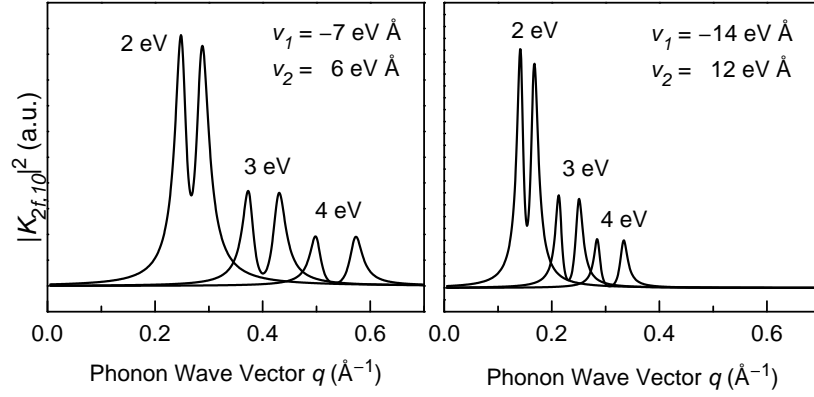


Figure 5.6: Raman intensity as a function of the phonon wave vector for laser energies between 2 and 4 eV, calculated from Eq. (5.3) for linear electronic bands. The double-peaks correspond to q_1 and q_2 in Eq. (5.4); here $q_2 < q_1$. On the right, the slope of the electronic bands is doubled; the shift of the Raman peaks with laser energy is therefore smaller by a factor of two. We used a linear phonon dispersion and a broadening $\gamma = 0.1$ eV.

different double-resonance conditions for the Stokes and anti-Stokes process at a given laser energy, as illustrated in Fig. 5.5 (lower row). In the example shown in Fig. 5.5, the phonon wave vector is larger in anti-Stokes than in Stokes scattering. This can be seen by comparing for instance Fig. 5.5 (a) and (e). For anti-Stokes scattering, the sign of the phonon energy in Eq. (5.2) has to be inverted. Because of time-reversal symmetry, the anti-Stokes process at given E_l^{AS} corresponds to the Stokes process at $E_l^S \approx E_l^{AS} + \hbar\omega_{ph}$, see for details also Ref. [162].

In second-order scattering, the elastic scattering by a defect is replaced by inelastic scattering by a second phonon. In the case of two phonons with the same frequency but opposite wave vector, the Raman shift is about twice the single-phonon (first order) frequency and hence the shift with laser energy is approximately doubled. Because the quasi-momentum conservation can always be fulfilled for scattering by two phonons, the second-order spectrum can be always double-resonant, independently of the presence of defects.

The observed intensities of the Raman peaks are not solely determined by the double resonance process. Those modes for which the double resonance takes place close to a singularity in the electronic joint density of states, are further enhanced; the same holds for single-resonant scattering. This effect is contained in the expressions of the Raman cross section [Eqs. 5.1 and 5.2], if the sum is taken over all intermediate states. If the joint density of states is large at a transition energy close to the incoming laser energy, the corresponding incoming resonances occur more often in the sum than for a smaller density of states. Furthermore, the intensity depends on the phonon density of states. This is taken into account when converting the phonon wave vector q into the phonon energy $\hbar\omega_{ph}$.

In summary, the laser-energy dependence of the observed Raman frequencies is a fingerprint of double-resonant Raman scattering with large phonon wave vectors. Further criteria that can be experimentally observed are the difference between Stokes and anti-Stokes spectra, a large intensity, and a variation of the line shape which cannot be described by a single Lorentzian. To allow large phonon wave vectors, higher-order scattering by two (or more) phonons or defects, relaxing the translation symmetry, is required. The double-resonance is experimentally accessible if the phonon dispersion is large and the electronic bands have a gap below the available laser energy or even cross the Fermi level in a single point as in semimetals.

5.1.1 Selection rules for $q \neq 0$ in carbon nanotubes

To apply the concept of defect-induced, double-resonant Raman scattering to carbon nanotubes, the selection rules have to be found for second-order scattering with $q \neq 0$, including either defect scattering or a second phonon. As for first-order scattering, they can be derived in the standard way from the character table of the line group [63, 64] or found from the conservation of quantum numbers.³ We will see that phonon branches of carbon nanotubes which are derived from a Raman-active Γ -point mode are always allowed. We assume that the defect cannot change the symmetry of a state it interacts with ($m_{\text{defect}} = 0$), *i.e.*, electrons can be scattered by the defect only within the same band. As for scattering with Γ -point modes, the phonon provides the quantum numbers by which the electronic system is changed in a given scattering geometry, *e.g.*, $\Delta m = \pm 1$ for x and z polarization of incoming and outgoing light, respectively. The required quantum numbers are summarized in Table 5.1. The σ_x and the σ_h parity quantum numbers correspond to the vertical and horizontal mirror planes, respectively, and exist in achiral tubes only, see Chap. 2. The σ_h parity (given in brackets) is defined only at $q = 0$. The vertical mirror plane (σ_x) is present at $q \neq 0$ as well if $m = 0$ or $m = n$. From the conservation of the σ_x parity it follows that the entire LO branch (including $q = 0$) is allowed in zig-zag tubes and forbidden in armchair tubes; *vice versa*, the TO branch is allowed in armchair tubes but forbidden in zig-zag nanotubes. In two-phonon scattering, the change in quantum numbers is provided in total by both phonons, *i.e.*, $\Delta m = m_{ph,1} + m_{ph,2}$. Therefore, in contrast to first-order scattering, also modes with $|m| > 2$ can contribute to the two-phonon signal. They scatter electrons from one band into another band. The quasi-angular momentum m of the phonon defines to which band the excited electron is scattered through $m_b = m_a + m_{ph}$, where the subscripts a and b refer to the intermediate states in Eq. (5.2).

If the phonon wave vector is larger than π/a , the quasi-angular momentum m is not a conserved quantum number and the *Umklapp* rules [Eq. (2.20) and (2.21)] apply. For achiral tubes,

³Note that also the quasi-momentum conservation rule, $q_1 = q_2 \pm q_{ph}$, is found formally from the full space group character table as given in Refs. [63, 64].

Table 5.1: Phonon quantum numbers conserving the total quantum numbers in $q \neq 0$ Raman scattering. The scattering geometry is given by the polarization of the incoming and scattered light, where z is the direction of the tube axis. The parity quantum numbers given in brackets are only defined at $q = 0$. In chiral tubes σ_h and σ_x are not a symmetry operation and the parity quantum numbers σ_x and σ_h are not present at all. For two-phonon scattering, $m_{ph} = m_{ph,1} + m_{ph,2}$.

Scattering geometry	Allowed phonon quantum numbers		
	m_{ph}	$\sigma_{x,ph}$	$\sigma_{h,ph}$
(z, z)	0	+1	(+1)
$(x, z), (z, x), (y, z), (z, y)$	± 1	–	(–1)
$(x, x), (y, y)$	$0, \pm 2$	+1 (if $m = 0$)	(+1)
$(x, y), (y, x)$	$0, \pm 2$	–1 (if $m = 0$)	(+1)

$m = 0$ changes into $m = n$ for $q \in (\pi/a, 2\pi/a]$. In chiral tubes, it is more convenient to use the helical quantum numbers \tilde{k}, \tilde{m} ; then the entire $\tilde{m} = 0$ band is allowed in (z, z) configuration.

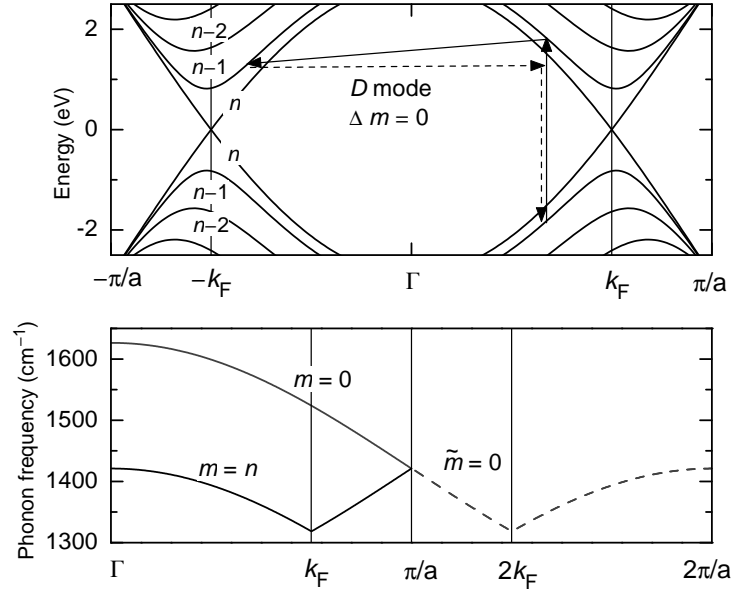
In summary, the selection rules for large- q Raman scattering in carbon nanotubes are given by the conservation of the quasi-angular momentum m . If $q > \pi/a$, the *Umklapp* rules must be additionally applied. For $m = 0$ and $m = n$ phonons in achiral tubes, the allowed modes are further restricted by parity quantum numbers. In general, for $q \neq 0$ the selection rules are less restrictive than for Γ -point phonons, since some of the parity quantum numbers are defined only at $q = 0$. If a phonon mode is forbidden at the Γ point but allowed for $q > 0$, however, continuity prevents the mode from having a large Raman signal at small q .

5.2 The D mode in carbon nanotubes

In Fig. 5.2 we saw already that the disorder-induced D mode of carbon nanotubes shifts significantly with excitation energy. This peculiar behavior is known for long from the D mode in graphite [163–166]. The origin of the excitation-energy dependence in graphite was resolved by Thomsen & Reich [133] as defect-induced, double-resonant Raman scattering. Laser-energy dependent studies in carbon nanotubes first focused on the D mode as well, because of its obvious correspondence to the graphite D mode and because the shift with laser energy is an order of magnitude larger than the shift of the high-energy modes and therefore easier to detect. The shift of the HEM frequencies will be studied in detail in Sect. 5.4. Here we discuss the origin of the D mode in carbon nanotubes and show the correspondence and the differences to graphite.

By applying the concept of defect-induced, double-resonant Raman scattering (Sect. 5.1), the D -mode spectra of carbon nanotubes are found theoretically. As discussed in Sect. 5.1, the double-resonance is determined by both electron and phonon dispersions. We make use of the

Figure 5.7: Electronic band structure (top) and model phonon dispersion (bottom) of an armchair nanotube. The Fermi wave vector k_F is at $2/3 \frac{\pi}{a}$ in armchair tubes. Resonant and non-resonant transitions are indicated by solid and dashed arrows, respectively. Note that the optical transition between the bands crossing the Fermi level ($m = n$) is forbidden by symmetry.



electronic band structure presented in Chap. 3 and the selection rules predicted by symmetry (Sects. 2.2 and 5.1.1). For the phonons we will use model dispersions.

The scattering process of the D mode in armchair tubes is shown in Fig. 5.7 (top). For z -polarized light, an electron-hole pair is excited in the band with $m = n - 1$, near the Fermi wave vector k_F for visible light. In the zone-folding approach, the Fermi wave vector k_F corresponds to the K point of graphite. The electron is scattered across the Γ point within the same band by a double-resonant phonon with $q_{\text{dr}} \approx 2k_F = \frac{4}{3} \frac{\pi}{a}$. It is then scattered back elastically by a defect and recombines with the hole (Sect. 5.1). Here the phonon must have $m_{\text{ph}} = 0$, because the defects lead to a relaxation of the quasi-linear momentum conservation only; it cannot change the quasi-angular momentum quantum number m , see Table 5.1.

In the lower part of Fig. 5.7 we give an example of a model phonon dispersion as the one used in the calculations below. The required phonon wave vector $q_{\text{dr}} \approx 2k_F$ is larger than the Brillouin zone. In this case, we have to apply the *Umklapp* rules Eq. (2.20):

$$2k_F = \frac{4}{3} \frac{\pi}{a} \equiv \frac{4}{3} \frac{\pi}{a} - \frac{2\pi}{a} = -\frac{2}{3} \frac{\pi}{a}.$$

and

$$m' = m + n = 0 + n = n$$

Thus in the conventional Brillouin zone the allowed phonon that leads to the D mode has a wave vector $q_{\text{dr}} \approx 2\pi/3a = k_F$ and band index $m = n$ in armchair tubes. In the extended or

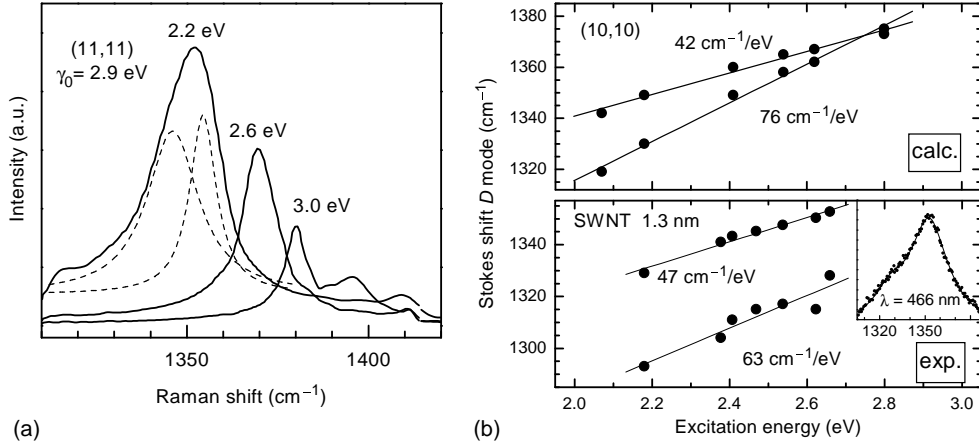


Figure 5.8: (a) *D* mode spectra calculated for the (11,11) tube [149]. The electronic band structure was calculated by the first-neighbors tight-binding approximation with $\gamma_0 = 2.9$ eV, and $\gamma = 0.1$ eV. The *D*-mode frequency clearly depends on excitation energy. The intensity decreases with increasing laser energy. (b) *D*-mode frequency as a function of excitation energy. Top: calculation for the (10,10) tube; bottom: experimental data from bundled single-walled nanotubes with a mean diameter of 1.3 nm. The inset shows an experimental spectrum.

helical Brillouin zone, *i.e.*, in the description by (\tilde{k}, \tilde{m}) quantum numbers, the phonon branch with $\tilde{m} = 0$ is taken (dashed line in Fig. 5.7).

Both electron and phonon states relevant for the double-resonant *D* mode are derived from the *K* point in graphite. Therefore, the double-resonant phonon corresponds to a *K*-point mode and the observed frequency is similar to the *D* mode in graphite. For higher incoming laser energy, the resonant optical transitions occur at larger distance from k_F . Hence q_{dr} is smaller if the optical transition is on the left of the conduction-band minimum in Fig. 5.7 and larger if the optical transition is on the right. In both cases, the double-resonant phonon wave vector moves away from k_F . This results in an increase of the phonon frequency with laser energy as the phonon band $m = n$ possesses a minimum at k_F (or $\tilde{m} = 0$ at $2k_F$).

The Raman spectra of the *D* mode, calculated according to the scattering process in Fig. 5.7, are shown in Fig. 5.8 (a) for the (11,11) tube. The spectra show a clear dependence on laser energy. The Raman intensity decreases with increasing laser energy, because the electron density of states is smaller for electron wave vectors away from k_F . The *D* mode is not symmetric and consists of two peaks, which shift at different rates. Several reasons account for this line shape. The conduction band minimum is not exactly at $k_F = 2\pi/3a$, the minimum is not symmetric, and incoming and outgoing resonances have slightly different double-resonance conditions, see also Fig. 5.5. The structure due to incoming and outgoing resonance is not resolved. In chiral nanotubes, the peak structure can be even more complex due to several electronic bands contributing simultaneously. In Fig. 5.8 (b) we show the frequency of the *D* mode as a function of laser energy. The calculated shifts for a (10,10) tube (42 and 76 cm⁻¹/eV) agree well with the

experiment on SWNT bundles (47 and 63 cm^{-1}/eV). The experimental spectrum in the inset shows that the D mode is not a single line but indeed contains at least two peaks.

Comparing tubes of the same chiral angle with different diameter, we find that at low excitation energy the absolute D -mode frequency is lower for smaller tubes but the rate by which the D mode shifts is larger. This is understood from the scattering process shown in Fig. 5.7. A smaller diameter results in a larger separation of conduction and valence bands. At the same laser energy, the wave vector of the excited electron is closer to k_F and hence the phonon frequency is lower than in larger-diameter tubes. Since the slope of the electron bands is smaller near k_F , the same variation in laser energy results in a larger change of the excited-electron wave vector. Therefore, the change of the double-resonant phonon wave vector and hence the frequency shift is larger. The predicted diameter dependence of the D -mode frequency was observed in experiments on isolated tubes and bundles [44, 167, 168].

In the above discussion we showed that both the electron and phonon wave vectors that are involved in D -mode scattering correspond to the Fermi wave vector k_F (K point in graphite). Therefore, they are approximately the same. Simultaneously, the double-resonant phonon wave vector q_{dr} is about twice the electron wave vector. Only if the electron wave vector is at $2/3$ of the Brillouin zone, it is equal to the phonon wave vector $q_{\text{dr}} \approx |2k_F - \frac{2\pi}{a}| = \frac{2\pi}{3a}$. This condition, *i.e.*, $k_F = 2\pi/3a$, is only fulfilled in $\mathcal{R} = 3$ tubes, see Ref. [79] and Chap. 3. A strong D -mode scattering and a systematic excitation-energy dependence thus cannot be observed in $\mathcal{R} = 1$ tubes [149]. Consequently, a weak Raman signal in the D -mode region does not necessarily indicate fewer defects in the investigated nanotubes but can be due to the presence of $\mathcal{R} = 1$ tubes. On the contrary, a strong D mode and a systematic shift with laser energy is an indication of metallic tubes.⁴ This prediction is based on the assumption that only phonons with $m = 0$ (and, including *Umklapp* processes, $\tilde{m} = 0$) are allowed by symmetry. If elastic scattering by the defect could change the quasi-angular momentum m as well – which is unlikely – the D mode would be double-resonant for any chirality [169].

As an example of a chiral $\mathcal{R} = 3$ tube we calculated the D mode of the (8,2) tube. The electronic band structure given by helical quantum numbers is shown in Fig. 5.9. As for armchair tubes, the optical transitions occur near $2/3$ of the (helical) Brillouin zone, and the double-resonant phonon wave vector $q_{\text{dr}} \approx \frac{4}{3}\frac{\tilde{\pi}}{a}$, where $\tilde{\pi} = q\pi/na$, see Chap. 2. The resulting D -mode spectra are shown in Fig. 5.10. The main peak shifts by $40 \text{ cm}^{-1}/\text{eV}$.

Above we showed that a strong D -mode scattering with a systematic excitation-energy dependence cannot occur in $\mathcal{R} = 1$ tubes. In second-order overtone scattering, on the other hand, the condition $m_{ph} = 0$ has to be fulfilled only by the sum of both phonons, $m_{ph} =$

⁴All tubes with $\mathcal{R} = 3$ are metallic; semiconducting tubes always have $\mathcal{R} = 1$. Only a small fraction of metallic tubes has $\mathcal{R} = 1$, among them all metallic zig-zag tubes.

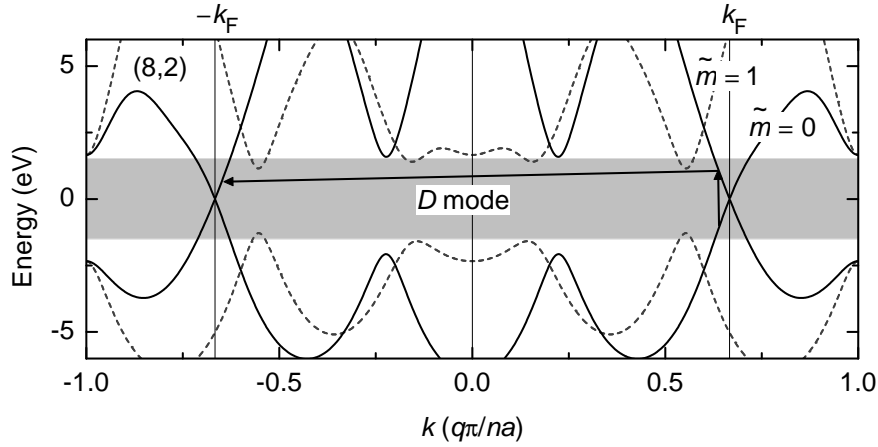


Figure 5.9: Electronic band structure of the (8,2) tube calculated within the tight-binding approximation including third-nearest neighbors. The visible range of optical transitions is shaded; the scattering process for the D mode is indicated by arrows. Because the (8,2) tube has $\mathcal{R} = 3$, the $\tilde{m} = 0$ conduction and valence bands cross the Fermi level at $k_F = 2\tilde{\pi}/3a$ [79]. $\tilde{\pi} = q\pi/na = 14\pi/a$, and $\tilde{m} = 0, 1$. Scattering by phonons with $\tilde{m} = 0$ and $q = 2k_F$ leads to the D mode.

$m_{ph,1} + m_{ph,2} = 0$, see Table 5.1. Thus the second-order D^* -mode becomes allowed in any tube, if $m_{ph,1} = -m_{ph,2}$ [170]. We will discuss this here for zig-zag nanotubes. Since zig-zag tubes always have $\mathcal{R} = 1$, *i.e.*, the singularities in the joint density of states are at the Γ point, D -mode scattering is not allowed for $m_{\text{defect}} = 0$. In Fig. 5.11 we show the electronic band structure of the (17,0) tube near the Γ point. In (a) the defect-induced double-resonance in (z, z)-polarization is displayed, leading to the first-order spectrum. Only phonons with $m_{ph} = 0$ are allowed. Since the double-resonant phonon wave vectors are rather close to the Γ point, the scattering process in (a) yields Raman peaks in the range of the high-energy modes, see Sect. 5.4. On the other hand, for Raman peaks in the D -mode range, phonons with $m \approx 2n/3$ are required. In this case, the scattered electron with $m_b = m_a + 2n/3$ cannot recombine with the hole (m_a) in a z -polarized optical transition, and the D mode does not appear in the first-

Figure 5.10: D mode spectra of the (8,2) tube. The phonon dispersion was modeled by an analytical function; the broadening parameter was set to $\gamma = 0.05$ eV. The main peak shifts by $40 \text{ cm}^{-1}/\text{eV}$ and the smaller one by $27 \text{ cm}^{-1}/\text{eV}$.

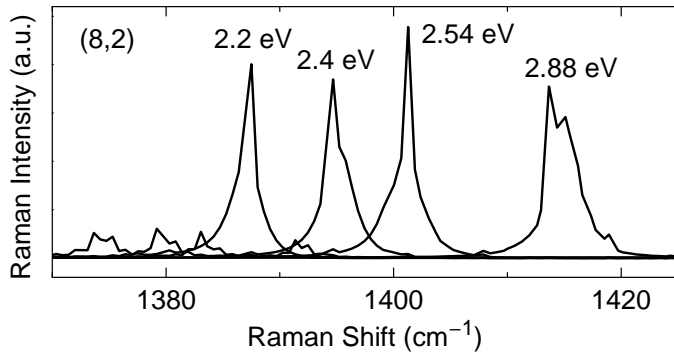
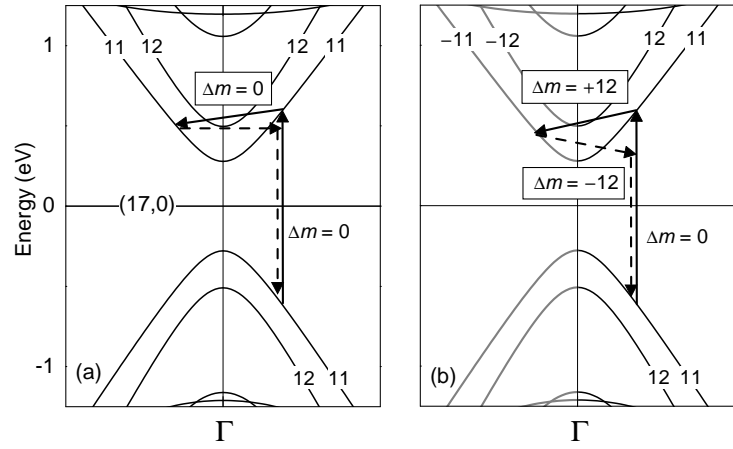


Figure 5.11: Electronic band structure of the (17,0) tube near the Γ point. The numbers indicate the band indices m . The band extrema are at the Γ point; the lowest optical transitions occur in the bands with $m \approx 2n/3$. In achiral tubes, the states with m and $-m$ are degenerate. (a) Double-resonant scattering with an $m = 0$ phonon and defect, resulting in high-energy modes. (b) Double-resonant scattering in second order by two phonons with $m = 12$ and $m = -12$, leading to the overtone D^* of the D mode.



order spectrum of zig-zag tubes. In Fig. 5.11 (b) a second-order process is shown leading to the D^* mode. For example, if the electron-hole pair is excited in the $m_a = 11$ band, a phonon with $m_{ph} = 12$ scatters the electron to the band $m_b = (m_a + m_{ph}) \bmod 2n = 11 + 12 - 34 = -11$, see Fig. 5.11 (b). A second phonon with $m_{ph} = -12$ scatters the electron back to near the original band. Because of the σ_h parity quantum numbers of the states at the Γ point, phonons with even parity are allowed only if $|m_a|$ and $|m_b|$ are both smaller or both larger than $2n/3$, see Chaps. 2 and 3. *Vice versa*, if the phonon has $\sigma_h = -1$, one of the electronic states must have $|m| > 2n/3$ and the second one $|m| < 2n/3$. Taking into account these selection rules, we calculated the D^* -mode spectra of the (19,0) tube in Fig. 5.12. The D^* mode is in the expected frequency range and shifts by $\approx 120 \text{ cm}^{-1}/\text{eV}$, in reasonable agreement with experiments [171].

The double-resonance process as the origin of the D mode in graphite and carbon nanotubes is well established and validated by experiments. Nevertheless, some interpretations attribute the *shift* of the D mode in carbon nanotubes to the selective enhancement of different tubes in

Figure 5.12: D^* Raman spectra calculated for the (19,0) tube at different excitation energies [170]. The phonon dispersion was taken from the force-constants calculations described in Sect. 4.3.2. The shift with laser energy amounts to $\approx 120 \text{ cm}^{-1}/\text{eV}$.

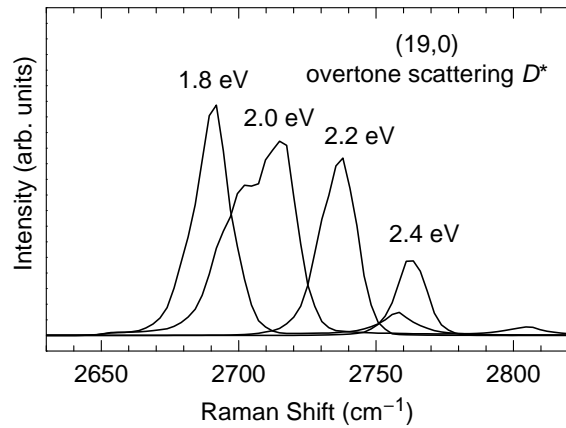
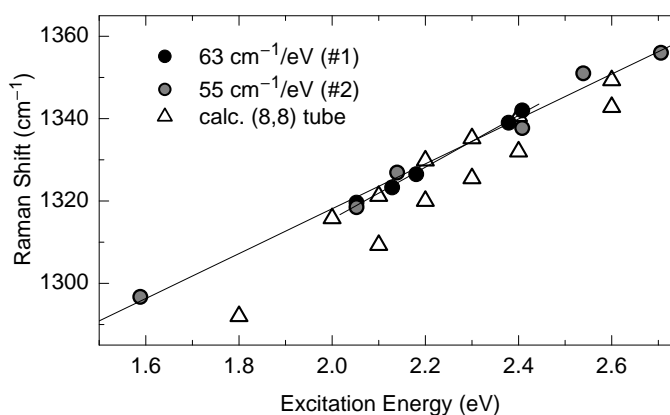


Figure 5.13: *D*-mode frequency as a function of laser energy measured on isolated tubes on two different spots of the sample (filled circles). The open triangles are calculated values for the (8,8) tube, where a model dispersion was used for the phonons. The calculated *D* mode is composed of two peaks; the upper one agrees very well with the experiment. In the experimental data, the individual peaks were not resolved. For the spectra see Fig. 5.25.



resonant Raman scattering [169, 172]. The *D*-mode frequency changes in this picture because at a different excitation energy the Raman signal from a different tube is observed; a *D*-mode shift in a single tube is not predicted, in contrast to the model explained above. Laser-energy-dependent Raman measurements, however, showed that the *D* mode of an isolated tube is not constant but shifts as in experiments on bulk samples. In Fig. 5.13 we present the *D*-mode frequencies as a function of excitation energy in an isolated tube and a thin bundle [173], for the measurements on isolated tubes see Sect. 5.4. The *D* mode shifts at a rate similar to that observed in bundles, showing that the dependence on excitation energy indeed is the property of a *single* tube and not an ensemble effect.

Finally, we want to comment on the phonon dispersion. In this section we always used a model dispersion like the one in Fig. 5.7, that was adapted to the theoretically predicted longitudinal (LO) branch in graphite. Although in armchair tubes the $m = 0$ LO branch is actually forbidden because of its σ_x parity quantum number being odd (Chap. 4), we used it in the calculations because it was the only one predicted with a minimum at about $1200 - 1300 \text{ cm}^{-1}$. In chiral tubes, the σ_x parity quantum number does not exist, thus both LO and TO branches are allowed. Meanwhile we found from inelastic X-ray scattering in graphite (Chap. 4) that the TO branch was incorrectly predicted in most of the previous calculations. The experiments showed that in fact the TO is at about the same frequencies as the LO was believed to be. Therefore, the *D* mode in carbon nanotubes comes from the TO-derived phonon branch instead from the LO, as well as the *D* mode in graphite. This is consistent with the selection rules; for graphite we discuss the *D* mode, based on the new experimental data, in Sect. 5.3. Since no revised calculations of the phonon dispersion in carbon nanotubes are available up to now, we stayed with the model dispersions in this section. The implications of the double-resonant model as well as the good qualitative agreement of the *D*-mode calculations with Raman experiments are not affected by this correction, because just the name of the model dispersions had to be altered.

5.3 The D mode in graphite

We showed above for carbon nanotubes that the double-resonance model provides an excellent understanding of all properties of the D mode. Nevertheless, the quantitative analysis so far relied on partly arbitrary assumptions about the phonon dispersion; for example, model dispersions by simple analytical expressions were used in Fig. 5.8 and in Refs. [133, 149, 169]. Because the theoretically determined phonon dispersions of graphite and hence carbon nanotubes were contradictory in many respects, see Sect. 4.2, quantitative predictions of the D mode were difficult to judge. For graphite, however, the experimental data of the phonon dispersion presented in Sect. 4.2 allow now a calculation of double-resonant D -mode scattering without any arbitrary assumptions.

In the literature, calculations of double-resonant scattering often rely on an additional simplification: instead of summing over all intermediate states in Eq. (5.2), *i.e.*, over all possible resonant and non-resonant processes, the double-resonant phonon wave vectors are found by just requiring two real intermediate states, see in particular the graphical methods in Refs. [118, 127, 169, 174]. Some of these apparent double-resonances, however, vanish by destructive interference in a full integration.

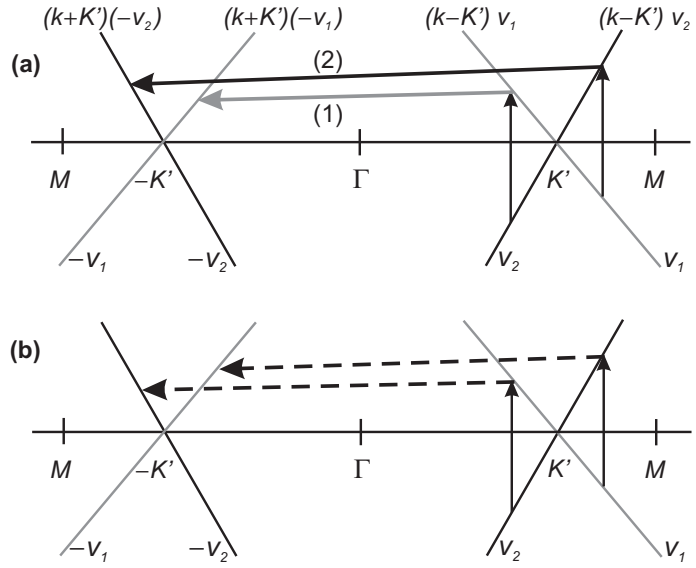
In this section we analyze the interference effects from analytical expressions for D -mode scattering. Moreover, we show that the one-dimensional integration along the high-symmetry lines results in approximately the same double-resonant phonon wave vectors as the integration in the two-dimensional Brillouin zone; thus the tedious integration in two dimensions is not necessary. Finally, we use the experimentally determined phonon dispersion of Sect. 4.2 to explicitly calculate the D -mode line shape and its excitation-energy dependence. The results agree very well with the experiment; in addition, they confirm that the D mode comes from the TO-derived phonon branch, consistent with the selection rules.¹

5.3.1 Double-resonant scattering in one dimension

Here, we derive an analytical expression for the Raman cross section of the D mode in the approximation of linear bands in one dimension. The scattering process for the D mode takes place between two inequivalent K points of the graphite Brillouin zone. At the K point, the electronic bands are approximately linear for transition energies in the visible range of light and cross the Fermi level. Along the Γ - K - M direction the D -mode phonon wave vector is close to twice the K -point vector. In Fig. 5.14 (a) both possibilities for scattering within the same electronic band are shown. v_1 and v_2 are the Fermi velocities, k and q are the wave vectors of the electron and the phonon, respectively.

¹This section is taken from Ref. [134] which is currently under review for publication in Physical Review B.

Figure 5.14: (a) Double-resonant scattering processes leading to the D mode in graphite. The electronic bands are assumed to be linear at the K point with Fermi velocities v_1 and v_2 . The D-mode scattering takes place across the Γ point within the same electronic band. (b) Scattering across the Γ point between two almost parallel bands does not contribute to the double-resonance signal because of destructive interference.



To find the double-resonant phonon wave vectors, we again evaluate Eq. (5.2). From the scattering processes shown in Fig. 5.14 (a) we find

$$\begin{aligned} E_{ai} &= (|k| - K')(v_1 - v_2) - i\gamma & \text{for } |k| < K', \\ E_{ai} &= (-|k| + K')(v_1 - v_2) - i\gamma & \text{for } |k| > K', \end{aligned} \quad (5.5)$$

and

$$\begin{aligned} E_{bi} &= -|k|(v_1 + v_2) + qv_1 - K'(v_1 - v_2) - i\gamma & \text{for } |k| < K', \\ E_{bi} &= -|k|(v_1 + v_2) + qv_2 - K'(v_2 - v_1) - i\gamma & \text{for } |k| > K'. \end{aligned} \quad (5.6)$$

K' denotes the wave vector of the K point. The lifetime broadening γ of the electronic transition energies is taken to be the same. The double-resonant processes (1) and (2) in Fig. 5.14 correspond to $|k| < K'$ and $|k| > K'$, respectively. In the first case, the phonon wave vector is smaller than $2K'$, *i.e.* it is from between K and M, whereas in the second case q is larger than $2K'$ and stems from between K and Γ . From the intermediate state b the electron is scattered to a state c close to state a , therefore $E_{ci} = E_{ai}$.

Assuming $v_1 = -v_2$, we introduce the following expressions analogous to the ones in Sect. 5.1 and Ref. [133]

$$\kappa_1 = \frac{E_l - i\gamma}{2v_1} \quad \text{and} \quad \kappa_2 = \frac{E_l - \hbar\omega_{ph} - i\gamma}{2v_1}. \quad (5.7)$$

We insert the above expressions for the transition energies E_{ai} and E_{bi} into Eq. (5.2) and obtain

$$\begin{aligned}
K_{2f,10} = & \frac{2}{(2v_1)^3} \sum_{k=0}^{K'} \left[\frac{\mathcal{M}}{(\kappa_1 + K' - k)(\kappa_2 + K' - k)} \right. \\
& \times \left. \left(\frac{1}{(\kappa_2 + K' - q/2)} + \frac{1}{(\kappa_1 + K' - q/2)} \right) \right] \\
& + \frac{2}{(2v_1)^3} \sum_{k=K'}^{\infty} \left[\frac{\mathcal{M}}{(\kappa_1 - K' + k)(\kappa_2 - K' + k)} \right. \\
& \times \left. \left(\frac{1}{(\kappa_2 - K' + q/2)} + \frac{1}{(\kappa_1 - K' + q/2)} \right) \right], \tag{5.8}
\end{aligned}$$

where again the transition matrix elements in the numerator are summarized by \mathcal{M} . The sum can be converted into an integral over k . A straightforward evaluation of the integral yields

$$\begin{aligned}
K_{2f,10} = & \frac{\mathcal{M}}{2v_1^2 \hbar \omega_{ph}} \left[\frac{\kappa_1 + \kappa_2 + 2K' - q}{(\kappa_1 + K' - q/2)(\kappa_2 + K' - q/2)} \ln \left(\frac{\kappa_2 + K'}{\kappa_1 + K'} \cdot \frac{\kappa_1}{\kappa_2} \right) \right. \\
& \left. - \frac{\kappa_1 + \kappa_2 - 2K' + q}{(\kappa_1 - K' + q/2)(\kappa_2 - K' + q/2)} \ln \left(\frac{\kappa_2}{\kappa_1} \right) \right]. \tag{5.9}
\end{aligned}$$

Equation (5.9) is evaluated as a function of the phonon wave vector q ; the Raman intensity is at maximum for those q which fulfill the double-resonance condition. The first term in the sum yields double-resonant q vectors smaller $2K'$, *i.e.*, between K - M [process (1) in Fig. 5.14 (a)], whereas the second term yields q vectors between the Γ and K point [process (2) in Fig. 5.14 (a)]. The maximum values of $K_{2f,10}$ are dominated by the terms in the denominators of Eq. (5.9). The double-resonant phonon wave vectors are therefore

$$\begin{aligned}
q_{1,2} &= 2(K' + \kappa_{1,2}) \text{ for } k < K' \\
q_{3,4} &= 2(K' - \kappa_{1,2}) \text{ for } k > K'. \tag{5.10}
\end{aligned}$$

Compared to the expression for scattering between two linear bands given by Eq. (5.3) and derived in Ref. [133], Eq. (5.9) describes double-resonant scattering across the Γ point within the same band, see Sect. 5.3.4. Both processes, (1) and (2) in Fig. 5.14 (a), are included, as well as both time orders of scattering by the phonon and by the defect. This leads to four slightly different double-resonant phonon wave vectors [Eq. (5.10)]. For a calculation of scattering across the K point the expression from Ref. [133] has to be added. In the approximation of zero phonon energy, Eq. (5.10) for the double-resonant phonon wave vectors yields the $q \approx 2k_i$ rule, see Sect. 5.1.

5.3.2 Interference effects

In Eq. (5.9) we explicitly excluded the Raman process, where the electron is scattered across the Γ point between two different, almost parallel bands. In this process [see Fig. 5.14 (b)], at

each excitation energy the double-resonance condition is fulfilled by the phonon exactly at the K point in the case of $v_1 = -v_2$. When summing over all intermediate states these contributions, however, cancel. In addition, in graphite the fully symmetric phonons leading to the D mode are not allowed to couple electronic states of different symmetry.

The Raman cross section for the scattering process shown in Fig. 5.14 (b) can be evaluated in the same way as above, assuming $v_1 = -v_2$:

$$K_{2f,10}^{(b)} = \frac{2\mathcal{M}}{(2v_1)^3} \cdot \frac{f(q, \kappa_1, \kappa_2)}{(\kappa_1 - \kappa_2)[2(\kappa_1 - \kappa_2) + 2K' - q]} \times \frac{1}{(2[\kappa_2 - \kappa_1] + 2K' - q)(2K' - q)}, \quad (5.11)$$

where $f(q, \kappa_1, \kappa_2)$ is a function of q , κ_1 , and κ_2 :

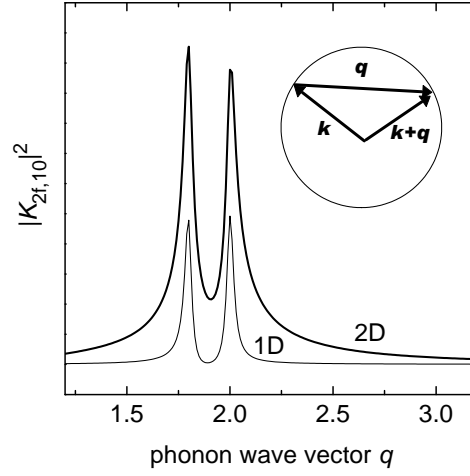
$$f = (2\kappa_2 - 2\kappa_1 + 2K' - q) [-(2K' - q) \ln(-\kappa_1 - K') + (2\kappa_1 - 2\kappa_2 + 2K' - q) \ln(-\kappa_2 - K') + (\kappa_1 - \kappa_2)(\ln 4 - 2 \ln(-2\kappa_2 - q))] + (2\kappa_1 - 2\kappa_2 + 2K' - q) [-(2\kappa_2 - 2\kappa_1 + 2K' - q) \ln(-\kappa_1 - K') + (2K' - q) \ln(-\kappa_2 - K') + (\kappa_1 - \kappa_2)(\ln 4 - 2 \ln(-2\kappa_1 - q))]. \quad (5.12)$$

κ_1 and κ_2 are given by Eq. (5.7). At first sight, this expression seems to have singularities at $q_1^{(b)} = 2K'$ and $q_{2,3}^{(b)} = 2K' \pm 2(\kappa_1 - \kappa_2)$. In particular, $q_1^{(b)} = 2K'$ agrees with what is found graphically from the figure. The numerator [Eq. (5.12)], however, vanishes simultaneously, and we obtain for $q \rightarrow 2K'$

$$\lim_{q \rightarrow 2K'} K_{2f,10}^{(b)} = \frac{2\mathcal{M}}{(2v_1)^3} \cdot \frac{1}{2(\kappa_1 + K')(\kappa_2 + K')}. \quad (5.13)$$

Therefore, the Raman cross section is large if $\kappa_1 = -K'$ or $\kappa_2 = -K'$. For $\gamma = 0$ this condition is equivalent to $E_{1,2} = -2v_1K'$, *i.e.*, a laser energy that is resonant with the optical transition at $k = 0$. Together with the initial condition of $q = 2K'$ we conclude that such a scattering process is not reasonable and does not contribute to a double-resonance signal. The other possibilities result in a similar situation. From $q_{2,3}^{(b)} = 2K' \pm 2(\kappa_1 - \kappa_2) = 2K' \pm \hbar\omega_{ph}/v_1$ it follows that $\hbar\omega_{ph} = \pm(qv_1 - 2K'v_1)$. This condition implies that either the phonon dispersion has the same slope as the electronic bands – in this case the process is “double-resonant” for any q – or, assuming a constant phonon energy, that $q \approx 2K'$. The latter case was already excluded above; the first is not realistic either. Therefore, we do not obtain double-resonant contributions from scattering across the Γ point between the two (almost) parallel electronic bands. Note that this mechanism is analogous to the destructive interference of double-resonant scattering within the same band, if the electron is not scattered across a minimum (or maximum) of the band. In fact, the destructive interference occurs because the electron before and after being scattered belongs to bands with the same slope, in particular with the same *sign* of the slope. These

Figure 5.15: Raman cross section $|K_{2f,10}|^2$ as a function of the phonon wave vector for linear bands in one dimension (lower curve) and for linear bands in two dimensions (upper curve). The inset shows the relation between the vectors \mathbf{k} and \mathbf{q} in Eq. (5.14).



contributions always vanish after summation over all intermediate states, for details see also Ref. [156].

In summary, the contributions from $q = 2K'$ [Fig. 5.14 (b)] cancel as well as those from $q = 0$. Nevertheless, when the integration of the Raman cross section is not performed explicitly but instead the double-resonant q vectors are found graphically, $q = 0$ and $q = 2K'$ contributions are often included by mistake [118, 127, 169, 174]. Neglecting the interference effects thus leads to incorrect results such as the prediction of Raman peaks that are not present in the spectra. In particular, $q = 2K'$ corresponds to a K -point vector; this is included in the literature as a contribution fulfilling $|q - K| = 0$ and being independent of the laser energy [118, 127, 169, 174]. We showed, however, that it is not possible to obtain double-resonant Raman scattering with phonons from exactly the K point.

5.3.3 Double-resonant scattering in two dimensions

Finally, we discuss the differences between the one-dimensional integration above and an integration in two dimensions. As an example we consider again linear bands which cross the Fermi level at $\mathbf{k} = 0$ with a Fermi velocity v_1 . Electrons are scattered across $\mathbf{k} = 0$ from wave vector \mathbf{k} to $\mathbf{k} + \mathbf{q}$, where \mathbf{q} is the phonon wave vector, see inset to Fig. 5.15. In two dimensions, the cross section Eq. (5.2) can be written as an integral over $|\mathbf{k}| = k$ and the angle θ between the vectors \mathbf{k} and \mathbf{q}

$$K_{2f,10}^{2D} = \frac{2\mathcal{M}}{(2v_1)^3} \int_0^\infty dk \int_0^{2\pi} d\theta \left[\frac{1}{(\kappa_1 - k)(\kappa_2 - k)} \times \frac{1}{\kappa_{1,2} - (k + \sqrt{k^2 + q^2 + 2kq \cos \theta})/2} \right] \quad (5.14)$$

with κ_1 and κ_2 as defined in Eq. (5.7). $|K_{2f,10}^{2D}|^2$ is plotted as a function of $|\mathbf{q}|$ in Fig. 5.15 for $\kappa_1 = 1 - i0.01$ and $\kappa_2 = 0.9 - i0.01$ (upper curve). The lower curve is the same scattering process evaluated in one dimension. The positions of the maxima, *i.e.*, the phonon wave vectors that contribute most in the double resonance, are the same in both calculations. The main difference is the much broader range of double-resonant q vectors, if the integration is performed in two dimensions.

Several authors estimated the relative weight of the contributions to the double-resonance signal by considering a “density” of double-resonant phonon wave vectors in two dimensions. [118, 174] Our results, however, show that the main contributions come from scattering across the Γ or K point as in one dimension. Therefore, for finding the double-resonant phonon wave vectors with the strongest Raman signal, the integration in one dimension is sufficient.

5.3.4 Selection rules in graphite

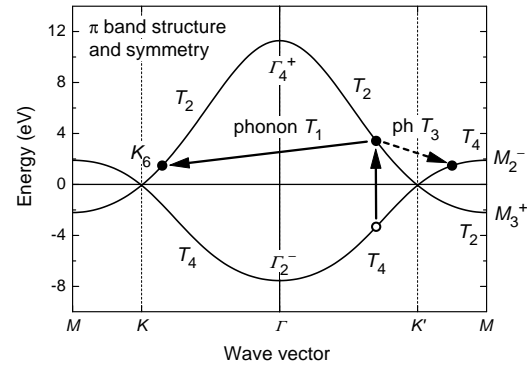
In the preceding section the possible double-resonant Raman processes in graphite were analyzed from a purely mathematical point of view. Here we include the symmetry of electrons and phonons and analyze which of the phonon branches are allowed by selection rules in double-resonant scattering.

Figure 5.16 shows the electronic π and π^* bands in graphene along Γ - K - M ; they are labeled by their symmetry. The bands are calculated from the tight-binding approximation including third-nearest neighbors and fit to *ab-initio* results [78]. Along Γ - K - M , the wave vectors between the high-symmetry points belong to the C_{2v} subgroup of the D_{6h} point group of graphene. The electronic bands have either T_2 or T_4 symmetry (A_2 and B_2 in molecular notation) [67, 150]. The double-resonant process (1) from Fig. 5.14 (a) is shown by solid arrows. The optical transition between T_4 and T_2 requires a photon with Γ_6^- symmetry, *i.e.*, in-plane polarized light. The excited electron is then scattered within the same band by a phonon which must therefore be fully symmetric (T_1). The same selection rules hold for the second process in Fig. 5.14 (a), because the electron-phonon scattering again takes place within the same electronic band.

We assume that the defect-scattering does not change the symmetry of the electron. Even if it did so, the Raman cross section would be small, because the defect would then not couple electronic states of the same symmetry. In the example shown in Fig. 5.16 the third intermediate electronic state is in this case far away from a real electronic state with the correct symmetry. Therefore, the third term in the denominator of the Raman cross section [Eq. (5.2)] is much larger than for an intermediate state very close to a real state.

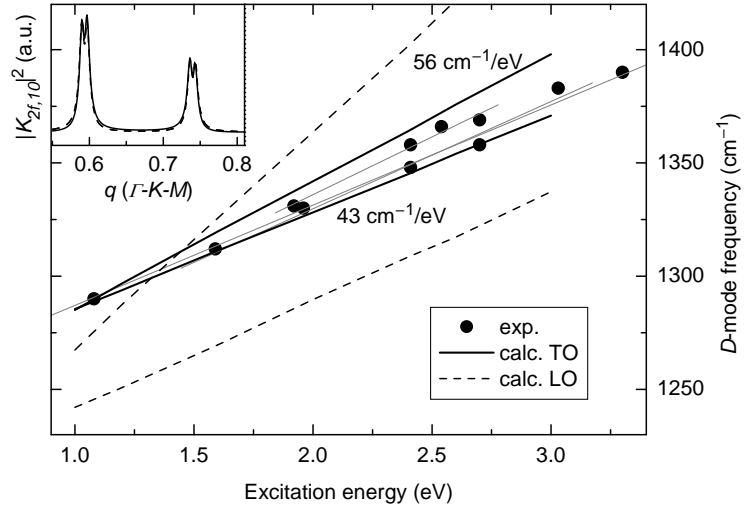
The double-resonant phonon wave vectors are, as shown in the previous section, near $q = 2K'$, which corresponds to near- K point vectors. At the K point of graphene, there are two optical branches, one derived from the longitudinal (LO) and one from the transverse (TO) Γ -

Figure 5.16: Electronic π and π^* bands of graphene along Γ - K - M [134, 150]. The symmetry of the bands is given. The solid arrows denote the same double-resonant process as in Fig. 5.14 (a). Only fully symmetric (T_1) phonons can contribute to the scattering within the same non-degenerate band. The dashed arrow indicates another possibility of double-resonant scattering, involving phonons from near the Γ point with T_3 symmetry.



point phonon, see Chap. 4. Although the eigenvectors at the K point are of mixed longitudinal and transverse character, we call them TO and LO for convenience. At the K point, the TO is the upper branch, which is fully symmetric (K_1 or A_1') in the D_{3h} symmetry group of the K point; the LO (lower branch) is degenerate with the longitudinal acoustic mode (K_5 or E' symmetry). Between the high-symmetry points the TO and the LA phonons have T_1 symmetry; the LO and the in-plane TA phonons belong to the T_3 representation. The out-of-plane modes have T_2 and T_4 symmetry. Since the scattering process in Figs. 5.14 (a) and 5.16 requires T_1 phonons, not all phonon branches contribute to the double-resonance process as would have been expected when neglecting symmetry. Only phonons from the TO or the LA branch are allowed in the double-resonant scattering shown in Fig. 5.14 (a). Because the LA phonons do not have the correct symmetry at the K point nor at the Γ point, we expect from continuity that the TO branch, which is allowed at both K and Γ , leads to the strongest double-resonant Raman signal. In particular, the LO mode is forbidden by symmetry in the D -mode process, in contrast to a variety of models which regarded the LO responsible for the Raman D mode [127, 133, 165, 175]. The reason for the LO being involved in those calculations is that most theoretical predictions [114, 115, 117] of the LO branch provided the characteristics required to match the experimental data of the D mode. These requirements are a frequency at about 1250 cm^{-1} and a local minimum at the K point. The TO phonon was predicted at a too high frequency at the K point, *e.g.*, 1370 cm^{-1} in the *ab-initio* calculation of Ref. [117], see also Sect. 4.2. In force-constants calculations even a local maximum was found for the TO branch at the K point [114], which is incompatible with the positive frequency shift as a function of laser energy. On the other hand, a fully symmetric breathing-like vibration of the carbon hexagons was suggested already by Tuinstra and Koenig [125] and later predicted from a molecular approach based on small aromatic molecules [116, 176–178]. In the following section we show that when using the new experimentally determined phonon dispersion presented in Sect. 4.2, indeed the calculations from the TO phonons match the experimental D -mode spectra very well.

Figure 5.17: D-mode frequency of graphite as a function of laser energy. The dots denote experimental data from Refs. [164–166]. The lines are calculations for defect-induced Raman scattering based on the experimental data for the TO (solid line) and LO (dashed line) phonon branch around the K point. *Inset:* Raman intensity $|K_{2f,10}|^2$ as a function of the phonon wave vector q at $E_i = 2.0$ eV. The solid line is from a calculation of Eq. (5.9); for the dashed line the scattering by K -point phonons was explicitly included. These phonons ($q = 2/3$) do not contribute to the Raman signal.



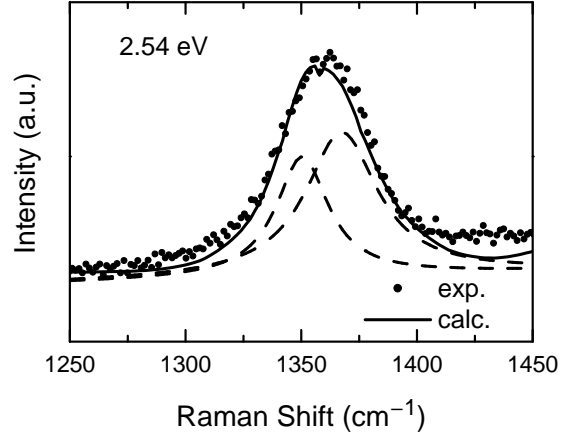
So far we considered scattering of the electrons across the Γ point within the same band. The electron can also be scattered across the K point, *i.e.*, between different bands, leading to further defect-induced modes with wave vectors closer to the Γ point. This is shown in Fig. 5.16 by the dashed arrow. The symmetry of the phonon required for scattering between electronic states with T_2 and T_4 symmetry is T_3 , therefore in this process the LO and TA modes are allowed. The contribution from the defect-scattering step, however, will be rather small because either the third intermediate state is not close to a real state of the same symmetry (if the defect conserves symmetry) or the scattering probability is small (if the defect changes symmetry). Therefore, defect-induced modes from close to the Γ point are predicted to be weaker than the D mode.

5.3.5 Calculation of the D mode in graphite

We now use the analytical expression derived for the Raman cross section, Eq. (5.9) to calculate the D mode of graphite. The average slope of both electron bands at the K point was set to $v_1 = -5.1$ eV \AA from a fit to *ab-initio* calculations of the electronic band structure for transition energies below 3 eV [78]. For the phonons we used a linear fit of the experimental TO frequencies close to the K point.

Figure 5.17 shows the D -mode frequencies calculated from the TO branch (solid lines) together with the experimental values for graphite. The D mode consists of two groups of peaks, one from each side of the K point [process (1) and (2) in Fig. 5.14 (a)]. Within each group, a double-peak structure results from the two different time orders in the scattering process. In Fig. 5.17, the average of the peak positions in each group was taken. The calculated slopes are

Figure 5.18: Raman spectrum of the D mode at $E_l = 2.54$ eV. The experimental spectrum (dots) was taken on a natural graphite flake. The solid line shows a spectrum calculated from the experimental data of the graphite TO phonon [124]; the dashed lines are Lorentzian fits to the calculated spectrum. The calculated Raman intensity is at each phonon energy multiplied by a Lorentzian with a full width of 20 cm^{-1} .



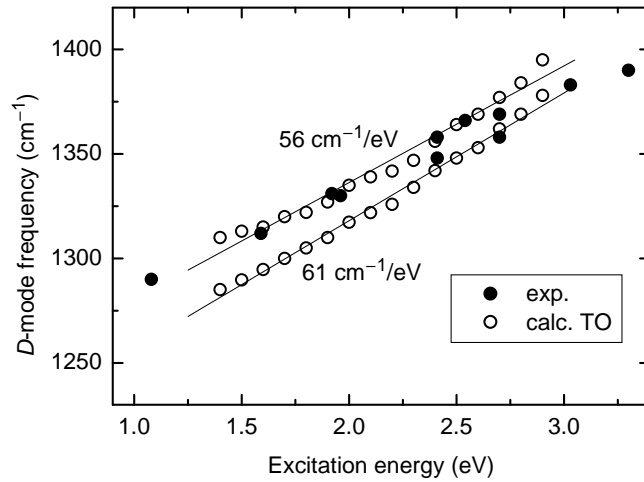
$56\text{ cm}^{-1}/\text{eV}$ and $43\text{ cm}^{-1}/\text{eV}$, where the larger slope stems from phonon wave vectors between K and M and the smaller one from between K and Γ . Compared to the experimental slopes of $44\text{ cm}^{-1}/\text{eV}$ (Ref. [165]), $47\text{ cm}^{-1}/\text{eV}$ (Ref. [164]), and $51\text{ cm}^{-1}/\text{eV}$ (Ref. [166]), we find a very good agreement. In contrast, if we calculate the D mode from the LO data (dashed lines), either the Raman frequencies are by $40 - 50\text{ cm}^{-1}$ lower than the experimental values, or the D mode shift is by a factor of two larger than the experimental shift.

The linear approximation used in Fig. 5.17 allows a quick estimation of the D -mode properties. The rate at which the D mode shifts is proportional to the slope of the phonon dispersion and inversely proportional to the slope of the electron bands. Moreover, the excitation-energy dependence is in this approximation strictly linear.

In the next step we include, again in one dimension, the correct electronic bands from the *ab-initio* calculation and the experimental dispersion of the TO branch. The sum over all intermediate states in Eq. (5.2) is performed numerically. As we showed in the last section, the main difference between the one-dimensional and the two-dimensional integration is a broadening of the range of double-resonant q values, where the positions of the maxima remain the same. Therefore, the possible error when performing the integration in one dimension is not larger than the uncertainties in a two-dimensional integration, where we would have to interpolate the experimental data of the phonon dispersion. Moreover, the asymmetry of the bands with respect to the K point (trigonal warping) is largest along the high-symmetry lines Γ - K - M and is therefore fully taken into account in the present one-dimensional calculation.

In Fig. 5.18 we show a calculated Raman spectrum of the D mode for an excitation energy $E_l = 2.54$ eV. The agreement with the experimental spectrum (dots) is excellent considering that no adjustable parameter is involved except for an overall scaling. The D -mode peak is not a single Lorentzian but has a complex line shape due to the double-resonance processes

Figure 5.19: *D*-mode frequency of graphite as a function of laser energy, calculated from the experimentally determined TO branch. The upper and lower frequencies come from phonons between *K*-*M* and between Γ -*K*, respectively. The dots denote experimental data from Refs. [164–166].



contributing to the signal. The individual contributions, however, are not resolved and a fit by two Lorentzians is appropriate. Each of the two peaks roughly corresponds to phonons from one particular side of the *K* point as discussed above. The good agreement in line shape was obtained by using a phonon linewidth of 20 cm^{-1} in the calculation. This large linewidth is consistent with the broadened range of double-resonant phonon wave vectors that we expect for the integration in two dimensions.

The *D*-mode frequency as a function of excitation energy from the same calculation as in Fig. 5.18 is shown in Fig. 5.19. The frequencies were again found from a fit by two Lorentzians to the calculated spectra. The upper (lower) frequency stems from the phonon branch between *K* and *M* (Γ and *K*). The *D* mode shifts at a rate of $56 \text{ cm}^{-1}/\text{eV}$ and $61 \text{ cm}^{-1}/\text{eV}$. Because of the non-linear electronic bands and phonon dispersion, the shift is only approximately linear. Our calculations again confirm that the *D* mode comes from the TO-derived phonon branch of graphite [116, 176–178]. From the strong relation between graphite and carbon nanotubes we expect that this holds for carbon nanotubes as well.

5.4 The high-energy modes

The Raman spectrum of the high-energy modes (see Figs. 5.1 and 5.2) is, like the radial breathing mode, specific to single-walled nanotubes. It consists of several close-by peaks with two dominant ones at approximately 1595 and 1570 cm^{-1} . The minimum between them is at almost the same frequency as the graphite E_{2g} mode (1580 cm^{-1}). Their full width at half maximum ranges from 15 to 30 cm^{-1} ; the line shape is not a simple Lorentzian or sum of Lorentzians, see Fig. 5.20. In fact, Fig. 5.2 shows that the line shape can vary dramatically, in particular, the peaks below 1580 cm^{-1} can increase in intensity and become even further broad-

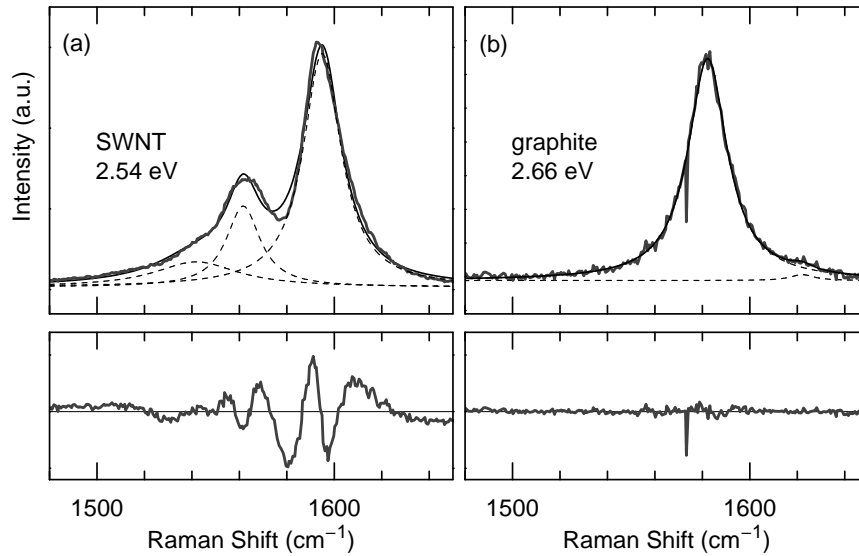
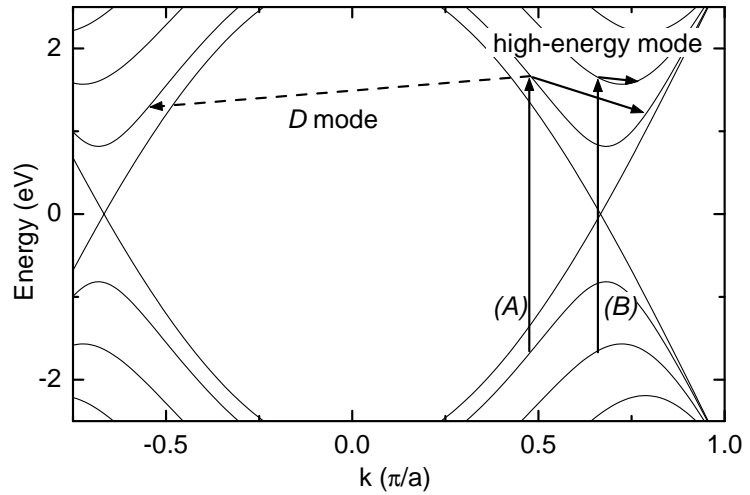


Figure 5.20: (a) High-energy modes of bundled carbon nanotubes (gray thick line). The lineshape cannot exactly be fit by just a sum of Lorentzians (black thin line and dashed lines). In particular, the position of the minimum between the two strongest peaks is not reproduced correctly by the fit; on the high-energy side the slopes of the experimental spectrum and the fit do not match. (b) The G mode in graphite is a single Lorentzian; the small peak at 1620 cm^{-1} comes from the overbending in the LO phonon branch and is due to double-resonant scattering. The bottom panels show the difference between the measured spectra and the fits. The deviations for the nanotube spectrum is clearly seen; the difference between the spectrum of graphite and the fit is almost zero.

ened. This characteristic peak structure allows, combined with the RBM, the identification of single-walled carbon nanotubes in a sample. From polarization-dependent Raman measurements it is known that the main contributions to the signal come from fully symmetric modes ($A_{1(g)}$) [179–182]; moreover, the optical absorption is strongest for z -polarized light, where z is the direction of the tube axis [84, 183]. Thus the Raman spectrum is predominantly observed in (z, z) configuration.

In laser-energy-dependent Raman experiments, additional information on the electronic properties of the sample can be obtained. If the laser energy is scanned across the band gap of a semiconductor, the Raman intensity, as a function of excitation energy, reveals transition energies, the lifetime of the electronic states, and properties of the electron–phonon interaction [156, 184, 185]. Another example of laser-energy-dependent Raman scattering was shown for the D mode in Sect. 5.2 where – in addition to the electronic properties – the phonon dispersion is probed. Although resonance profiles of the radial breathing mode and the high-energy modes in nanotubes were investigated by several authors [152, 186, 187], the aim of changing excitation energy was often a different one for carbon nanotubes. The common interpretation so far assumed that the laser energy determines which of the tubes in a sample are resonantly excited and contribute exclusively to the Raman signal [148, 155, 188]. Consequently, the slight

Figure 5.21: Double-resonant scattering process for the high-energy mode in the band structure of an armchair nanotube. For comparison, the D -mode scattering is shown by the dashed arrow. Processes (A) and (B) at the same laser energy are both double resonant. Process (B) leads to the largest Raman peaks because it involves electrons with a large density of states. Process (A) gives rise to the weaker peak structure on the low-energy side of the Raman high-energy mode.



variation of the HEM frequencies (see Fig. 5.2) with excitation energy was usually attributed to a weak diameter dependence of the optical Raman-active modes [155, 189], which is predicted by force-constants and *ab-initio* calculations [136, 190, 191]. In this interpretation, only those tubes that have a singularity in the electronic joint density of states *exactly* at the laser energy contribute to the Raman signal. Many diameter-dependent studies of the vibrational properties of carbon nanotubes are based on this assumption, *i.e.*, the laser energy is varied instead of the tube diameter. In the literature of carbon nanotubes, the term “single resonance” or “photo-selective scattering” is often taken to stand for the diameter selection.

We will show here that the frequency shift of the high-energy mode with varying excitation energy is not necessarily due to diameter-selective excitation of the tubes. For example, this picture cannot explain how the rather complex peak structure arises from just the two fully-symmetric phonon modes that are allowed in carbon nanotubes for (z, z) -scattering, nor does it give a reason for the amplitude ratio of the HEM peaks. In contrast, the double-resonance picture gives a natural explanation for these peculiar properties of the HEM. In this picture, as for the D mode, the Raman frequency does not change because a different tube is excited, but because a different phonon of the same tube is enhanced. The scattering process is analogous to the one explained for the D mode in Sect. 5.2, but the excited electron is now scattered by a phonon with relatively small momentum across the conduction-band minimum (Fig. 5.21). Unlike in graphite (Sect. 5.3.4), scattering across the conduction-band minimum in carbon nanotubes requires the same symmetry of the phonon as the D -mode scattering across the Γ point. Therefore, if the D mode is caused by a double-resonant process, there is no reason for the HEM not to be of the same origin.

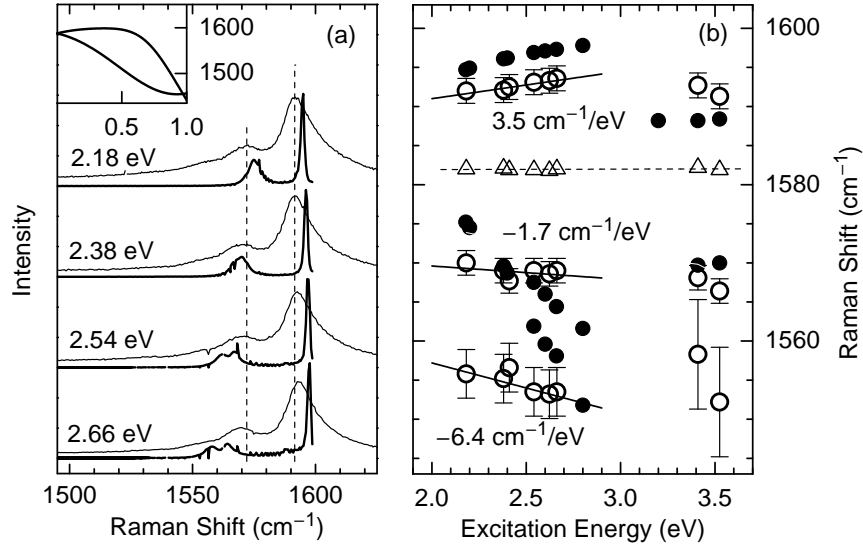
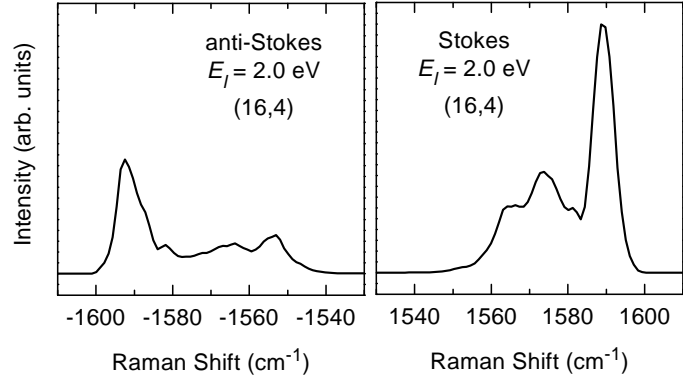


Figure 5.22: (a) Experimental (upper curves) and calculated (lower curves) Raman spectra of single-walled carbon nanotubes. The calculations were performed for the (15,6) tube according to Eq. (5.2). The model phonon dispersion shown in the inset and the nearest-neighbor tight-binding approximation for the electrons were used, see Ref. [43]. (b) High-energy mode as a function of laser energy. The open circles are experimental data from bundles of single-walled nanotubes; the open triangles are from graphite. Values calculated for double-resonant scattering in the (15,6) tube are given by closed symbols. The frequencies of the peak at $\approx 1590 \text{ cm}^{-1}$ increase with laser energy, whereas the lower peaks decrease in frequency. The graphite frequency is constant.

The double-resonant process leading to the high-energy modes is shown in Fig. 5.21 for an armchair tube. If the polarization of the incoming and outgoing light is parallel to the tube axis [(z,z) scattering geometry], the phonon must conserve all quantum numbers, in particular, $m_{ph} = 0$ (or $\tilde{m}_{ph} = 0$ for chiral tubes), see Table 5.1. Therefore, the electron can be scattered by a fully symmetric phonon within the same band across the minimum. With increasing excitation energy the selected phonon wave vector increases, resulting in a frequency shift of the observed Raman mode. As in the example of linear bands (Sect. 5.1), scattering from the left or from the right of the minimum leads to slightly different phonon wave vectors. Furthermore, at the same excitation energy, the resonant optical transition might be provided by two different electronic bands. This is indicated by (A) and (B) in Fig. 5.21. Process (B) dominates the spectrum because the density of states of the involved electrons is larger than for process (A).

Experimentally, a systematic shift of the high-energy peaks is indeed observed. In Fig. 5.22 (a) we show the Raman spectra of bundled single-walled nanotubes recorded at different excitation energies (upper curves). The dashed lines indicate the peak position at $E_l = 2.18 \text{ eV}$. The upper peak shows a systematic upshift, whereas the lower peaks shift to smaller frequencies, see Fig. 5.22 (b). We calculated the Raman spectra of the (15,6) tube by double-resonant

Figure 5.23: Stokes and anti-Stokes HEM at the same laser energy calculated for the (16,4) tube. The phonon dispersion was calculated from the force-constants approach described in Ref. [135] (Sect. 4.3.2); the electronic band structure was found from the tight-binding approximation including third-nearest neighbors, see Chap. 3. The frequencies and the line shape are different in Stokes and anti-Stokes scattering due to different double-resonance conditions. Only the two $\tilde{m} = 0$ phonon bands are included in the calculation.



scattering using a model dispersion for the phonons [inset to Fig. 5.22 (a)]. The agreement of the calculated spectra (lower curves) with the experimental ones is very good, in particular the amplitude ratio between the main peaks, and the presence of a minimum close to the graphite E_{2g} frequency. Moreover, we obtain positive and negative shifts with excitation energy, as in the experiment. The calculated peak positions are shown in Fig. 5.22 (b) by closed symbols. As long as the dominant scattering process occurs in the same electronic band for each laser energy, the double-resonant phonon wave vector continuously increases. Therefore, the upper peak follows the overbending of the LO branch, and the lower peaks decrease in frequency according to the negative slope of the TO dispersion. The upper peak has the largest amplitude because the LO phonons contribute with a large density of states to the double-resonant Raman cross section [Eq. (5.2)]. The presence of several peaks on the low-energy side is due to close-by electronic bands that contribute with different intensity in the double-resonance process. If at a particular laser energy the next higher electronic band is reached, this process, such as (B) in Fig. 5.21, will dominate the Raman spectrum. In this case the phonon wave vectors are again small, and the strongest Raman peaks are again close to the Γ -point frequencies. This “jump” is seen in Fig. 5.22 (b) for laser energies above 3 eV. Note that the frequency of the graphite E_{2g} mode (triangles) does not vary with excitation energy as it is not a defect-induced, double-resonant mode.

The double resonance predicts, as outlined in Sect. 5.1, different Stokes and anti-Stokes spectra for the high-energy modes. In agreement with this prediction, differences between Stokes- and anti-Stokes spectra were observed by several authors [192, 193]. In Fig. 5.23 we show Stokes and anti-Stokes spectra of the (16,4) tube calculated for double-resonant Raman scattering. Since the double-resonance conditions are slightly different in Stokes and anti-Stokes scattering, the resulting Raman modes differ in shape and frequency. Although only the two $\tilde{m} = 0$ phonon bands are included in the calculation, consistent with the predominant A_1 symmetry of the Raman modes, the calculated spectrum exhibits a complex peak structure.

Double resonance	Single resonance
shift of the Raman peaks due to defect-induced double resonance	shift of the Raman peaks due to diameter & chirality selective single resonance
↓	↓
Phonons with large wave vectors are excited	only Γ -point phonon modes are excited
↓	↓
Raman spectra resemble the phonon dispersion	Raman spectra resemble a tube diameter & chirality distribution
↓	↓
Raman peaks shift with laser energy in an isolated tube	Raman peaks do not shift in an isolated tube

Table 5.2: Different implications of defect-induced, double-resonant scattering and diameter-selective single-resonant scattering.

For Raman experiments performed on bulk samples containing unoriented bundles of single-walled tubes with different chirality and large diameter distribution, the interpretation of the Raman spectra is complex and sometimes leads to ambiguous conclusions. The Raman signal is averaged over many tubes with different properties that are not resolved. Since for tube ensembles the predictions of the single-resonance and the double-resonance model are similar, it is difficult to distinguish them experimentally. For example, both models allow a variation of the HEM frequencies, although for different reasons. The single-resonance explained the difference between Stokes- and anti-Stokes spectra by slightly different resonance windows for Stokes and anti-Stokes scattering, where semiconducting tubes were selected in Stokes and metallic tubes in anti-Stokes spectra, or *vice versa* [192]. To judge whether different phonons from the same tube (double-resonance) or the same phonons from different tubes (single resonance) determine the Raman spectra, we need to perform Raman experiments on the same individual tube.

5.4.1 Experiments on individual nanotubes

Experiments on individual tube became recently feasible by dispersing very small bundles or even isolated tubes onto a substrate [34, 148, 153, 173, 194]. In these experiments, the chirality of the investigated tube is still unknown. But now the Raman spectrum reflects the properties of just one individual tube. If position and orientation of the tube are known, polarized Raman measurements can be performed within a given scattering geometry [34], see Sect. 4.3.1. Moreover, the *same* tube can be studied under different experimental conditions like varying

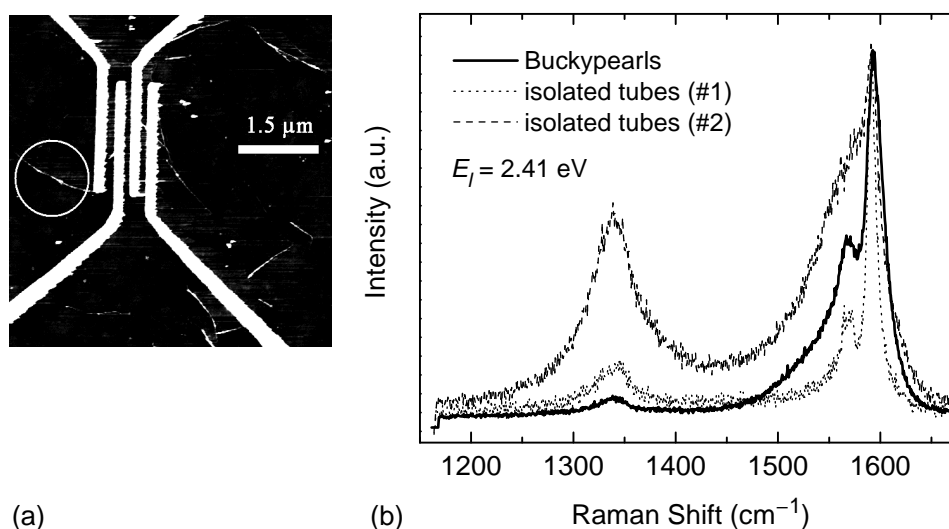


Figure 5.24: (a) Atomic force microscopy (AFM) image of individual nanotubes or thin bundles on a SiO_2 substrate. The four vertical electrodes are used as a marker. The white circle indicates the investigated tube. By averaging cross sections along the tube axis a value of 2.8 nm was obtained, indicating the presence of at most 2–3 tubes. From Ref. [173]. (b) Raman spectra at $E_l = 2.41 \text{ eV}$ from the same type of sample, where the solid line is measured on the bulk material (buckypearls). The dotted and dashed lines are from two different spots on the substrate with 1–2 tubes or very thin tube bundles within the focus.

laser wavelength. Any dependence of the Raman spectra such as frequency, line shape, or intensity on the excitation energy is then a property of the tube itself. To collect a Raman signal from only one or very few nanotubes, a conventional micro-Raman setup [195] with a $\times 100$ objective is sufficient. The distance between the tubes on the substrate must be larger than the size of the laser spot ($\sim 1 - 2 \mu\text{m}$) to ensure that only one tube is within the laser focus. The laser power on the sample is kept below $\sim 100 \mu\text{W}$ to prevent the nanotubes from being damaged. The position of the tube relative to some marker structures on the substrate can be determined by scanning force microscopy.

Figure 5.24 shows to the left a typical atomic-force microscopy (AFM) image of isolated tubes or very thin bundles on a Si/SiO_2 substrate. The position of tubes close to the marker, here a gold electrode, can be found with the optical microscope of the Raman setup. The sample was positioned such that the polarization of the incoming and detected light is approximately parallel to the tube axis. The Raman signal disappeared when the polarization of the incoming light was changed or when the sample was moved by $0.5 - 2 \mu\text{m}$ with respect to the laser spot. To the right of Fig. 5.24 we show the Raman spectra of isolated tubes or very thin bundles from the same type of sample. It is remarkable that the Raman signal of a single molecule is strong enough to be detected without further enhancement. The overall line shape is similar to that in bundles of single-walled tubes (solid line), although one could expect that the lines were much

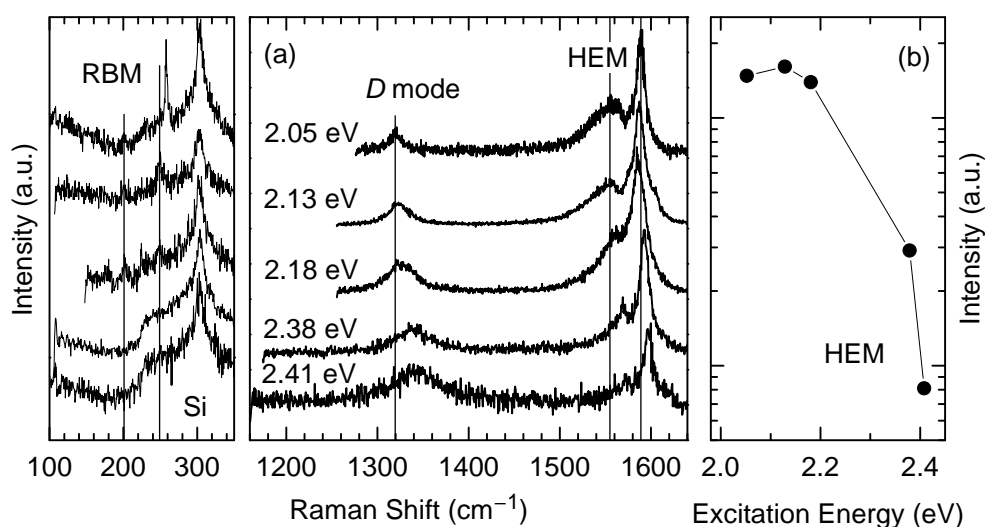


Figure 5.25: (a) Raman spectra from the same individual tube at different laser energies. The vertical lines indicate the peak positions at the lowest laser energy. The RBM signal is weak but comparable with the Si second-order acoustic modes at 300 cm^{-1} (left). The *D* mode clearly shifts, see also Sect. 5.2; the HEM frequencies and line shape vary as well. At lower excitation energy, the spectrum is metallic-like, whereas at larger excitation energy the spectrum resembles a semiconducting spectrum. (b) Intensity of the HEM as a function of laser energy. The intensity was found by taking the area of the HEM peaks. The intensity is normalized with respect to laser power, spectrometer sensitivity and integration time.

narrower or at least of Lorentzian line shape for a single tube. Depending on the position of the laser focus, *i.e.*, depending on the particular tube, the Raman spectrum exhibits a “metallic” (dashed line) or a “semiconducting” line shape (dotted line). Several authors performed experiments also on samples where the position and orientation of the isolated tubes were not known but only their average density on the substrate. The analysis of these experiments is then, as for bulk samples, based on assumptions on the relation between RBM frequency and diameter, and on diameter-selective scattering [45, 188].

In Fig. 5.25 (a) we show the Raman spectrum recorded at different laser energies from the nanotube indicated in Fig. 5.24. Both line shape and frequency of the high-energy modes clearly depend on laser energy. The spectrum at 2.05 eV exhibits a strong broadening and a high intensity at $\approx 1550\text{ cm}^{-1}$. It resembles a metallic spectrum, which, in general, is expected to be weaker than in bundles [153]. With increasing laser energy, the peak at $\approx 1550\text{ cm}^{-1}$ becomes weaker in intensity and shifts towards higher frequencies. The frequency of the upper peak at $\approx 1590\text{ cm}^{-1}$ first decreases and then increases again. The spectra recorded at excitation energies above 2.18 eV resemble typical semiconducting spectra. This indicates that the metallic or semiconducting appearance of the Raman spectrum is not an intrinsic property of the tube but depends also on the excitation energy. The signal of the radial breathing mode was weak in

general and overlapped with the second-order acoustic spectrum of Si (Fig. 5.25 (a), left). At laser energies between 2.05 eV and 2.18 eV, weak RBM peaks at 200 cm^{-1} and at 249 cm^{-1} can be found; the latter is slightly upshifted at 2.05 eV. At higher laser energies the RBM could not be detected. Nevertheless, since the detected RBM peaks do not show a significant variation, we assume that the Raman signal comes from the same tube (or at most two tubes) at each of the five laser energies in Fig. 5.25 (a).

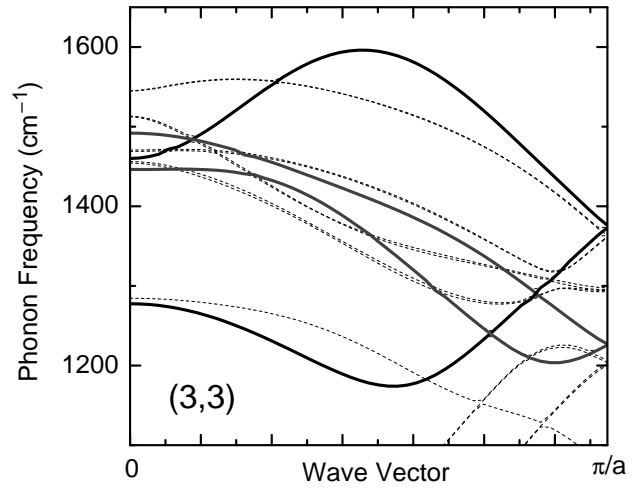
The marked excitation-energy dependence of the high-energy modes in an individual nanotube provides strong support for the double-resonance model. The single-resonance picture, in contrast, cannot explain the results shown in Fig. 5.25, unless it is assumed that the investigated tube in fact consisted of five tubes, where at each excitation energy one of them is resonantly excited. This is rather unlikely, in particular in view of the almost constant RBM frequencies. Moreover, in the diameter-selective model a larger excitation energy would select a tube with smaller diameter. Consequently one should expect a continuous decrease of the frequencies of the lower peak, in contrast to the experimental results in Fig. 5.25 (a). The intensity of the high-energy modes [Fig. 5.25 (b)] decreases continuously with increasing laser energy. This indicates that the smallest excitation energy is closest to a singularity in the electronic joint density of states. As the laser energy increases, the double-resonance process moves away from the conduction-band minimum (see Fig. 5.21), leading to a weaker Raman signal by larger phonon wave vectors. Again this result is fully in accordance with the double-resonance model, whereas the single-resonance model – assuming the resonant excitation of five different tubes – would expect nearly constant Raman intensities. *Vice versa*, a continuous decrease in intensity would imply constant Raman frequencies (excitation of the same tube) in the single-resonance picture.

In summary, Raman measurements of the same isolated nanotube demonstrated that the high-energy spectra depend on the laser energy for an individual tube. This provides a clear evidence for the double-resonant nature of the high-energy modes in carbon nanotubes, solving a major controversy on the interpretation of the spectra.

5.4.2 Metallic nanotubes

In this section we will consider in more detail the origin of the metallic and semiconducting appearance of the high-energy modes. In the conventional interpretation, the spectrum at $E_l = 2.05\text{ eV}$ in Fig. 5.25 (a) indicates the presence of a metallic tube, whereas a spectrum like the one at $E_l = 2.38\text{ eV}$ would be assigned to a semiconducting tube. The results in Fig. 5.25 (a) show, however, a continuous transition from metallic- to semiconducting-like Raman spectra in the same nanotube. Again, this variation of the line shape is understood by double-resonant scattering.

Figure 5.26: Phonon dispersion relation of the (3,3) tube from *ab-initio* calculations. The solid lines indicate the $m = 0$ and $m = 3$ branches of the LO (black) and the TO phonon (gray). At the Γ point, the LO phonon drops below the TO frequency, giving rise to a pronounced overbending. The shape of the bands has probably to be revised in detail, since the phonon frequencies are actually determined only at those points that are compatible with the supercell used in the calculation, see also Ref. [124]. From Machón *et al.* [139].



Let us assume that the isolated tube in Fig. 5.25 (a) is metallic, as predicted from its line shape at $E_l = 2.05$ eV. The comparatively large intensity at this energy [Fig. 5.25 (b)] suggests that the laser energy is close to a singularity in the electronic joint density of states, *i.e.*, the optical transitions occur close to the conduction band minimum. Consequently, the double-resonant phonon wave vector is small, and increases with increasing laser energy. The observed phonon is thus close to the Γ point at $E_l = 2.05$ eV. In metallic tubes, the LO $m = 0$ phonon frequency at the Γ point is significantly softened because of a strong electron-phonon coupling, as first predicted by Dubay *et al.* [191] from *ab-initio* calculations. This softening leads to the strong Raman signal on the low-energy side of the HEM peak in metallic tubes, as observed in the upper spectrum in Fig. 5.25 (a).

Inside the Brillouin zone, the LO branch exhibits a pronounced overbending, see Fig. 5.26, and then continues similarly to what is expected for semiconducting tubes. In achiral tubes, the $m = 0$ LO and TO modes cross near the Γ point, whereas in chiral tubes they exhibit an anticrossing because they have the same symmetry. With increasing laser energy and hence increasing double-resonant phonon wave vector, the Raman peaks follow the phonon dispersion. They first shift towards each other, and then the splitting increases again. This is seen in Fig. 5.27 (a), where the HEM frequencies as a function of the laser energy are plotted from the Raman spectra in Fig. 5.25. The solid and dashed lines are a guide to the eye to illustrate the resemblance to the phonon dispersion for a chiral and an achiral tube, respectively. As an example, we calculated the HEM frequencies for an (8,8) tube, see Fig. 5.27 (b), using a phonon dispersion that we modified according to the predicted drop of the LO frequency. The qualitative agreement is very good: the splitting between the HEM peaks first decreases and then increases again after the crossing of the LO and TO branch. The bottom axis emphasizes the correspondence to the phonon dispersion, where the average values of the double-resonant

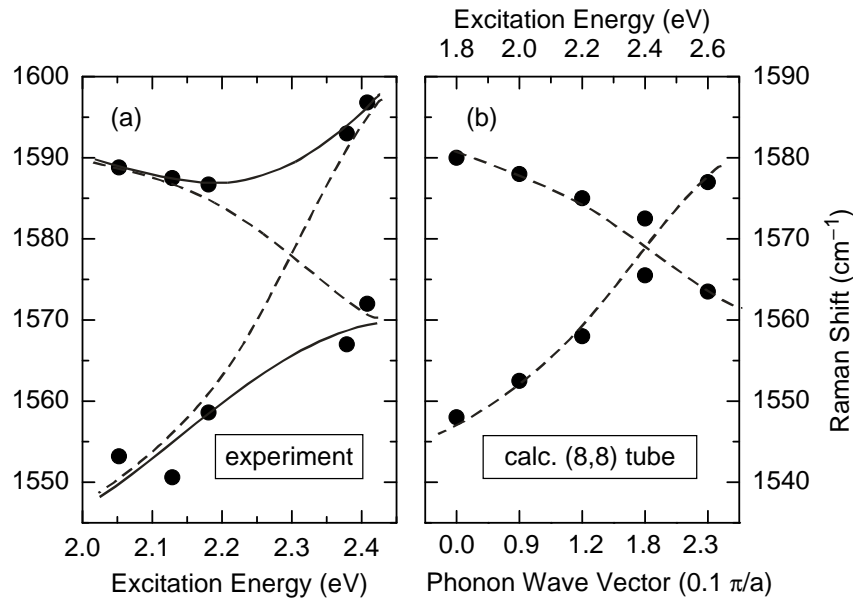


Figure 5.27: (a) High-energy mode frequencies as a function of laser energy, measured on an isolated tube; (b) calculation for the (8,8) tube. The solid and dashed lines are guides to the eye. They illustrate the resemblance of the HEM dependence on laser energy to the phonon dispersion of a metallic tube. In (b), the bottom axis denotes the calculated double-resonant phonon wave vector; the axis is not linear. The phonon dispersion used in the calculation is a model dispersion adapted to a metallic tube. From Ref. [173].

phonon wave vectors are given. Note that the relation between the laser energy and the double-resonant phonon wave vectors is not linear because of the non-linear electron and phonon bands. We do not expect an exact quantitative agreement of the experimental and the calculated frequencies because the calculation depends on the chirality and diameter of the tube and on the approximations for the electron and phonon dispersions.

Besides the generally lower frequencies in metallic nanotubes as discussed above, a second mechanism gives rise to the peculiar metallic line shape. Kempa [196] and Jiang *et al.* [153] proposed that a strong coupling of phonon and plasmon modes leads to the downshift and line shape of the metallic Raman spectra. They showed that a non-zero phonon wave vector is required for this coupling. Therefore, defects must be present in the tube, if the metallic line shape is to be observed, in accordance with the double-resonance model. The required phonon momentum decreases in nanotube bundles with bundle thickness, thus the metallic line shape is weaker in isolated tubes than in bundles.

In summary, the Raman spectra of metallic tubes appear both metallic- and semiconducting-like, depending on the laser energy compared to the energy of the van-Hove singularity. If the Raman spectrum is metallic, however, it *does* indicate a metallic tube. Only in metallic tubes, the strong broadening of the mode by a phonon-plasmon coupling and the softening of the

LO phonon occur, giving rise to the peak on the low-energy side of the HEM. Therefore, Raman scattering provides an experimentally fast and simple method for the determination of the metallic character of a tube. For example, metallic nanotubes that had been separated by an electric field from semiconducting tubes [42] were characterized by Raman scattering instead of transport measurements, which would have been much more laborious.

5.4.3 Defects

The interpretation of the above results by double-resonant Raman scattering implies that defects are present in the sample, relaxing the translation periodicity and hence the conservation of quasi-momentum. These defects could be structural defects such as pentagon-heptagon pairs, vacancies, kinks or the finite length of the tube. Furthermore, defects can be formed by impurities such as alkali metals that intercalate into the nanotubes [197–199] or substitutional boron and nitrogen atoms [200–202]. Studies of defects and their interaction with the electronic states in a nanotube are mostly performed with respect to the transport properties of metallic tubes, see for instance Ref. [203].

As for the D mode in graphite, the strength of the double-resonant Raman modes in carbon nanotubes is expected to depend on the defect concentration in the sample. This will constitute further experimental support of the double-resonance model. Frequently it is assumed that the intensity of the D mode with respect to the HEM intensity, D/HEM , indicates the defect concentration. For example, the purity of nanotubes produced under different growth conditions is often estimated from the intensity ratio D/HEM [204–207]. Raman studies, where the defect concentration in carbon nanotubes was systematically varied to validate this assumption, are rare [204, 208]. Instead, this assumption is rather based on analogous investigations of the intensity ratio D/G in graphite samples with varying crystallite size [125]. On the other hand, if in carbon nanotubes the HEM itself is a defect-induced mode, the intensity ratio D/HEM should be used with great caution. We will show here that the intensity of both the D mode and the HEM in carbon nanotubes depends on the concentration of defects in the sample.

We studied boron-doped multiwall carbon nanotubes with varying boron content [209].⁵ Figure 5.28 (a) shows the Raman spectra of such multiwall nanotubes at different boron concentrations in the growth mix. The intensity of the D mode is roughly constant in the doped sample, whereas the absolute intensities of the HEM and the D^* mode decrease with the defect concentration. The intensity decrease of the D^* mode is more rapid than that of the HEM.

In general, disorder reduces the crystal symmetry, which leads to a softening of the $q \approx 0$ rule for first-order scattering or the $q_1 \pm q_2 \approx 0$ rule in second order and results in a broadening of the Raman peaks [210, 211]. Furthermore, the absolute Raman intensities can change

⁵The sample and Raman measurements were made in Clemson; the interpretation in Berlin.

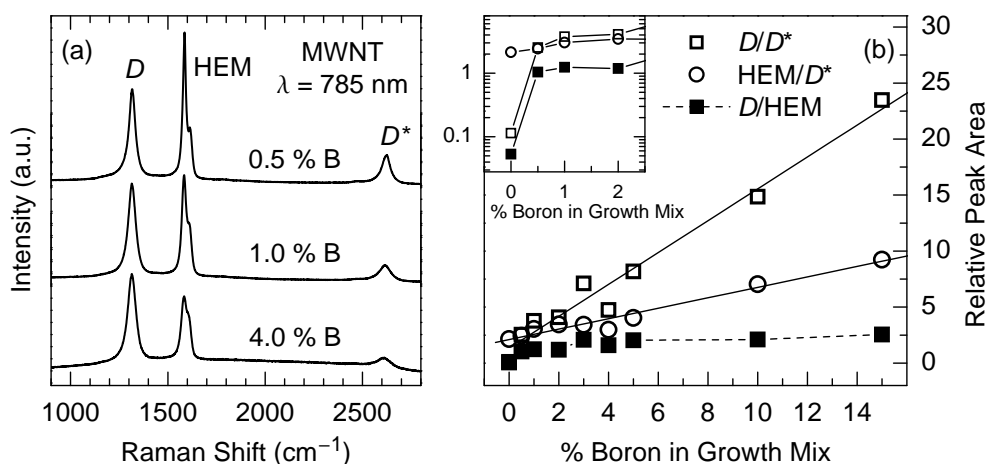


Figure 5.28: (a) Raman spectra of boron-doped multiwall carbon nanotubes with different boron concentrations in the growth mix. The spectra are normalized with respect to laser power and integration time. (b) Relative Raman intensities of the D mode, HEM and the second-order mode D^* as a function of the nominal boron concentration. Closed symbols indicate the intensity ratio D/HEM ; open squares and circles indicate the intensity of the D mode and the HEM, respectively, normalized to the D^* mode intensity. The intensity is found by fitting each Raman mode separately by one or two Lorentzians and taking the total peak area. The solid lines are linear fits to the data; the dashed line is a guide to the eye. When normalized to a second-order mode, both the D mode and the HEM increase in intensity with the defect concentration. *Inset:* semi-logarithmic plot of the region of low boron concentration.

because of a different absorption cross section in the disordered sample. These mechanisms have a similar influence on first and second-order intensities. In addition, particular modes in the first-order spectrum can be selectively enhanced by disorder. First, Γ -point phonons that are forbidden by symmetry in the perfect crystal can become allowed and appear in the Raman spectra. Second, because the $q \approx 0$ rule does not apply any longer, particular phonon modes from inside the Brillouin zone can contribute with a strong Raman signal in a double resonance process, as discussed above. Thus a large defect concentration might lead to an increased scattering cross section for the defect-induced, double-resonant Raman mode in the first-order spectra of carbon nanotubes. The second-order signal in carbon nanotubes, on the other hand, is caused by a double-resonant process independently of the presence of defects, because phonons from throughout the Brillouin zone are allowed in second-order scattering. Therefore, by normalizing the first-order intensities with respect to the second-order overtone mode D^* we can distinguish between first-order modes that are defect-induced and enhanced through a double resonance and Γ -point modes that are not enhanced by defects.

In Fig. 5.28 (b) the relative intensities of the Raman peaks as a function of the nominal boron concentration are shown. Open symbols indicate the intensity of the D mode and the HEM, normalized with respect to the second-order overtone D^* . As expected for a disorder-induced mode, the relative intensity of the D mode increases with increasing density of defects.

Between 0% and 0.5% nominal boron concentration, the intensity ratio D/D^* increases rapidly [by a factor of 25, see inset of Fig. 5.28 (b)]; for higher concentrations the increase is weaker. The relative intensity of the high-energy mode increases as well with increasing nominal boron concentration, although at a somewhat lower rate than the D mode. This behavior is contrary to what would be expected for a first-order, Raman-allowed Γ -point mode, whose intensity should exhibit the same dependence on the defect concentration as the second-order overtone modes. Therefore, the increasing intensity ratio HEM/D^* indicates that the high-energy mode in carbon nanotubes is disorder-induced as well, further supporting the double-resonance model.

The intensity ratio D/HEM is shown by the closed squares in Fig. 5.28 (b). Like the ratio D/D^* , it increases, but at a rather small rate above 3% nominal boron concentration. An increasing or decreasing intensity ratio D/HEM thus gives still a tendency for a higher or lower density of defects in the sample. Note however, that a small D/HEM ratio can also indicate an $\mathcal{R} = 1$ tube (Sect. 5.2), irrespectively of the purity of the sample. Since the intensity of the high-energy mode itself depends on the concentration of defects in the sample it is not appropriate as a basis for normalization. Instead, we can use both intensity ratios, D/D^* and HEM/D^* , to find a correlation between the boron concentration and the Raman intensities. We approximate the relative intensities by linear functions [Fig. 5.28 (b)] and obtain $I^{D/D^*} = 1.3 + x \cdot 1.4(\% \text{conc.})^{-1}$ between 1% and 15% and $I^{\text{HEM}/D^*} = 2.1 + x \cdot 0.47(\% \text{conc.})^{-1}$ between 0% and 15% B concentration, where x is the nominal boron concentration. Note that at this point we do not know the actual boron concentration but only the nominal concentration as given by the growth parameters.

If both the D mode and the high-energy mode result from a defect-induced Raman process, the question arises, why the increase in relative intensity HEM/D^* is much weaker (at least at the lowest doping levels) than the increase of D/D^* [inset to Fig. 5.28 (b)]. This can be easily understood from the different phonon wave vectors that give rise to the D and high-energy mode, respectively. As outlined in Sect. 5.4 the HEM phonon wave vectors are rather close to the Γ point compared to those of the D mode. Thus even a low defect concentration leads to a weak spatial confinement of the high-energy phonon modes. The corresponding distribution of phonon wave vectors is large enough to allow the double-resonant, near- Γ point modes to contribute to the scattering process. For example, let the defect concentration be 0.1%, i.e., there is one defect per 1000 carbon atoms. In the (10,10) tube this results in one defect per 25 unit cells or a mean distance between the defects of $25a_0$, where a_0 is the length of the graphene lattice vectors. The wave vector corresponding to the mean distance between the defects is $k = 2\pi/(25a_0) = 0.08\pi/a_0$, which is already large compared with the wave vector of visible light (on the order of $10^{-3}\pi/a_0$). In the (20,20) tube, the same defect concentration leads to a mean distance between the defects of $12.5a_0$ or a corresponding wave vector $k =$

$0.16\pi/a_0$. For tubes of similar diameter but different chirality the mean distance between the defects varies only slightly at a given defect concentration. Since the phonon wave vectors that fulfill the double-resonance condition for the high-energy modes are all in the range of $0.1 - 0.3\pi/a_0$ (independent of the tube chirality), these modes originate from a double-resonance Raman process already at a low defect concentration. On the other hand, the phonon wave vectors leading to the D mode are large compared to those of Γ -point modes. A low defect concentration thus affects the D mode intensity much less than the HEM intensity. When the number of defects increases, the mean distance between the defects eventually becomes comparable with the wavelength of the D mode phonons. At this point, the D mode intensity increases rapidly as it benefits strongly from the enhancement of the defect concentration. The long-wavelength phonon modes in the HEM, on the other hand, are now less influenced by the increasing density of defects and exhibit only a weak enhancement. In this way we can understand the initial stronger rise of the D -mode signal as compared to that of the HEM.

Our results agree well with experiments on single-walled nanotubes, where, instead of impurity atoms, structural defects were introduced by γ -irradiation [208]. In these experiments the intensity of the HEM also increased with the defect concentration (irradiation time), until a saturation was reached. Thus the general effect of disorder on the Raman intensities in carbon nanotubes does not depend on the type of defects. In summary, we showed that defects contribute to the HEM scattering in carbon nanotubes, implying that nanotubes seen in Raman experiments probably always contain defects.

5.5 Absolute Raman cross section

So far we did not consider the matrix elements for the optical transitions and electron-phonon or electron-defect scattering in the above calculations of the Raman spectra. Instead, we regarded them as a constant \mathcal{M} , since we were interested only in the relative Raman cross section and the conditions for resonant scattering. Thereby we neglected their possible dependence on the chirality of the tube and, in the same tube, on the particular electron and phonon states. Now we will include the matrix elements explicitly to find a quantitative basis for the particularly large Raman signal from carbon nanotubes.

As a first step we determine the absolute Raman cross section both experimentally and theoretically for the radial breathing mode. The optical absorption in carbon nanotubes has been studied in great detail in the literature [84, 183, 212]; the matrix elements for electron-phonon coupling are much more difficult to access. Therefore, we restrict ourselves here to the fully symmetric radial breathing mode at the Γ point, *i.e.*, to first-order Raman scattering.

We are looking for the matrix elements $\langle 0, f, b | H_{ep} | 0, 0, a \rangle$ in Eq. (5.1). In the case of symmetric phonon modes (as the RBM), the matrix element can be found by evaluating the change in electronic energies due to the atomic displacement by the phonon mode [213]:

$$\langle 0, f, b | H_{ep} | 0, 0, b \rangle = \sqrt{\frac{\hbar}{2MN\omega^{\text{RBM}}}} \sum_a \varepsilon_a^{\text{RBM}} \frac{\partial E_b}{\partial \mathbf{u}_a}, \quad (5.15)$$

where b indicates the electron band index and wave vector, which is the same before and after scattering because the phonon is fully symmetric and the wave vector $q = 0$. The sum runs over all atoms a in the unit cell, M is the atomic mass, E_b the electronic energy and \mathbf{u}_a the atomic displacement. ε_a^i is the polarization vector of the phonon i normalized by $\sum_a \varepsilon_a^i \varepsilon_a^j = \delta_{ij}$, and N is the number of unit cells in the system ($N = 1$ in our calculation). The electron-phonon coupling is strong if the change in energy of the electronic state per unit displacement is large. The electronic energies in equilibrium position and with the atomic displacement, the RBM eigenvector, and the RBM frequency were calculated by M. Machón, see Ref. [214].

In general, the matrix elements for the RBM decrease with increasing tube diameter. The reason is that for the same radial displacement of the atoms, the change in bond length, and hence the effect on the electronic energies near the Fermi level, is smaller for larger diameters. In the limit of infinite diameter, the radial breathing mode becomes the out-of-plane translation of graphene, which at $k = 0$ does not alter the electronic energies. Furthermore, at similar diameter the electron-phonon coupling is stronger in zig-zag tubes than in armchair tubes [214]. Finally, when comparing different transitions in the same zig-zag tube, we find a systematic variation in both sign and absolute value of the matrix elements. If the matrix element is positive, its absolute value is small; *vice versa*, the absolute values of negative matrix elements are large. The first matrix element, \mathcal{M}_1 , is positive in those zig-zag (and presumably all semi-conducting) tubes that have $(n_1 - n_2) \bmod 3 = -1$, *e.g.*, in the (14,0) and the (17,0) tube. The changes of the matrix elements in sign and absolute value reflect which side of the graphene K point the electronic bands come from [214]. In particular, in zig-zag tubes they reflect whether the band index m is larger or smaller than $2n/3$ (see Sect. 2.1).

The above results show that the common assumption of constant electron-phonon coupling strength is not correct. The variation of the matrix elements is particularly important if Raman intensities from different nanotubes are compared in the analysis of experiments. For example, the approach in Ref. [148] to assign the chirality of the investigated tubes from Raman spectra is strongly based on the RBM intensities. This assignment relies on the assumption that the strongest RBM signal comes from a tube with the singularity in the joint density of states closest to the laser energy. We will show below explicitly, that the Raman intensity from different tubes at the same resonance condition directly reflects the differences in the electron-

phonon coupling strength. Thus the electron-phonon matrix elements have to be taken into account when comparing Raman intensities.

Strictly speaking, the assumption of constant matrix elements is incorrect even for electron-phonon scattering within the same electronic band of the same nanotube, because the coupling strength depends on the electron wave vector and probably on the phonon wave vector as well. This might affect the relative intensities of the Raman peaks in the spectra calculated above for the D mode and the HEM (Sects. 5.2 and 5.4), but it will not alter the understanding of the scattering processes and the qualitative agreement with experiments.

We now calculate the absolute Raman cross section for the RBM using the above determined matrix elements and compare the results with experiment. For first-order scattering, the absolute Raman scattering cross section per unit length and unit solid angle, $dS/d\Omega$, is given by [156, 215, 216]:

$$\frac{dS}{d\Omega} = \frac{\omega_l \omega_s^3 n_l n_s^3 V_c}{(2\pi)^2 c^4 (\hbar\omega_l)^2} [\mathcal{N}(\omega_{ph}) + 1] |K_{2f,10}|^2 \quad (5.16)$$

where $K_{2f,10}$ is given by Eq. (5.1). The indices $l(s)$ indicate the incoming (scattered) light, ω is the angular frequency of the photons, $\hbar\omega_{ph}$ the phonon energy, and n the refractive index. V_c denotes the unit-cell volume, c the vacuum velocity of light, and $\mathcal{N}(\omega_{ph})$ is the Bose-Einstein occupation number of the phonons. We convert the summation over k in $K_{2f,10}$ into an integral over transition energies $\hbar\omega$:

$$\frac{dS}{d\Omega} = \frac{\omega_l \omega_s^3 n_l n_s^3 V_c}{(2\pi)^2 c^4 (\hbar\omega_l)^2} [\mathcal{N}(\omega_{ph}) + 1] \left| \int \frac{\rho(\hbar\omega) \langle f | H_{eR} | b \rangle \langle b | H_{ep} | a \rangle \langle a | H_{eR} | i \rangle \hbar}{(E_l - \hbar\omega - i\gamma)(E_l - \hbar\omega_{ph} - \hbar\omega - i\gamma)} d\omega \right|^2, \quad (5.17)$$

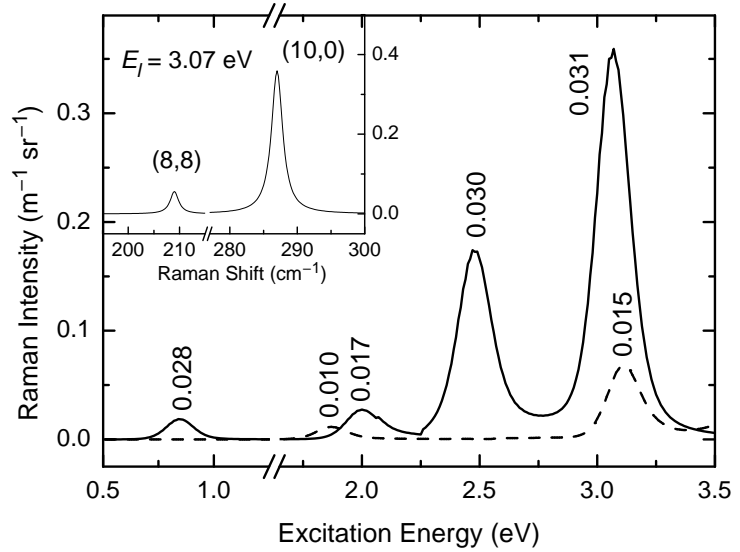
where $\rho(\hbar\omega)$ is the joint density of electronic states. Note that $dS/d\Omega$ is independent of the scattering volume V . For comparison with experiment, the Raman efficiency

$$\frac{d\sigma}{d\Omega} = V \frac{dS}{d\Omega} \quad (5.18)$$

must be calculated. To evaluate the absolute Raman cross section Eq. (5.17), we use the electron-phonon coupling matrix elements as given in Ref. [214], assuming that at a given transition energy only one pair of valence and conduction bands contributes significantly to the scattering process. The optical matrix elements, the refractive indices, and the joint density of states were obtained from *ab-initio* calculations with $\gamma = 0.1$ eV.

In Fig. 5.29 we show the calculated Raman cross section for the RBM of the (10,0) and the (8,8) tube as a function of laser energy. The first and second transitions of the (8,8) tube and the second and fourth transitions of the (10,0) tube, respectively, are at similar transition energy.

Figure 5.29: Absolute RBM Raman intensity as a function of excitation energy calculated for the (8,8) tube (dashed line) and the (10,0) tube (solid line). The numbers are the magnitude of the matrix elements in eV. Inset: RBM spectrum of the (8,8) and the (10,0) tube at $E_l = 3.07$ eV.

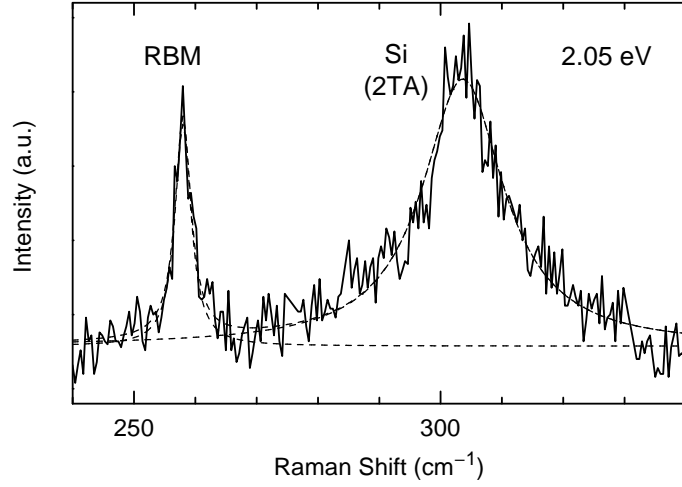


Then the difference in the Raman intensity is determined mainly by the different strength of the electron-phonon coupling. The ratio of the matrix elements is for instance $0.031/0.015 \approx 2$ at $E_l \approx 3$ eV; correspondingly the RBM intensity of the (10,0) tube is by a factor of ≈ 4 larger than the intensity of the (8,8) tube, see Fig. 5.29. The inset to Fig. 5.29 shows the calculated RBM spectra of the (8,8) and the (10,0) tube at $E_l = 3.07$ eV, where both tubes are closest to the resonance. The difference in intensity directly comes from the different electron-phonon coupling strength. Therefore, the larger intensity of the (10,0) tube does not indicate that in this tube the singularity in the joint density of states is closer to the laser energy than in the (8,8) tube, in contrast to the interpretation when constant matrix elements are assumed.

Furthermore, for the (10,0) tube Fig. 5.29 shows the variation of the electron-phonon matrix elements with different electronic bands. For constant matrix elements in a given tube, the maximum of the Raman cross section would follow roughly an E_l^2 dependence [Eq. (5.17)]. The variation of the matrix elements, however, leads to a deviation from this dependence. The second peak in the Raman resonance profile of the (10,0) tube is significantly weaker than expected for constant electron-phonon coupling. In an $(n_1 - n_2) \bmod 3 = -1$ tube, on the other hand, the second and third peak would be enhanced with respect to constant matrix elements. Therefore, one can, in principle, distinguish $(n_1 - n_2) \bmod 3 = -1$ and $(n_1 - n_2) \bmod 3 = +1$ tube families by measuring Raman resonance profiles over several resonant transitions of the same tube or by comparing relative intensities of tubes with close-by transition energies [86].

Experimentally, we determined the absolute Raman scattering efficiency $dS/d\Omega$ of the RBM of a particular carbon nanotube by comparing the measured peak area A_{RBM} with the simultaneously recorded second-order (2TA) Si peak at $300 \text{ cm}^{-1} A_{\text{Si}}$, see Fig. 5.30. At ex-

Figure 5.30: Experimental RBM spectra of an individual tube on a Si substrate, see Fig. 5.24, at two laser energies. The intensity of the RBM is approximately by a factor of 5 smaller than the intensity of the second-order acoustic peak of Si. To obtain the absolute cross section of the RBM scattering, the intensities have to be corrected for the different scattering volume and refractive indices.



citation energies $E_l = 2.05$ eV and 2.13 eV, the Raman intensity of the RBM is found to be $A_{\text{RBM}} = 0.2A_{\text{Si}}$. The absolute scattering cross section of the first order Si peak is known at $E_l = 1.9$ eV to be $1.68 \cdot 10^{-5} \text{ m}^{-1} \text{ sr}^{-1}$ [184, 217]. For the relative scattering intensity of the second-order 2TA to the first-order signal we obtained experimentally 0.05, resulting in an absolute value $dS_{\text{Si},2\text{TA}}/d\Omega = 0.084 \text{ m}^{-1} \text{ sr}^{-1}$. In order to find $dS_{\text{RBM}}/d\Omega$, we have to correct the measured peak areas for the scattering volume of Si and of the nanotube and their refractive indices [218]. No correction is necessary here for laser power, integration time or spectrometer sensitivity, because both the RBM and the second-order Si peak were recorded in the same measurement. Thus we obtain

$$\frac{dS_{\text{RBM}}/d\Omega}{dS_{\text{Si},2\text{TA}}/d\Omega} = \frac{A_{\text{RBM}}}{A_{\text{Si}}} \cdot \frac{V_{\text{Si}} \cdot n_{\text{RBM}}^2}{V_{\text{RBM}} \cdot n_{\text{Si}}^2}, \quad (5.19)$$

where n_{RBM} and n_{Si} are the refractive indices of the nanotube and Si, respectively, at the wavelength of the scattered light; $n_{\text{Si}} = 3.9$ at $E_l = 2.0$ eV [219]. For a metallic (semiconducting) tube at the first (second) singularity in the joint density of states we find from the above *ab-initio* calculations $n_{\text{RBM}} = 6.5$. The diameter of the laser focus is $\approx 1 \mu\text{m}$ on the sample. Using a cylinder with the diameter of the laser focus and length $1/\alpha$, where $\alpha = 4.5 \times 10^3 \text{ cm}^{-1}$ is the absorption coefficient of Si at $E_l = 2$ eV [219], we obtain for the scattering volume $V_{\text{Si}} = 1.728 \mu\text{m}^3$. We assume that the whole tube of ≈ 1 nm diameter and $1 \mu\text{m}$ length is illuminated, yielding $V_{\text{RBM}} = 0.785 \cdot 10^{-6} \mu\text{m}^3$. From Eq. (5.19) follows for the absolute Raman scattering cross section of the nanotube RBM signal

$$\frac{dS_{\text{RBM}}/d\Omega}{dS_{\text{Si},2\text{TA}}/d\Omega} = 1.2 \cdot 10^6,$$

and

$$dS_{\text{RBM}}/d\Omega = 1.1 \text{ m}^{-1} \text{ sr}^{-1}. \quad (5.20)$$

The scattering cross section of the nanotube for the RBM is thus by four orders of magnitude larger than that of Si at $E_l \approx 2 \text{ eV}$, reflecting the fact that the Raman signal of the nanotube, which is a single molecule, can be detected almost on the same scale as the Si second-order spectrum.

The calculated values for the (10,0) and the (8,8) tube at 2 eV excitation energy (0.03 and $0.01 \text{ m}^{-1} \text{ sr}^{-1}$, respectively) are much smaller than found experimentally. On the other hand, the experimental determination of the absolute Raman cross section is not trivial and contains some simplifications such as the correction by the refractive indices n_s in Eq. (5.19) or the determination of the scattering volume V_c . Furthermore, we found the absolute intensity with respect to another experimentally determined cross section, which is another source of error [184]. Together with the uncertainties in the calculation such as the choice of the broadening parameter γ , the error might amount to an order of magnitude. In the present calculations we did not include the contributions from defect-induced, double-resonant scattering, which can further enhance the Raman cross section. The calculation of the matrix elements for electron-defect scattering as well as for electron-phonon scattering for arbitrary phonon wave vectors, however, is beyond the scope of this work.

In summary, the matrix elements for electron-phonon scattering of the RBM in carbon nanotubes depend strongly on the diameter and chirality of the tube as well as on the particular electronic bands. We used the *ab-initio* calculated matrix elements to determine the absolute Raman cross section for the RBM in first-order scattering and found the Raman intensity to be significantly smaller than in experiment. This discrepancy is partly due to uncertainties in both the calculation and the experiment, but it might also be an indication for the double-resonant nature of the RBM, explaining the much larger cross section in the experiment.

5.6 Summary: Single- and double-resonance interpretation

We discussed above the interpretation of the Raman spectra of carbon nanotubes within the model of defect-induced, double-resonant scattering. We proposed that the entire Raman spectrum is determined by double resonances, and showed that this is consistent with the experimental results on both individual nanotubes and tube ensembles. Since the implications of this model are in part contradictory to the more conventional model of diameter-selective single resonances, which is still applied in the literature, we will summarize here the discussion between these two concepts.

The single-resonance model is the conventional one and assumes scattering by Γ -point phonons only. Furthermore, the singularities in the electronic density of states play a dominant role. A tube contributes to the Raman signal only if the incoming or outgoing photon energy closely matches a singularity. Therefore, the Raman intensity of a given tube is either large, in the case of a resonance, or approximately zero. Consequently, in carbon-nanotube ensembles specific tubes are selected by the choice of the laser energy (diameter-selective resonance). Line shape or frequency of the Raman modes cannot change for a given tube by variation of the laser wavelength. Also for the D mode, which is widely accepted to result from a double-resonant process, the *shift* with excitation energy is sometimes attributed to selective enhancement of different tubes. In general, any variations of the Raman spectra with laser energy imply that different tubes are excited, when the single-resonance interpretation is invoked.

In the double-resonance model, phonons with large wave vectors are allowed by defect scattering, and are selectively enhanced in a double-resonant process. This interpretation does not explicitly exclude single resonances – in fact, they are always included in calculations of the Raman cross section, see for instance Eq. (5.2) – but the double-resonance dominates the Raman spectra. The role of the singularities in the electronic density of states is considered as well, *i.e.*, the Raman cross section increases for incoming or outgoing resonances close to the singularities. In addition, the phonon density of states is equally important. Moreover, the enhancement by double instead of single resonances can compensate for a lower electronic density of states. In bulk samples with many different tubes, the laser energy will exactly match the singularities for only a few of them. These tubes contribute with a strong signal, as in the single-resonance picture. Nevertheless, the contributions from the remaining tubes, neglected in the single-resonance model, can sum up to a comparable signal. This is supported by experiments on the same individual tube for several laser energies that cannot all match the singularities exactly.

From a theoretical point of view, defect-induced, double-resonant scattering for the high-energy and the radial breathing modes can occur in carbon nanotubes, because it is the same process that is allowed for the D mode. The only difference is the smaller phonon wave vec-

tor. This makes the process even more favorable, since a wave vector on the order of δ^{-1} corresponds to a mean distance δ between the defects and hence a lower defect concentration is required than for the D mode. Raman experiments on boron-doped nanotubes showed that the intensity of the high-energy modes increased with defect (boron) concentration. Moreover, the single-resonance model does not give a convincing explanation for the line shape of the high-energy peaks, in particular, the amplitude ratio of the peaks. Interpretations based on possibly different symmetries of the Raman modes, like the assignment to A_{1g} , E_{1g} , and E_{2g} modes, are contradicted by polarization-dependent Raman experiments showing that the high-energy spectra are uniformly dominated by fully symmetric phonon modes. In contrast, the double-resonance model offers a straightforward explanation for the complex line shape of the high-energy modes from only A_1 -symmetry phonons.

The double-resonance interpretation is strongly supported by experiments. Both the D mode and the high-energy mode in the same individual tube were found to depend on laser energy in frequency and shape. This result is the fingerprints of defect-induced, double-resonant Raman scattering and cannot be understood by single-resonant scattering of only Γ -point modes. In general, the strong enhancement of the Raman cross section by a double resonance explains why the Raman signal of a single molecule such as an isolated nanotube can be detected on a scale comparable with the second-order modes of bulk silicon. The double-resonance picture consistently explains a number of experimental results from Raman scattering on carbon nanotubes, such as the laser-energy dependence of the modes, their symmetry properties, and their line shape.

In summary, our experiments and modeling revealed that the double-resonance process is the predominant origin of the entire Raman spectrum of carbon nanotubes. The essential difference to the single-resonance picture is that variations of the Raman spectra with excitation energy are not always attributed to selective enhancement of different *tubes* but of different *phonon* wave vectors in the same tube. Consequently, the double-resonance model leads to different conclusions about the properties of the investigated tubes. Since the Raman line shape can change in the same tube depending on laser energy, a “semiconducting” spectrum does not necessarily indicate a semiconducting tube. Instead the spectrum can also result from a metallic tube. A “metallic” Raman spectrum, however, is still a signature of metallic tubes, because only metallic tubes have the softened phonon frequencies and the strong electron-phonon coupling that give rise to the large Raman signal on the low-energy side of the HEM. Regarding the D mode, only metallic tubes with $\mathcal{R} = 3$, *i.e.*, $(n_1 - n_2)/3$ integer, exhibit a strong D -mode scattering. Therefore, the absence of the D mode, which is usually taken as an indication of low defect concentration, can instead also result from a semiconducting or a metallic $\mathcal{R} = 1$ tube. Finally, if the entire Raman spectrum of carbon nanotubes is determined

by double-resonant Raman scattering, the radial breathing mode, too, shifts with laser energy. The shift of the radial breathing mode is probably smaller than for the high-energy modes because of its flat dispersion close to the Γ point. Given the large uncertainties in the relation between the RBM frequency and the tube diameter, the additional correction due to the double resonance is, most likely, small. For a verification of all predictions from this model, further experiments on isolated tubes are needed, where the metallic or semiconducting character of the tube or even its chirality are known from independent measurements.

6 Conclusion

In this work we developed a coherent picture of the Raman scattering processes in carbon nanotubes. We showed that the entire first-order Raman spectrum of carbon nanotubes is dominated by defect-induced, double-resonant scattering. In this interpretation, the observed Raman peaks are not Γ -point modes as in conventional first-order scattering. Instead, they arise from phonons with finite wave vector in a second-order process including elastic scattering by a defect. The phonon modes that match the double-resonance condition are enhanced and give rise to the Raman signal. As this condition depends on excitation energy, the peak positions, shape and relative intensities of the spectrum change correspondingly. Therefore, by scanning the excitation energy one can partly map the phonon dispersion of a carbon nanotube.

The previous model of conventional single-resonant Raman scattering attributed the variation of the spectra to selective excitation of specific tubes in a nanotube ensemble. It cannot explain the laser-energy dependence observed in an individual tube, nor is it able to reproduce the peculiar line shape of the high-energy mode correctly. In contrast, the double-resonance model explains the Raman spectrum of carbon nanotubes in a consistent way.

The Raman process includes absorption and emission of light, electron-phonon scattering, and, in the case of defect-induced scattering, electron-defect interaction. In order to be able to model the entire Raman spectrum of carbon nanotubes, we calculated the nanotube phonon dispersion by force constants in a symmetry-based approach. From the symmetry of the electron and phonon states we derived selection rules for each step in the Raman process. We calculated the D mode and the high-energy mode within the double-resonance picture. Our calculation includes only fully symmetric phonon modes, which were found both from polarization-dependent experiments and from theory to contribute most to the signal. The observed multiple-peak line shape of the modes is found to arise from slightly different double-resonance conditions for altered time orders, for asymmetric band extrema, and for several close-by electronic bands in chiral nanotubes. In experiments we found that the two strongest peaks of the high-energy mode shift into opposite direction with excitation energy. This is easily understood in the double-resonance picture as the high-energy peaks follow the phonon dispersion with increasing laser energy from the Γ point towards larger wave vectors. The

phonon energy decreases for the TO-derived branch and increases according to the overbending in the LO-derived branch, resulting in the observed negative and positive slopes of the frequency shift. Furthermore, we performed Raman experiments on boron-doped nanotubes, which supported the predicted dependence of the high-energy mode intensity on the defect concentration. Overall, we obtain a very good agreement with the experimental results.

Since the excitation-energy dependent Raman experiments were always carried out on nanotube ensembles of all chiral angles and with a large diameter distribution, it was difficult to distinguish whether different tubes were excited when changing the laser energy (single resonance), or whether different phonons from the same tube were observed (double resonance). Clearly, the experiment to solve this controversy is to record the Raman spectra of the same individual nanotube at several excitation energies. We performed such measurements and found that both the D mode and the high-energy mode change with laser energy, as predicted by the double-resonance model. Moreover, the line shape of the high-energy mode changed continuously from metallic-like to semiconducting-like, in accordance with the phonon dispersion predicted for metallic nanotubes. Therefore, the line shape that was previously believed to indicate the excitation of semiconducting nanotubes, can also result from metallic tubes.

In double-resonant Raman scattering, the excited phonon modes and the Raman-frequency shift depend sensitively on the phonon dispersion itself. The existing theoretical predictions of the phonon dispersion, however, were contradictory for graphite already, resulting in contradicting theories for carbon nanotubes. Surprisingly, the optical phonon branches of graphite had never been completely measured. This comes mainly from the lack of single crystals that are sufficiently large for inelastic neutron scattering. We now determined the entire optical phonon branches of graphite by the rather young experimental technique of inelastic X-ray scattering. For the TO-derived phonon branch, we found a particularly large dispersion that was underestimated in most of the previous calculations. At the K point, this branch is strongly softened in frequency, indicating a large coupling to the electronic system. The TO-derived phonons near the K point are the ones leading to the D mode in the Raman spectrum. Our result therefore solves an open question in double-resonant Raman scattering: a large number of symmetry-allowed double-resonant peaks could in principle be expected in carbon nanotubes instead of only the D mode and the high-energy mode. Apparently, the observation of predominantly two lines reflects a particularly strong electron-phonon coupling for these modes. Such a strong coupling had been previously found for the LO-derived Γ point mode in metallic nanotubes (leading to the metallic high-energy modes) and is now observed for the K -point phonon that gives rise to the D mode. Based on the experimental results of the graphite phonon dispersion we refined and extended the calculations of the D -mode spectra. In addition, we analytically studied the interference and dimensionality effects in the Raman process. By using

the experimental phonon dispersion we obtained an excellent quantitative agreement between our calculation and the experiments.

The next level of insight into the Raman process in carbon nanotubes is found in the absolute Raman cross section. As a first step we determined the absolute intensity of the radial breathing mode and calculated its first-order cross section. We included the matrix elements of the electron-phonon and electron-photon interaction explicitly. The calculated Raman cross section is by 1 – 2 orders of magnitude smaller than in experiment. This result might partly be due to large uncertainties in both the calculation and the measurement. Furthermore it might indicate that the RBM results from double-resonant scattering as well.

The double-resonant origin of the spectra and the resulting changes with laser energy have to be taken into account when characterizing the nanotube sample by Raman spectroscopy. First, semiconducting-like spectra might also arise from metallic nanotubes, whereas metallic-like spectra unambiguously indicate metallic tubes. Second, the Raman intensity of the high-energy mode depends on the defect concentration in the sample similarly to the *D* mode. Third, the Raman spectrum of carbon nanotubes can be detected also if the excitation energy is not exactly in resonance with the singularities in the joint electronic density of states.

Our experimental determination of the graphite phonon dispersion is the foundation for revised phonon dispersion relations in carbon nanotubes. Further studies on the absolute Raman cross section will provide another distinction between single- and double-resonant processes. We were able to confirm the predicted chirality dependence of the electron-phonon scattering matrix elements qualitatively in recent experiments on the intensity of the radial breathing modes.

Bibliography

- [1] H. W. Kroto, J. R. Heath, S. C. O'Brien, R. F. Curl, and R. E. Smalley, "C₆₀: Buckminsterfullerene", *Nature* **318**, 162 (1985).
- [2] S. Iijima, "Helical microtubules of graphitic carbon", *Nature* **354**, 56 (1991).
- [3] S. Iijima and T. Ichihashi, "Single-shell carbon nanotubes of 1-nm diameter", *Nature* **363**, 603 (1993).
- [4] D. S. Bethune, C. H. Kiang, M. S. deVries, G. Gorman, R. Savoy, J. Vazques, and R. Beyers, "Cobalt-catalyzed growth of carbon nanotubes with single-atomic-layer", *Nature* **363**, 605 (1993).
- [5] W. Krätschmer, L. D. Lamb, K. Fostiropoulos, and D. R. Huffman, "Solid C₆₀: a new form of carbon", *Nature* **347**, 354 (2000).
- [6] M. Radosavljević, J. Lefebvre, and A. T. Johnson, "High-field electrical transport and breakdown in bundles of single-wall carbon nanotubes", *Phys. Rev. B* **64**, 241 307(R) (2001).
- [7] S.-B. Lee, K. B. K. Teo, L. A. W. Robinson, A. S. Teh, M. Chhowalla, *et al.*, "Characteristics of multiwalled carbon nanotube nanobridges fabricated by poly(methylmethacrylate) suspended dispersion", *J. Vac. Sci. Technol. B* **20**, 2773 (2002).
- [8] J.-P. Salvetat, G. A. D. Briggs, J.-M. Bonard, R. R. Bacsá, A. J. Kulik, *et al.*, "Elastic and shear moduli of single-walled carbon nanotube ropes", *Phys. Rev. Lett.* **82**, 944 (1999).
- [9] M. M. J. Treacy, T. W. Ebbesen, and J. M. Gibson, "Exceptionally high Young's modulus observed for individual carbon nanotubes", *Nature* **381**, 678 (1996).
- [10] A. Kis, G. Csányi, J.-P. Salvetat, T.-N. Lee, E. Couteau, *et al.*, "Reinforcement of single-walled carbon nanotube bundles by intertube bridging", *Nature Materials* **3**, 153 (2004).

- [11] P. Avouris, “Molecular electronics with carbon nanotubes”, *Acc. Chem. Res.* **35**, 1026 (2002).
- [12] A. Bachtold, P. Hadley, T. Nakanishi, and C. Dekker, “Logic circuits with carbon nanotube transistors”, *Science* **294**, 1317 (2001).
- [13] R. H. Baughman, C. Cui, A. Zakhidov, Z. Iqbal, J. N. Barisci, *et al.*, “Carbon nanotube actuators”, *Science* **284**, 1340 (1999).
- [14] M. Stoll, P. M. Rafailov, W. Frenzel, and C. Thomsen, “Electrochemical and Raman measurements on single-walled carbon nanotubes”, *Chem. Phys. Lett.* **375**, 625 (2003).
- [15] P. A. Williams, S. J. Papadakis, A. M. Patel, M. R. Falvo, S. Washburn, and R. Superfine, “Fabrication of nanometer-scale mechanical devices incorporating individual multiwalled carbon nanotubes as torsional springs”, *Appl. Phys. Lett.* **82**, 805 (2003).
- [16] A. M. Fennimore, T. D. Yuzvinsky, W.-Q. Han, M. S. Fuhrer, J. Cumings, and A. Zettl, “Rotational actuators based on carbon nanotubes”, *Nature* **424**, 408 (2003).
- [17] T. W. Odom, J. L. Huang, P. Kim, and C. M. Lieber, “Atomic structure and electronic properties of single-walled carbon nanotubes”, *Nature* **391**, 62 (1998).
- [18] P. Kim, T. W. Odom, J.-L. Huang, and C. M. Lieber, “Electronic density of states of atomically resolved single-walled carbon nanotubes: Van Hove singularities and end states”, *Phys. Rev. Lett.* **82**, 1225 (1999).
- [19] L. C. Venema, J. W. Janssen, M. R. Buitelaar, J. W. G. Wildöer, S. G. Lemay, L. P. Kouwenhoven, and C. Dekker, “Spatially resolved scanning tunneling spectroscopy on single-walled carbon nanotubes”, *Phys. Rev. B* **62**, 5238 (2000).
- [20] M. Bockrath, D. H. Cobden, J. Lu, A. G. Rinzler, R. E. Smalley, L. Balents, and P. L. McEuen, “Luttinger-liquid behaviour in carbon nanotubes”, *Nature* **397**, 598 (1999).
- [21] R. Egger, A. Bachtold, M. Fuhrer, M. Bockrath, D. Cobden, and P. McEuen, “Luttinger liquid behavior in metallic carbon nanotubes”, in *Interacting Electrons in Nanostructures*, edited by R. Haug and H. Schoeller (Springer, Berlin, 2001), vol. 579 of *Lecture Notes in Physics*.
- [22] S. Frank, P. Poncharal, Z. L. Wang, and W. A. de Heer, “Carbon nanotube quantum resistors”, *Science* **280**, 1744 (1998).

- [23] J. Nygård, D. Cobden, M. Bockrath, P. McEuen, and P. Lindelof, “Electrical transport measurements on single-walled carbon nanotubes”, *Appl. Phys. A: Mater. Sci. Process.* **69**, 297 (1999).
- [24] Z. Yao, C. Dekker, and P. Avouris, “Electrical transport through single-wall carbon nanotubes”, in *Carbon Nanotubes*, edited by M. S. Dresselhaus, G. Dresselhaus, and P. Avouris (Springer, Berlin, 2001), vol. 80 of *Topics in Applied Physics*, p. 146.
- [25] A. R. Goñi, L. N. Pfeiffer, K. W. West, A. Pinczuk, H. U. Baranger, and H. L. Stormer, “Observation of quantum wire formation at intersecting quantum wells”, *Appl. Phys. Lett.* **61**, 1956 (1992).
- [26] O. M. Auslaender, A. Yacoby, R. de Picciotto, K. W. Baldwin, L. N. Pfeiffer, and K. W. West, “Tunneling spectroscopy of the elementary excitations in a one-dimensional wire”, *Science* **295**, 825 (2002).
- [27] A. M. Chang, “Chiral luttinger liquids at the fractional quantum hall edge”, *Rev. Mod. Phys.* **75**, 1449 (2003).
- [28] I. Božović, M. Vujičić, and F. Herbut, “Irreducible representations of the symmetry groups of polymer molecules I”, *J. Phys. A* **11**, 2133 (1978).
- [29] I. Božović and M. Vujičić, “Irreducible representations of the symmetry groups of polymer molecules II”, *J. Phys. A* **14**, 777 (1981).
- [30] M. Damnjanović, “Standard components of polar and axial vectors for quasi one-dimensional systems”, *Phys. Lett. A* **94**, 337 (1983).
- [31] S. Reich, C. Thomsen, and J. Maultzsch, *Carbon Nanotubes: Basic Concepts and Physical Properties* (Wiley-VCH, Berlin, 2004).
- [32] J.-C. Charlier and S. Iijima, “Growth mechanisms of carbon nanotubes”, in *Carbon Nanotubes*, edited by M. S. Dresselhaus, G. Dresselhaus, and P. Avouris (Springer, Berlin, 2001), vol. 80 of *Topics in Applied Physics*, p. 55.
- [33] H. Dai, “Nanotube growth and characterization”, in *Carbon Nanotubes*, edited by M. S. Dresselhaus, G. Dresselhaus, and P. Avouris (Springer, Berlin, 2001), vol. 80 of *Topics in Applied Physics*, p. 29.
- [34] G. S. Duesberg, I. Loa, M. Burghard, K. Syassen, and S. Roth, “Polarized Raman spectroscopy of individual single-wall carbon nanotubes”, *Phys. Rev. Lett.* **85**, 5436 (2000).

- [35] M. J. O'Connell, S. M. Bachilo, C. B. Huffman, V. C. Moore, M. S. Strano, *et al.*, "Band gap fluorescence from individual single-walled carbon nanotubes", *Science* **297**, 593 (2002).
- [36] S. M. Bachilo, M. S. Strano, C. Kittrell, R. H. Hauge, R. E. Smalley, and R. B. Weisman, "Structure-assigned optical spectra of single-walled carbon nanotubes", *Science* **298**, 2361 (2002).
- [37] S. Lebedkin, F. Hennrich, T. Skipa, and M. M. Kappes, "Near-infrared photoluminescence of single-walled carbon nanotubes prepared by the laser vaporization method", *J. Phys. Chem. B* **107**, 1949 (2003).
- [38] A. Hagen and T. Hertel, "Quantitative analysis of optical spectra from individual single-wall carbon nanotubes", *Nano Lett.* **3**, 383 (2003).
- [39] J. Lefebvre, Y. Homma, and P. Finnie, "Bright band gap photoluminescence from unprocessed single-walled carbon nanotubes", *Phys. Rev. Lett.* **90**, 217 401 (2003).
- [40] G. N. Ostojic, S. Zaric, J. Kono, M. S. Strano, V. C. Moore, R. H. Hauge, and R. E. Smalley, "Interband recombination dynamics in resonantly excited single-walled carbon nanotubes", *Phys. Rev. Lett.* **92**, 117 402 (2004).
- [41] Y.-Z. Ma, J. Stenger, J. Zimmermann, S. M. Bachilo, R. E. Smalley, R. B. Weisman, and G. R. Fleming, "Ultrafast carrier dynamics in single-walled carbon nanotubes probed by femtosecond spectroscopy", *J. Chem. Phys.* **120**, 3368 (2004).
- [42] R. Krupke, F. Hennrich, H. v. Löhneysen, and M. M. Kappes, "Separation of metallic from semiconducting single-walled carbon nanotubes", *Science* **301**, 344 (2003).
- [43] J. Maultzsch, S. Reich, and C. Thomsen, "Raman scattering in carbon nanotubes revisited", *Phys. Rev. B* **65**, 233 402 (2002).
- [44] A. G. Souza-Filho, A. Jorio, G. Samsonidze, G. Dresselhaus, M. A. Pimenta, *et al.*, "Competing spring constant versus double resonance effects on the properties of dispersive modes in isolated single-wall carbon nanotubes", *Phys. Rev. B* **67**, 035 427 (2003).
- [45] A. Jorio, M. A. Pimenta, A. G. Souza-Filho, G. G. Samsonidze, A. K. Swan, *et al.*, "Resonance Raman Spectra of Carbon Nanotubes by Cross-Polarized Light", *Phys. Rev. Lett.* **90**, 107 403 (2003).
- [46] M. Damnjanović, I. Milošević, T. Vuković, and R. Sredanović, "Full symmetry, optical activity, and potentials of single-wall and multiwall nanotubes", *Phys. Rev. B* **60**, 2728 (1999).

- [47] M. Damnjanović, T. Vuković, and I. Milošević, “Modified group projectors: Tight binding method”, *J. Phys. A: Math. Gen.* **33**, 6561 (2000).
- [48] S. Reich, H. Jantoljak, and C. Thomsen, “Shear strain in carbon nanotubes under hydrostatic pressure”, *Phys. Rev. B* **61**, R13 389 (2000).
- [49] C. Journet and P. Bernier, “Production of carbon nanotubes”, *Appl. Phys. A: Mater. Sci. Process.* **67**, 1 (1998).
- [50] M. J. Bronikowski, P. A. Willis, D. T. Colbert, K. A. Smith, and R. E. Smalley, “Gas-phase production of carbon single-walled nanotubes from carbon monoxide via the HiPco process: A parametric study”, *J. Vac. Sci. Technol. A* **19**, 1800–1805 (2001).
- [51] L. Henrard, A. Loiseau, C. Journet, and P. Bernier, “Study of the symmetry of single-wall nanotubes by electron diffraction”, *Eur. Phys. B* **13**, 661 (2000).
- [52] C. Qin and L.-M. Peng, “Measurement accuracy of the diameter of a carbon nanotube from TEM images”, *Phys. Rev. B* **65**, 155 431 (2002).
- [53] Z. Zhang and C. M. Lieber, “Nanotube structure and electronic properties probed by scanning tunneling microscopy”, *Appl. Phys. Lett.* **62**, 2792 (1993).
- [54] M. Ge and K. Sattler, “Vapor-condensation generation and STM analysis of fullerene tubes”, *Science* **260**, 515 (1993).
- [55] J. W. G. Wildöer, L. C. Venema, A. G. Rinzler, R. E. Smalley, and C. Dekker, “Electronic structure of atomically resolved carbon nanotubes”, *Nature* **391**, 59 (1998).
- [56] T. W. Odom, J. H. Hafner, and C. M. Lieber, “Scanning probe microscopy studies of carbon nanotubes”, in *Carbon Nanotubes*, edited by M. S. Dresselhaus, G. Dresselhaus, and P. Avouris (Springer, Berlin, 2001), vol. 80 of *Topics in Applied Physics*, p. 173.
- [57] A. Hassanien, M. Tokumoto, S. Oshima, Y. Kuriki, F. Ikazaki, K. Uchida, and M. Yumura, “Geometrical structure and electronic properties of atomically resolved multiwall carbon nanotubes”, *Appl. Phys. Lett.* **75**, 2755 (1999).
- [58] J. Muster, M. Burghard, S. Roth, G. S. Duesberg, E. Hernández, and A. Rubio, “Scanning force microscopy characterization of individual carbon nanotubes on electrode arrays”, *J. Vac. Sci. Technol. B* **16**, 2796 (1998).
- [59] X. B. Zhang, X. F. Zhang, S. Amelinckx, G. Van Tendeloo, and J. Van Landuyt, “The reciprocal space of carbon nanotubes: A detailed interpretation of the electron diffraction effects”, *Ultramicroscopy* **54**, 237 (1994).

- [60] L. C. Qin, T. Ichihashi, and S. Iijima, "On the measurement of helicity of carbon nanotubes", *Ultramicroscopy* **67**, 181 (1997).
- [61] A. A. Lucas, F. Moreau, and P. Lambin, "Optical simulations of electron diffraction by carbon nanotubes", *Rev. Mod. Phys.* **74**, 1 (2002).
- [62] M. Gao, J. M. Zuo, R. D. Twisten, I. Petrov, L. A. Nagahara, and R. Zhang, "Structure determination of individual single-wall carbon nanotubes by nanoarea electron diffraction", *Appl. Phys. Lett.* **82**, 2703 (2003).
- [63] N. Božović, I. Božović, and M. Damnjanović, "Selection rules for polymers and quasi one-dimensional crystals: IV. Kronecker product for the line groups isogonal to D_{nh} ", *J. Phys. A: Math. Gen.* **18**, 923 (1985).
- [64] M. Damnjanović, I. Božović, and N. Božović, "Selection rules for polymers and quasi one-dimensional crystals: II. Kronecker product for the line groups isogonal to D_n ", *J. Phys. A: Math. Gen.* **17**, 747 (1984).
- [65] M. Damnjanović, I. Milošević, T. Vuković, and R. Sredanović, "Symmetry and lattices of single-wall nanotubes", *J. Phys. A* **32**, 4097 (1999).
- [66] I. N. Bronstein and K. Semendjajew, *Taschenbuch der Mathematik* (Harry Deutsch, Frankfurt, 1973).
- [67] T. Inui, Y. Tanabe, and Y. Onodera, *Group Theory and its Application in Physics* (Springer, Berlin, 1996).
- [68] G. Burns, *Introduction to group theory with applications* (Academic, New York, 1977).
- [69] V. Heine, *Group Theory in Quantum Mechanics: An Introduction to its present usage* (Pergamon, Oxford, 1977).
- [70] M. Tinkham, *Group theory and quantum mechanics* (McGraw-Hill, New York, 1964).
- [71] I. Milošević and M. Damnjanović, "Normal vibrations and Jahn-Teller effect for polymers and quasi-one-dimensional systems", *Phys. Rev. B* **47**, 7805 (1993).
- [72] J. W. Mintmire, B. I. Dunlap, and C. T. White, "Are fullerene tubules metallic?", *Phys. Rev. Lett.* **68**, 631 (1992).
- [73] C. T. White, D. H. Robertson, and J. W. Mintmire, "Helical and rotational symmetries of nanoscale graphitic tubules", *Phys. Rev. B* **47**, 5485 (1993).

- [74] M. Damnjanović, I. Milošević, T. Vuković, and J. Maultzsch, “Quantum numbers and band topology of nanotubes”, *J. Phys. A* **36**, 5707 (2003).
- [75] T. Vuković, I. Milošević, and M. Damnjanović, “Carbon nanotubes band assignation, topology, Bloch states, and selection rules”, *Phys. Rev. B* **65**, 045 418 (2002).
- [76] E. B. Wilson, J. C. Decius, and P. C. Cross, *Molecular Vibrations* (Dover, New York, 1980).
- [77] P. R. Wallace, “The band theory of graphite”, *Phys. Rev.* **71**, 622 (1947).
- [78] S. Reich, J. Maultzsch, C. Thomsen, and P. Ordejón, “Tight-binding description of graphene”, *Phys. Rev. B* **66**, 035 412 (2002).
- [79] M. Damnjanović, T. Vuković, and I. Milošević, “Fermi level quantum numbers and secondary gap of conducting carbon nanotubes”, *Solid State Commun.* **116**, 265 (2000), Table 1 in this reference contains a small error: For chiral tubes and the \tilde{k} quantum numbers $\tilde{k}_F = 2q\pi/3na$ for $\mathcal{R} = 3$ tubes and $\tilde{k}_F = 0$ for $\mathcal{R} = 1$ nanotubes.
- [80] C. T. White and J. W. Mintmire, “Density of states reflects diameter in nanotubes”, *Nature* **394**, 29 (1998).
- [81] J. W. Mintmire and C. T. White, “Universal density of states for carbon nanotubes”, *Phys. Rev. Lett.* **81**, 2506 (1998).
- [82] H. Kataura, Y. Kumazawa, Y. Maniwa, I. Umezu, S. Suzuki, Y. Ohtsuka, and Y. Achiba, “Optical properties of single-wall carbon nanotubes”, *Synth. Met.* **103**, 2555 (1999).
- [83] X. Blase, L. X. Benedict, E. L. Shirley, and S. G. Louie, “Hybridization effects and metallicity in small radius carbon nanotubes”, *Phys. Rev. Lett.* **72**, 1878 (1994).
- [84] M. Machón, S. Reich, C. Thomsen, D. Sánchez-Portal, and P. Ordejón, “*Ab initio* calculations of the optical properties of 4-Å-diameter single-walled nanotubes”, *Phys. Rev. B* **66**, 155 410 (2002).
- [85] S. Reich, C. Thomsen, and P. Ordejón, “Electronic band structure of isolated and bundled carbon nanotubes”, *Phys. Rev. B* **65**, 155 411 (2002).
- [86] H. Telg, J. Maultzsch, S. Reich, F. Hennrich, and C. Thomsen, “Chirality distribution and transition energies of carbon nanotubes”, (2004), submitted to *Phys. Rev. Lett.*
- [87] C. L. Kane and E. J. Mele, “Ratio problem in single carbon nanotube fluorescence spectroscopy”, *Phys. Rev. Lett.* **90**, 207 401 (2003).

- [88] C. D. Spataru, S. Ismail-Beigi, L. X. Benedict, and S. G. Louie, “Excitonic effects and optical spectra of single-walled carbon nanotubes”, *Phys. Rev. Lett.* **93**, 077 402 (2004).
- [89] P. Y. Yu and M. Cardona, *Fundamentals of Semiconductors* (Springer, Berlin, 1999, 2nd ed.).
- [90] U. Kuhlmann, H. Jantoljak, N. Pfänder, P. Bernier, C. Journet, and C. Thomsen, “Infrared active phonons in single-walled carbon nanotubes”, *Chem. Phys. Lett.* **294**, 237 (1998).
- [91] U. Kuhlmann, H. Jantoljak, N. Pfänder, C. Journet, P. Bernier, and C. Thomsen, “Infrared reflectance of single-walled carbon nanotubes”, *Synth. Met.* **103**, 2506 (1999).
- [92] A. Mizel, L. X. Benedict, M. L. Cohen, S. G. Louie, A. Zettl, N. K. Budraa, and W. P. Beyermann, “Analysis of the low-temperature specific heat of multiwalled carbon nanotubes and carbon nanotube ropes”, *Phys. Rev. B* **60**, 3264 (1999).
- [93] S. Rols, Z. Benes, E. Anglaret, J. L. Sauvajol, P. Papanek, *et al.*, “Phonon density of states of single-walled carbon nanotubes”, *Phys. Rev. Lett.* **85**, 5222 (2000).
- [94] K. B. J. C. Lasjaunias, Z. Benes, J. E. Fischer, and P. Monceau, “Low-temperature specific heat of single-wall carbon nanotubes”, *prb* **65**, 113 409 (2002).
- [95] B. N. Brockhouse and P. K. Iyengar, “Normal modes of germanium by neutron spectrometry”, *Phys. Rev.* **111**, 747 (1958).
- [96] J. L. Warren, J. L. Yarnell, G. Dolling, and R. A. Cowley, “Lattice dynamics of diamond”, *Phys. Rev.* **158**, 805 (1967).
- [97] G. Nilsson and G. Nelin, “Phonon dispersion relation in Ge at 80° K”, *Phys. Rev. B* **3**, 364 (1971).
- [98] M. M. Beg and S. M. Shapiro, “Study of phonon dispersion relations in cuprous oxide by inelastic neutron scattering”, *Phys. Rev. B* **13**, 1728 (1976).
- [99] D. Strauch and B. Dorner, “Phonon dispersion in GaAs”, *J. Phys.: Condens. Matter* **2**, 1457 (1990).
- [100] C. V. Raman, “A Change of Wave-length in Light Scattering”, *Nature* **121**, 619 (1928).
- [101] B. A. Weinstein and M. Cardona, “Second-order Raman Spectrum of Germanium”, *Phys. Rev. B* **7**, 2545 (1973).

- [102] M. L. Bansal, A. K. Sood, and M. Cardona, “Strongly dispersive low frequency Raman modes in Germanium”, *Solid State Commun.* **78**, 579 (1991).
- [103] E. Burkel, B. Dorner, T. Illini, and J. Peisl, “First observations of phonon dispersion curves with inelastic x-ray scattering”, *Rev. Sci. Instrum.* **60**, 1671 (1989).
- [104] E. Burkel, “Phonon spectroscopy by inelastic x-ray scattering”, *Rep. Prog. Phys.* **63**, 171 (2000).
- [105] H. Fukazawa, S. Ikeda, M. Oguro, S. M. Bennington, and S. Mae, “Phonon dispersion curves in KOD-doped ice observed by neutron scattering”, *J. Chem. Phys.* **118**, 1577 (2003).
- [106] C. H. Gardiner, A. T. Boothroyd, B. H. Larsen, W. Reichardt, A. A. Zhokhov, *et al.*, “Phonon dispersion relations in $\text{PrBa}_2\text{Cu}_3\text{O}_{6+x}$ ($x \approx 2$)”, *Phys. Rev. B* **69**, 092 302 (2004).
- [107] F. Occelli, M. Krisch, P. Loubeyre, F. Sette, R. Le Toullec, C. Masciovecchio, and J.-P. Rueff, “Phonon dispersion curves in an argon single crystal at high pressure by inelastic x-ray scattering”, *Phys. Rev. B* **63**, 224 306 (2001).
- [108] C. Kittel, *Introduction to Solid State Physics* (Wiley, New York, 1996), 7th edn.
- [109] O. Madelung, *Introduction to Solid-State Theory*, vol. 2 of *Springer Series in Solid-State Science* (Springer, Berlin, 1981).
- [110] R. Nicklow, N. Wakabayashi, and H. G. Smith, “Lattice Dynamics of Pyrolytic Graphite”, *Phys. Rev. B* **5**, 4951 (1972).
- [111] J. L. Wilkes, R. E. Palmer, and R. F. Willis, “Phonons in graphite studied by EELS”, *J. Electron Spectr. Rel. Phen.* **44**, 355 (1987).
- [112] C. Oshima, T. Aizawa, R. Souda, Y. Ishizawa, and Y. Sumiyoshi, “Surface phonon dispersion curves of graphite (0001) over the entire energy region”, *Solid State Comm.* **65**, 1601 (1988).
- [113] S. Siebentritt, R. Poes, and K.-H. Rieder, “Surface phonon dispersion in graphite and in a lanthanum graphite intercalation compound”, *Phys. Rev. B* **55**, 7927 (1997).
- [114] R. A. Jishi and G. Dresselhaus, “Lattice-dynamical model for graphite”, *Phys. Rev. B* **26**, 4514 (1982).

- [115] D. Sánchez-Portal, E. Artacho, J. M. Soler, A. Rubio, and P. Ordejón, “*Ab initio* structural, elastic, and vibrational properties of carbon nanotubes”, *Phys. Rev. B* **59**, 12 678 (1999).
- [116] C. Mapelli, C. Castiglioni, G. Zerbi, and K. Müllen, “Common force field for graphite and polycyclic aromatic hydrocarbons”, *Phys. Rev. B* **60**, 12 710 (1999).
- [117] O. Dubay and G. Kresse, “Accurate density functional calculations for the phonon dispersion relations of graphite layer and carbon nanotubes”, *Phys. Rev. B* **67**, 035 401 (2003).
- [118] A. Grüneis, R. Saito, T. Kimura, L. G. Cançado, M. A. Pimenta, *et al.*, “Determination of two-dimensional phonon dispersion relation of graphite by raman spectroscopy”, *Phys. Rev. B* **65**, 155 405 (2002).
- [119] The graphite flakes were kindly provided by A. V. Tamashauskyy.
- [120] *International Tables for Crystallography: Space-group symmetry*, vol. A (Kluwer Academic Publishers, Dordrecht, 1995), ed. by T. Hahn.
- [121] R. J. Elliott and M. F. Thorpe, “Group theoretical selection rules in inelastic neutron scattering”, *Proc. Phys. Soc.* **91**, 903 (1967).
- [122] J. M. Perez-Mato, M. Aroyo, J. Hlinka, M. Quilichini, and R. Currat, “Phonon Symmetry Selection Rules for Inelastic Neutron Scattering”, *Phys. Rev. Lett.* **81**, 2462 (1998).
- [123] A. K. Kirov, M. I. Aroyo, and J. M. Perez-Mato, “NEUTRON: a program for computing phonon extinction rules of inelastic neutron scattering and thermal diffuse scattering experiments”, *J. Appl. Cryst.* **36**, 1085 (2003).
- [124] J. Maultzsch, S. Reich, C. Thomsen, H. Requardt, and P. Ordejón, “Phonon dispersion of graphite”, *Phys. Rev. Lett.* **92**, 075 501 (2004).
- [125] F. Tuinstra and J. L. Koenig, “Raman spectrum of graphite”, *J. Chem. Phys.* **53**, 1126 (1970).
- [126] P. Pavone, R. Bauer, K. Karch, O. Schütt, S. Vent, *et al.*, “*Ab-initio* phonon calculations in solids”, *Physica B* **220**, 439 (1996).
- [127] R. Saito, A. Jorio, A. G. Souza-Filho, G. Dresselhaus, M. S. Dresselhaus, and M. A. Pimenta, “Probing Phonon Dispersion Relations of Graphite by Double Resonance Raman Scattering”, *Phys. Rev. Lett.* **88**, 027 401 (2002).

- [128] J. P. Perdew, K. Burke, and M. Ernzerhof, “Generalized gradient approximation made simple”, *Phys. Rev. Lett.* **77**, 3865 (1996).
- [129] J. M. Soler, E. Artacho, J. D. Gale, A. García, J. Junquera, P. Ordejón, and D. Sánchez-Portal, “The SIESTA method for ab initio order- N materials simulation”, *J. Phys.: Cond. Mat.* **14**, 2745 (2002).
- [130] F. Favot and A. Dal Corso, “Phonon dispersions: Performance of the generalized gradient approximation”, *Phys. Rev. B* **60**, 11 427 (1999).
- [131] Z. Yao, C. L. Kane, and C. Dekker, “High-field electrical transport in single-wall carbon nanotubes”, *Phys. Rev. Lett.* **84**, 2941 (2000).
- [132] B. Bourlon, D. Glatli, B. Plaçais, J. Berroir, C. Miko, L. Forró, and A. Bachtold, “Geometrical dependence of high-bias current in multiwalled carbon nanotubes”, *Phys. Rev. Lett.* **92**, 026 804 (2004).
- [133] C. Thomsen and S. Reich, “Double-resonant Raman scattering in graphite”, *Phys. Rev. Lett.* **85**, 5214 (2000).
- [134] J. Maultzsch, S. Reich, and C. Thomsen, “Double-resonant Raman scattering in graphite: interference effects, selection rules and phonon dispersion”, (2004), submitted to *Phys. Rev. B*.
- [135] J. Maultzsch, S. Reich, C. Thomsen, E. Dobardžić, I. Milošević, and M. Damnjanović, “Phonon dispersion of carbon nanotubes”, *Solid State Commun.* **121**, 471 (2002).
- [136] E. Dobardžić, I. M. B. Nikolić, T. Vuković, and M. Damnjanović, “Single-wall carbon nanotubes phonon spectra: Symmetry-based calculations”, *Phys. Rev. B* **68**, 045 408 (2003).
- [137] S. Reich, C. Thomsen, and P. Ordejón, “Eigenvectors of chiral nanotubes”, *Phys. Rev. B* **64**, 195 416 (2001).
- [138] J. Kürti, V. Zólyomi, M. Kertesz, and G. Sun, “The geometry and the radial breathing mode of carbon nanotubes: beyond the ideal behaviour”, *New J. Phys.* **5**, 125.1 (2003).
- [139] M. Machón *et al.* (unpublished).
- [140] V. N. Popov and L. Henrard, “Breathing-like modes of multiwalled carbon nanotubes”, *Phys. Rev. B* **65**, 235 415 (2002).

- [141] J. M. Benoit, J. P. Buisson, O. Chauvet, C. Godon, and S. Lefrant, “Low-frequency Raman studies of multiwalled carbon nanotubes: Experiments and theory”, *Phys. Rev. B* **66**, 073 417 (2002).
- [142] S. Bandow, C. Chen, G. U. Sumanasekera, R. Gupta, M. Yudasaka, S. Iijima, and P. C. Eklund, “Diameter-selective resonant Raman scattering in double-wall carbon nanotubes”, *Phys. Rev. B* **66**, 075 416 (2002).
- [143] R. R. Bacsa, A. Peigney, C. Laurent, P. Puech, and W. S. Bacsa, “Chirality of internal metallic and semiconducting carbon nanotubes”, *Phys. Rev. B* **65**, 161 404(R) (2002).
- [144] C. Kramberger, R. Pfeiffer, H. Kuzmany, V. Zólyomi, and J. Kürti, “Assignment of chiral vectors in carbon nanotubes”, *Phys. Rev. B* **68**, 235 404 (2003).
- [145] M. Damnjanović, T. Vuković, and I. Milošević, “Super-slippery carbon nanotubes: Symmetry breaking breaks friction”, *Eur. Phys. J. B* **25**, 131 (2002).
- [146] E. Dobardžić, J. Maultzsch, I. Milošević, C. Thomsen, and M. Damnjanović, “The radial breathing mode frequency in double-walled carbon nanotubes: an analytical approximation”, *phys. stat. sol. (b)* **237**, R7 (2003).
- [147] J. Kürti, G. Kresse, and H. Kuzmany, “First-principles calculations of the radial breathing mode of single-wall carbon nanotubes”, *Phys. Rev. B* **58**, 8869 (1998).
- [148] A. Jorio, R. Saito, J. H. Hafner, C. M. Lieber, M. Hunter, *et al.*, “Structural (n, m) determination of isolated single-wall carbon nanotubes by resonant Raman scattering”, *Phys. Rev. Lett.* **86**, 1118 (2001).
- [149] J. Maultzsch, S. Reich, and C. Thomsen, “Chirality selective Raman scattering of the D-mode in carbon nanotubes”, *Phys. Rev. B* **64**, 121 407(R) (2001).
- [150] S. Reich and C. Thomsen, “Raman spectroscopy of graphite”, *Philosophical Transactions of the Royal Society* (2004), submitted.
- [151] M. A. Pimenta, A. Marucci, S. A. Empedocles, M. G. Bawendi, E. B. Hanlon, *et al.*, “Raman modes of metallic carbon nanotubes”, *Phys. Rev. B* **58**, R16 016 (1998).
- [152] P. M. Rafailov, H. Jantoljak, and C. Thomsen, “Electronic transitions in single-walled carbon nanotubes: A resonance Raman study”, *Phys. Rev. B* **61**, 16 179 (2000).
- [153] C. Jiang, K. Kempa, J. Zhao, U. Schlecht, U. Kolb, *et al.*, “Strong enhancement of the Breit-Wigner-Fano Raman line in carbon nanotube bundles caused by plasmon band formation”, *Phys. Rev. B* **66**, 161 404(R) (2002).

- [154] P. Nikolaev, M. J. Bronikowski, R. K. Bradley, F. Rohmund, D. T. Colbert, K. A. Smith, and R. E. Smalley, "Gas-phase catalytic growth of single-walled carbon nanotubes from carbon monoxide", *Chem. Phys. Lett.* **313**, 91 (1999).
- [155] A. M. Rao, E. Richter, S. Bandow, B. Chase, P. C. Eklund, *et al.*, "Diameter-selective Raman scattering from vibrational modes in carbon nanotubes", *Science* **275**, 187 (1997).
- [156] R. M. Martin and L. M. Falicov, "Resonant Raman scattering", in *Light Scattering in Solids I: Introductory Concepts*, edited by M. Cardona (Springer, Berlin, 1983), vol. 8 of *Topics in Applied Physics*, p. 79.
- [157] F. Cerdeira, E. Anastassakis, W. Kauschke, and M. Cardona, "Stress-induced doubly resonant Raman scattering in GaAs", *Phys. Rev. Lett.* **57**, 3209 (1986).
- [158] F. Agulló-Rueda, E. E. Mendez, and J. M. Hong, "Double resonant Raman scattering induced by an electric field", *Phys. Rev. B* **38**, 12 720(R) (1988).
- [159] C. Trallero-Giner, T. Ruf, and M. Cardona, "Theory of one-phonon resonant Raman scattering in a magnetic field", *Phys. Rev. B* **41**, 3028 (1990).
- [160] F. Calle, J. M. Calleja, F. Meseguer, C. Tejedor, L. Viña, C. López, and K. Ploog, "Double Raman resonances induced by a magnetic field in GaAs-AlAs multiple quantum wells", *Phys. Rev. B* **44**, 1113 (1991).
- [161] D. A. Kleinman, R. C. Miller, and A. C. Gossard, "Double resonant LO-phonon Raman scattering observed with GaAs-Al_xGa_{1-x}As quantum wells", *Phys. Rev. B* **35**, 664 (1987).
- [162] V. Zólyomi and J. Kürti, "Calculating the discrepancy between the Stokes and anti-Stokes Raman D band of carbon nanotubes using double resonance theory", *Phys. Rev. B* **66**, 073 418 (2002).
- [163] R. P. Vidano, D. B. Fischbach, L. J. Willis, and T. M. Loehr, "Observation of Raman band shifting with excitation wavelength for carbons and graphites", *Solid State Commun.* **39**, 341 (1981).
- [164] Y. Wang, D. C. Alsmeyer, and R. L. McCreery, "Raman spectroscopy of carbon materials: Structural basis of observed spectra", *Chem. Mater.* **2**, 557 (1990).
- [165] I. Pócsik, M. Hundhausen, M. Koos, and L. Ley, "Origin of the D peak in the Raman spectrum of microcrystalline graphite", *J. Non-Cryst. Sol.* **227-230B**, 1083 (1998).

- [166] M. J. Matthews, M. A. Pimenta, G. Dresselhaus, M. S. Dresselhaus, and M. Endo, “Origin of dispersive effects of the Raman D band in carbon materials”, *Phys. Rev. B* **59**, R6585 (1999).
- [167] M. A. Pimenta, A. Jorio, S. D. M. Brown, A. G. Souza-Filho, G. Dresselhaus, *et al.*, “Diameter dependence of the Raman D -band in isolated single-wall carbon nanotubes”, *Phys. Rev. B* **64**, 041 401(R) (2001).
- [168] S. D. M. Brown, A. Jorio, M. S. Dresselhaus, and G. Dresselhaus, “Observations of the D -band feature in the Raman spectra of carbon nanotubes”, *Phys. Rev. B* **64**, 073 403 (2001).
- [169] J. Kürti, V. Zólyomi, A. Grüneis, and H. Kuzmany, “Double resonant Raman phenomena enhanced by van Hove singularities in single-wall carbon nanotubes”, *Phys. Rev. B* **65**, 165 433 (2002).
- [170] J. Maultzsch, S. Reich, and C. Thomsen, “Double-resonant Raman scattering in single-wall carbon nanotubes”, in *Proc. 26th ICPS*, edited by A. R. Long and J. H. Davies (Institute of Physics Publishing, Bristol (UK), 2002), p. D209.
- [171] C. Thomsen, “Second-order Raman spectra of single and multi-walled carbon nanotubes”, *Phys. Rev. B* **61**, 4542 (2000).
- [172] A. G. Souza Filho, A. Jorio, G. Dresselhaus, M. S. Dresselhaus, R. Saito, *et al.*, “Effect of quantized electronic states on the dispersive Raman features in individual single-wall carbon nanotubes”, *Phys. Rev. B* **65**, 035 404 (2002).
- [173] J. Maultzsch, S. Reich, U. Schlecht, and C. Thomsen, “High-energy phonon branches of an individual metallic carbon nanotube”, *Phys. Rev. Lett.* **91**, 087 402 (2003).
- [174] L. G. Cançado, M. A. Pimenta, R. Saito, A. Jorio, L. O. Ladeira, *et al.*, “Stokes and anti-Stokes double resonance Raman scattering in two-dimensional graphite”, *Phys. Rev. B* **66**, 035 415 (2002).
- [175] A. K. Sood, R. Gupta, and S. A. Asher, “Origin of the unusual dependence of Raman D band on excitation wavelength in graphite-like materials”, *J. Appl. Phys.* **90**, 4494 (2001).
- [176] C. Castiglioni, F. Negri, M. Rigolio, and G. Zerbi, “Raman activation in disordered graphites of the A_1 symmetry forbidden $k \neq 0$ phonon: The origin of the D line”, *J. Chem. Phys.* **115**, 3769 (2001).

- [177] A. Ferrari and J. Robertson, "Interpretation of raman spectra of disordered and amorphous carbon", *Phys. Rev. B* **61**, 14 095 (2000).
- [178] A. Ferrari and J. Robertson, "Resonant Raman spectroscopy of disordered, amorphous, and diamondlike carbon", *Phys. Rev. B* **64**, 075 414 (2001).
- [179] H. H. Gommans, J. W. Alldredge, H. Tashiro, J. Park, J. Magnuson, and A. G. Rinzler, "Fibers of aligned single-walled carbon nanotubes: Polarized Raman spectroscopy", *J. Appl. Phys.* **88**, 2509 (2000).
- [180] A. Jorio, G. Dresselhaus, M. S. Dresselhaus, M. Souza, M. S. S. Dantas, *et al.*, "Polarized Raman study of single-wall semiconducting carbon nanotubes", *Phys. Rev. Lett.* **85**, 2617 (2000).
- [181] S. Reich, C. Thomsen, G. S. Duesberg, and S. Roth, "Intensities of the Raman active modes in single and multiwall nanotubes", *Phys. Rev. B* **63**, R041 401 (2001).
- [182] P. M. Rafailov, J. Maultzsch, M. Machón, S. Reich, C. Thomsen, *et al.*, "Pressure and polarization-angle dependent raman spectra of aligned single-wall carbon nanotubes in $\text{AlPO}_4\text{-5}$ crystal channels", in *Electronic Properties of Novel Materials-Molecular Nanostructures*, edited by H. Kuzmany, J. Fink, M. Mehring, and S. Roth, AIP 633 (2002), p. 290.
- [183] Z. M. Li, Z. K. Tang, H. J. Liu, N. Wang, C. T. Chan, *et al.*, "Polarized absorption spectra of single-walled 4 Å carbon nanotubes aligned in channels of an $\text{AlPO}_4\text{-5}$ single crystal", *Phys. Rev. Lett.* **87**, 127 401 (2001).
- [184] M. Cardona, "Resonance phenomena", in *Light Scattering in Solids II*, edited by M. Cardona and G. Güntherodt (Springer, Berlin, 1982), vol. 50 of *Topics in Applied Physics*, p. 19.
- [185] W. Kauschke, A. K. Sood, M. Cardona, and K. Ploog, "Resonance Raman scattering in $\text{GaAs-Al}_x\text{Ga}_{1-x}\text{As}$ superlattices: Impurity-induced Fröhlich-interaction scattering", *Phys. Rev. B* **36**, 1612 (1987).
- [186] M. Canonico, G. B. Adams, C. Poweleit, J. Menéndez, J. B. Page, *et al.*, "Characterization of carbon nanotubes using Raman excitation profiles", *Phys. Rev. B* **65**, 201 402(R) (2002).
- [187] M. S. Strano, S. K. Doorn, E. H. Haroz, C. Kittrell, R. H. Hauge, and R. E. Smalley, "Assignment of (n, m) Raman and optical features of metallic single-walled carbon nanotubes", *Nano Lett.* **3**, 1091 (2003).

- [188] A. Jorio, A. G. Souza Filho, G. Dresselhaus, M. S. Dresselhaus, A. K. Swan, *et al.*, “G-band resonant Raman study of 62 isolated single-wall carbon nanotubes”, *Phys. Rev. B* **65**, 155 412 (2002).
- [189] E. Richter and K. R. Subbaswamy, “Theory of size-dependent resonance Raman scattering from carbon nanotubes”, *Phys. Rev. Lett.* **79**, 2738 (1997).
- [190] R. Saito, T. Takeya, T. Kimura, G. Dresselhaus, and M. S. Dresselhaus, “Raman intensity of single-wall carbon nanotubes”, *Phys. Rev. B* **57**, 4145 (1998).
- [191] O. Dubay, G. Kresse, and H. Kuzmany, “Phonon Softening in Metallic Nanotubes by a Peierls-like Mechanism”, *Phys. Rev. Lett.* **88**, 235 506 (2002).
- [192] S. D. M. Brown, P. Corio, A. Marucci, M. S. Dresselhaus, M. A. Pimenta, and K. Kneipp, “Anti-stokes Raman spectra of single-walled carbon nanotubes”, *Phys. Rev. B* **61**, R5137 (2000).
- [193] S.-L. Zhang, X. Hu, H. Li, Z. Shi, K. T. Yue, *et al.*, “Abnormal anti-Stokes Raman scattering of carbon nanotubes”, *Phys. Rev. B* **66**, 035 413 (2002).
- [194] Z. Yu and L. E. Brus, “ (n, m) structural assignments and chirality dependence in single-wall carbon nanotube Raman scattering”, *J. Phys. Chem. B* **105**, 6831 (2001).
- [195] I. Loa, *The spin-Peierls system CuGeO₃: a Raman scattering study*, Dissertation Technische Universität Berlin (Wiss.-u.-Technik-Verl., Berlin, 1998).
- [196] K. Kempa, “Gapless plasmons in carbon nanotubes and their interactions with phonons”, *Phys. Rev. B* **66**, 195 406 (2002).
- [197] R. S. Lee, H. J. Kim, J. E. Fischer, A. Thess, and R. E. Smalley, “Conductivity enhancement in single-walled carbon nanotube bundles doped with K and Br”, *Nature* **388**, 255 (1997).
- [198] X. Liu, C. Lee, C. Zhou, and J. Han, “Carbon nanotube field-effect inverters”, *Appl. Phys. Lett.* **79**, 3329 (2001).
- [199] V. Derycke, R. Martel, J. Appenzeller, and P. Avouris, “Controlling doping and carrier injection in carbon nanotube transistors”, *Appl. Phys. Lett.* **80**, 2773 (2002).
- [200] O. Stephan, P. M. Ajayan, C. Colliex, P. Redlich, J. M. Lambert, P. Bernier, and P. Lefin, “Doping Graphitic and Carbon Nanotube Structures with Boron and Nitrogen”, *Science* **266**, 1683 (1994).

- [201] D. L. Carroll, P. Redlich, X. B. J.-C. Charlier, S. Curran, P. M. Ajayan, S. Roth, and M. Rühle, “Effects of Nanodomain Formation on the Electronic Structure of Doped Carbon Nanotubes”, *Phys. Rev. Lett.* **81**, 2332 (1998).
- [202] B. Wei, R. Spolenak, P. Kohler-Redlich, M. Rühle, and E. Arzt, “Electrical transport in pure and boron-doped carbon nanotubes”, *Appl. Phys. Lett.* **74**, 3149 (1999).
- [203] H. J. Choi, J. Ihm, S. G. Louie, and M. L. Cohen, “Defects, quasibound states, and quantum conductance in metallic carbon nanotubes”, *Phys. Rev. Lett.* **84**, 2917 (2000), and references therein.
- [204] M. Hirscher, M. Becher, M. Haluska, U. Dettlaff-Weglikowska, A. Quintel, *et al.*, “Hydrogen storage in sonicated carbon materials”, *Appl. Phys. A: Mater. Sci. Process.* **72**, 129 (2001).
- [205] L. Zhang, H. Li, K.-T. Yue, S.-L. Zhang, X. Wu, *et al.*, “Effects of intense laser irradiation on Raman intensity features of carbon nanotubes”, *Phys. Rev. B* **65**, 073401 (2002).
- [206] C. Zhi, X. D. Bai, and E. G. Wang, “Raman characterization of boron carbonitride nanotubes”, *Appl. Phys. Lett.* **80**, 3590 (2002).
- [207] R. G. Lacerda, A. S. Teh, M. H. Yang, K. B. K. Teo, N. L. Rupesinghe, *et al.*, “Growth of high-quality single-wall carbon nanotubes without amorphous carbon formation”, *Appl. Phys. Lett.* **84**, 269 (2004).
- [208] V. Skákalová, M. Hulman, P. Fedorko, P. Lukáč, and S. Roth, “Effect of γ -irradiation on single-wall carbon nanotube paper”, in *Electronic Properties of Novel Materials-Molecular Nanostructures*, edited by H. Kuzmany, J. Fink, M. Mehring, and S. Roth, AIP (2003), p. 143.
- [209] J. Maultzsch, S. Reich, C. Thomsen, S. Webster, R. Czerw, *et al.*, “Raman characterization of boron-doped multiwalled carbon nanotubes”, *Appl. Phys. Lett.* **81**, 2647 (2002).
- [210] M. H. Brodsky, “Raman Scattering in Amorphous Semiconductors”, in *Light Scattering in Solids I: Introductory Concepts*, edited by M. Cardona (Springer-Verlag, Berlin Heidelberg New York, 1983), vol. 8 of *Topics in Applied Physics*, p. 205, 2 edn.
- [211] R. S. Berg and P. Y. Yu, “Resonant Raman study of intrinsic defect modes in electron- and neutron-irradiated GaAs”, *Phys. Rev. B* **35**, 2205 (1987).

- [212] I. Milošević, B. Nikolić, and M. Damnjanović, “Symmetry-based calculations of optical absorption in narrow nanotubes”, *Phys. Rev. B* **69**, 113 408 (2004).
- [213] F. S. Khan and P. B. Allen, “Deformation potentials and electron-phonon scattering: Two new theorems”, *Phys. Rev. B* **29**, 3341 (1984).
- [214] M. Machón, S. Reich, J. Maultzsch, P. Ordejón, and C. Thomsen, “The strength of the radial breathing mode in single-walled carbon nanotubes”, (2003), submitted to *Phys. Rev. Lett.*
- [215] A. Cantarero, C. Trallero-Giner, and M. Cardona, “Excitons in one-phonon resonant Raman scattering: Deformation-potential interaction”, *Phys. Rev. B* **39**, 8388 (1989).
- [216] C. Trallero-Giner, A. Cantarero, M. Cardona, and M. Mora, “Impurity-induced resonant Raman scattering”, *Phys. Rev. B* **45**, 6601 (1992).
- [217] M. H. Grimsditch and M. Cardona, “Absolute Cross-Section for Raman Scattering by Phonons in Silicon”, *phys. stat. sol.* **102**, 155 (1980).
- [218] I. Loa, S. Gronemeyer, C. Thomsen, O. Ambacher, D. Schikora, and D. J. As, “Comparative Determination of Absolute Raman Scattering Efficiencies and Applications to GaN”, *J. Raman Spectr.* **29**, 291 (1998).
- [219] H. R. Philipp and E. A. Taft, “Optical Constants of Silicon in the Region 1 to 10 eV”, *Phys. Rev.* **120**, 37 (1960).

Acknowledgments

I would like to thank the people who contributed to this work, especially

my advisor Christian Thomsen for encouraging me to stay in the field of carbon nanotubes, for his continuous support and interest in this work, for many discussions and for the granted freedom in organizing my work. I always enjoyed being in his group and learning about physics. Many thanks also for introducing me to the dye laser and to absolute Raman cross sections. Special thanks to Christian Thomsen and Stephanie Reich for the very nice (and slightly crazy) time during writing the book, it was great fun.

Prof. Dr. Wolfgang Richter for reviewing this thesis.

Prof. Dr. Siegfried Hess for being the chairman of my thesis committee.

Stephanie Reich for teaching me many things, in particular group theory and Raman scattering and the beginnings of SIESTA. Many thanks for the discussions on the D mode, correlation tables, and symmetry, and especially for encouraging me many times.

María Machón for all the discussions on phonons, hexagons, N 's, and electron-phonon-coupling and for the help with SIESTA. Many thanks also for the lessons on Spanish and on tortilla-making.

Sabine Bahrs and Christian Kristukat for the many liters of tea, the biscuits (and some bananas), and the fun; my roommates Uwe Kuhlmann, Peter Rafailov, and Paula Guidici, and all members of the group for their help, the nice atmosphere and the Tischtennisplattenparties. Many thanks to Sabine for the double-resonance applet.

Hagen Telg for his patience in working with me, for the nice time in the lab, the Eieruhr, the stories about climbing, and of course the “La Ola”.

Marianne Heinold, Sabine Morgner, Heiner Perls, and Bernd Schöler for their support and help with bureaucracy, all kinds of pumps, cooling systems, the new “XY-Füße”, and for some nice conversations about chocolate. Many thanks to Sabine Morgner for the Raman characterization of the graphite single crystals.

Milan Damnjanović and Ivanka Milošević and the group in Belgrade for teaching us line groups and for the joint work. I very much enjoyed the time in Belgrade and the nice guest house, and the weeks in Arandjelovac and Vrnjačka Banja.

Ulrich Schlecht (MPI Stuttgart) for the samples of isolated nanotubes.

Herwig Requardt (ESRF Grenoble); without his help we could not have done the inelastic X-ray experiment on graphite.

Pablo Ordejón for the kind hospitality in Barcelona and the opportunity to learn about density functional theory and SIESTA.

Rüdeger for everything and also for proofreading this thesis.

Sonja and my parents.